UNIVERSITY OF BIRMINGHAM

Development and understanding of Pt-based catalysts supported on transition metal carbides for polymer electrolyte fuel cells

By

JAVIER MONZÓ GIMÉNEZ

A thesis submitted to the

University of Birmingham

For the degree of

DOCTOR OF PHILOSOPHY

School of Chemistry

College of Engineering and Physical Sciences

University of Birmingham

January 2018

Abstract

The consumption of energy has increased in the last decades due to the industrial development and to a population growth. Consequently, the emissions of gases responsible for the Greenhouse effect are increasing and thus the Global temperature as well. For this reason, our society is pushing to find alternative energy generators. Polymer electrolyte fuel cells (PEFC) are emerging as a potential candidate to replace common energy generators due to its special features. The wide commercialization of Polymer electrolyte fuel cell technology is limited for some factors as the cost and durability of the device. The cost of PEFC is high because Pt is used as the catalysts. Also, the degradation of the catalyst at operation conditions leading in a failure of the device is another limiting factor. For that reason, the development of alternative materials is the key for a wide commercialization of PEFC.

In order to develop novel catalysts, a novel methodology to understand the degradation mechanism has been developed, combining cyclic voltammetry and X-ray fluorescence (XRF). For the validation of the methodology, unsupported Pt nanoparticles and Pt nanoparticles supported on TaC (Pt/TaC) were used. Pt/TaC showed a mass activity improvement and a considerable stability.

On the basis of these results, a series of transition metal carbides (TMC) with high surface area were synthesised: VC, NbC and TaC. Pt nanoparticles were dispersed on the TMC (Pt/TMC) and the resulting catalysts were physically characterized. Also, the stability and mass activity of the Pt/TMC catalysts was

assessed. Pt/NbC was the most stable catalyst under oxidative conditions and it presented an improvement of the mass activity.

In order to tackle the other problem of the PEFC, Pt-alloys with transition metal have been studied for reducing the cost. PtCo nanoparticles were synthesised and characterized and then they were dispersed on NbC. The resulting catalyst, PtCo/NbC was characterized and its stability was tested. PtCo/NbC was more durable and catalytically active than the commercial Pt/C catalysts.

This thesis is dedicated to my parent, brothers, nieces and you for your unconditional support over the years.

Esta tesis está dedicada a mis padres, hermanos, sobrinas y tú por vuestro apoyo incondicional durante los años.

"*You do not really understand something unless you can explain it to your grandmother.*" - Albert Einstein

Acknowledgments

Firstly, I would like to thank to my supervisor, Dr. Paramaconi Rodriguez, for giving me the opportunity to carry out my PhD. Many years ago, you introduced me in the “electrochemical World”. During the last four years, I have learnt a lot of Science from you with our “friendly” group meetings or during our “beer/coffee” meetings. I desire all the best in your scientific career and with your group which I will always feel part in.

Big thank you to the rest of Para’s group, present and past; all of you have contributed somehow to this thesis. Especially to Adam, “Chiquito”, for all this time that we have expended together in the lab discussing about Science and at the staff house discussing about life: “*Myśleć o niebieskich migdałach”*.

To my colleague since the first day of my PhD, Nacho. All your help has been essential to tackle the end of the road, thank brother from another mother. Thank you and Laura for all these pizza evenings. We know that our ways will cross again in the future.

To the person that took her bag to move to the rainy and cold country called England. The person that never doubt and push me to tackle my dreams, Mari Lluch. Thank you love for sharing all this time in Birmingham and be there for all my concerns. I can feel that I can fly next to you.

To my family that has always supported me from the distance that you made it short. Thank you for always being there.

To all other people that I have met during my PhD because they have participate somehow in this thesis; people from Paco's group that made me feel like a member of their group and my friends in Chemistry. To Dr Jackie Deans for her help with all the characterization techniques, she makes everything easier.

Finally, to my UK family: Maria, Ana, Edvin, Dario, Gaëlle, Alex and "puteros", all this time in Birmingham would never be the same without you, you made me happy.

Table of contents

Abbreviations

AFC	Alkaline fuel cell
Ag/AgCl	Silver/ Silver Chloride
ASP	Accelerated stress protocol
AST	Accelerated Stress Test
BOL	Beginning of life
DFT	Density functional theory
DMFC	Direct methanol fuel cell
DoE	United States department of energy
E	Potential
ECSA	Electrochemical Surface Area
EOL	End of life
GDL	Gas difussion layer
ICE	Internal combustion engines
j	Current density
MCFC	Molten carbonate fuel cell
MEA	Membrane electrode assembly
ORR	Oxygen reduction reaction
PAFC	Phosphoric acid fuel cell
PEFC	Polymer electrolyte fuel cell
Pt	Platinum
PtCo-Nps	Platinum Cobalt Nanoparticles
Pt-Nps	Platinum Nanoparticles
RHE	Reversible Hydrogen Electrode
SMSI	Strong-metal-support-interaction
SOFC	Solid oxide fuel cell

TMC	Transition metals carbides
XRD	X-ray Diffraction
XRF	X-ray fluorescence

CHAPTER 1

Polymer electrolyte fuel cells: introduction and limitations/challenges.

Format: Dissertation.

Overview: In this Chapter we give an introduction to polymer electrolyte fuel cell (PEFC), covering the motivation to study PEFC, their advantages upon other alternative energy devices and their limitations/challenges for a wide commercialization. PEFCs are postulated as a proper candidate for green energy generator due to their features, however have some limitations which need to be overcome to consolidate their technology. The main goals of PEFC technology are the reduction of the costs, the increase of the catalytic activity and the increase of the durability.

In this thesis, the strategy to achieve these goals will be to understand the degradation mechanisms behind the poor durability of the common catalysts developing a novel methodology (Chapter 3). Then, Pt catalysts supported on transition metal carbides (TMC) will be synthesized and tested as durable catalysts (Chapter 4). Finally, Pt-alloys will be prepared on stable TMC and tested as cathode catalyst in order to achieve a durable catalyst for PEFC applications (Chapter 5).

1. Introduction

1.1. Motivation

Population and industrial growth has driven an exponential increase of energy demand/consumption since second half of the twentieth century to the present. The worldwide population has increased in 1 billion people in the last twelve years leading to an increase of energy demand.[1] A high percentage of the energy demand is covered by the traditional energy sources such as oil, natural gas and carbon. Fossil fuels have the drawback of generating CO_2. Between 1970 and 2000 the atmospheric emissions of CO_2 amounted to 0.4 gigatonne per year, increasing to 1.0 gigatonne per year between 2000 to 2010. This trend could lead to a global temperature increase between 3.7 – 4.8 ºC in 2100, well above the 2 ºC value set as alarming.[2]

Consumption and deep exploitation of the traditional energy sources is declining their reserves; the remaining amount of fossil fuel will be consumed by 2019.[3,4] The control and security of rich areas in fossil fuels and exploration activities is essential to guarantee the energy supply leading in an increase of both energy and environmental costs. Nuclear energy is the most established alternative energy source to cover the energy demand. However, the society is pushing to reduce the use of nuclear plants due to the difficult waste management and the risk of radioactive leakage from the plants and the disposal containers.

In order to solve the problematic situation of the global warming, 127 countries have ratified the Paris Agreement signed at the United Nations framework convention on climate change 2016.[5] In this document, it is established that the current atmospheric CO_2 concentration, 430 ppm, has to be kept at 450 ppm by

2050. Global temperature increase has to be held below 2 ºC, so that CO_2 emissions have to be zero or close to zero by 2100. In order to mitigate the CO_2 emissions, alternative energy generators need rapid improvement. Fuel cell technology is postulated as the alternative to CO_2 emission technology, among other alternatives as batteries, solar panel, windmills or hydroelectric technology for stationary and portable applications.[6]

1.2. Fuel cells

A fuel cell is an electrochemical device that converts chemical energy, stored in the molecular bonds, into electricity. Grove cell is the earliest dated electric cell developed by William Grove in 1939.[7] It consisted of an electrode of zinc submerged in sulphuric acid and a platinum electrode submerged in nitric acid separated by a porous ceramic pot, producing electricity.

Figure 1 shows a schematic structure of a PEFC. The overall performance and principles of current fuel cells are similar; at the anode takes place the oxidation of the fuel (hydrogen or hydrocarbons) generating cations and electrons. Cations produced go through the membrane and electrons flow by an external circuit to the cathode closing the circuit. At the cathode, cations and electrons combine with an oxidizing agent, commonly O_2, producing water.[3]

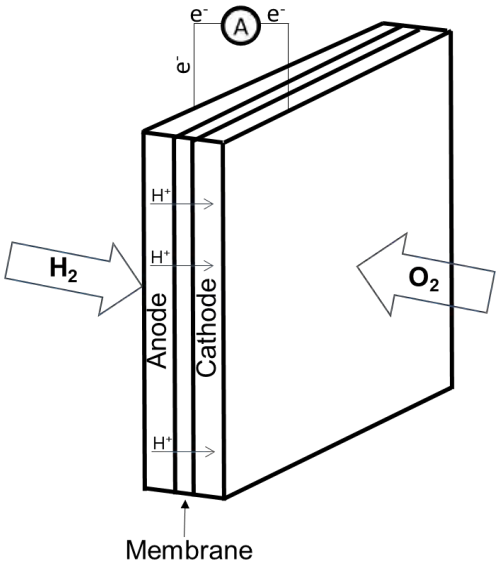

Figure 1 Simplified structure of a polymer electrolyte fuel cell.

Fuel cells present many advantages among traditional technologies as engines or batteries, postulating it as propitious technology. The following characteristics of the fuel cell reflect the advantages:[6]

- Fuel cells produce **low or zero emissions of pollutants** during their performance, and the only by-product generated is water.
- Fuel cell **efficiency** is higher than the one for combustion engines which are limited by the Carnot cycle.
- Fuel cells are **adaptable devices** to the required power, could go from the range of 1 W (mobile phone) to megawatts (stationary plants).
- Fuel cells can **operate continuously** while they are supplied with fuel. In contrast, battery performance must be interrupted for recharging.
- Operation and easy refuelling of the fuel cells produce awfully **low acoustic contamination**.

2. Types of fuel cell

In the last decades, there have been developed six types of fuel cell.[8] The classification is done on the basis of the electrolyte employed inside of the device. The rest of the components as well as the working temperature are established on the basis of the electrolyte. Table 1 summarizes the different types of fuel cell:

Table 1 Types of fuel cell and their main characteristics. Fuel cells using noble catalyst in their electrodes are highlight in blue, the ones highlighted in green use non-noble metals.

	Electrolyte	**Temperature**	**Fuel**
Polymer electrolyte fuel cell (PEFC)	Polymer	40 – 90	H_2
Alkaline fuel cell (AFC)	KOH	40 – 200	H_2
Direct methanol fuel cell (DMFC)	Polymer	60 – 130	Methanol
Phosphoric acid fuel cell (PAFC)	Phosphoric acid	200	H_2
Molten carbonate fuel cell (MCFC)	Molten carbonate	650	H_2, CH_4, CO
Solid oxide fuel cell (SOFC)	Solid oxide	600 - 900	H_2, CH_4, CO

2.1. Polymer electrolyte fuel cell

PEFCs present specific features as low working temperature as well as size versatility to fulfil the power demand. For this reason, PEFCs are postulated as a proper candidate for dynamic and stationary power generation industries among other types of fuel cells.[6]

2.1.1. Structure

Figure 2 shows the structure of a PEFC, the electrochemical energy production takes place at the membrane electrode assembly (MEA) that is composed by the gas diffusion layers (GDL), anode/cathode and membrane.

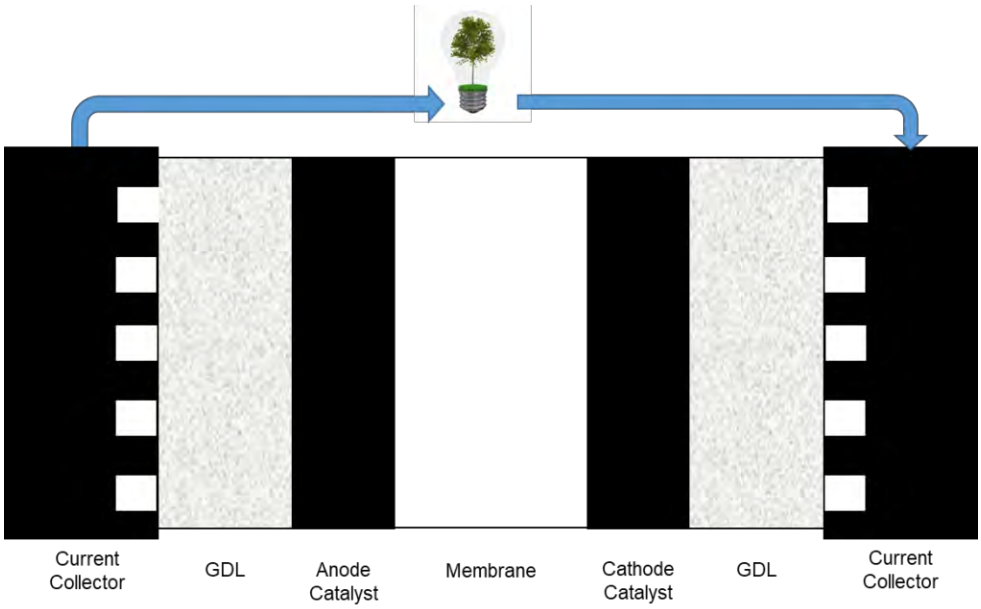

Figure 2 Schematic structure of a PEFC highlighting the main components.

At the anode takes place the hydrogen oxidation (eq. 1):

$$2H_2 \rightarrow 4H^+ + 4e^- \qquad E° = 0.00 \text{ V (RHE)} \qquad (1)$$

The protons generated go through the membrane and the electrons by an external circuit to the cathode. The membrane is not conductive. The oxygen reacts with the protons and electrons (eq. 2) forming water at the cathode.

$$O_2 + 4e^- + 4H^+ \rightarrow 2H_2O \qquad E° = 1.23 \text{ V (RHE)} \qquad (2)$$

The overall reaction for a PEFC is:

$$2H_2 + O_2 \rightarrow 2H_2O \qquad E° = 1.23 \text{ V (RHE)} \qquad (3)$$

As a consequence of the water generated, the flow of the gases to the catalyst surface can be impeded leading in a failure of the device. For this reason, the catalysts have to meet some properties as a surface area of 50 $m^2\ g^{-1}$ for water management, a conductivity higher of 0.1 $S \cdot cm^{-1}$ and a porous structure of 25 nm.

2.1.2. Limitations of PEFC technology

The wide implementation of PEFC in a strategic sector as the automotive sector still being an important challenge despite of its commercialization in aerospace sector. PEFC market is directly related to the hydrogen economy, thus limiting factors of PEFC mass-market have to be solved for increasing demand of PEFC and coercing investments for hydrogen production and distribution.

2.1.2.1. Cost

The cost of PEFCs must be similar to traditional internal combustion engines (ICE) to be commercially viable. Generation of one kW using an ICE is $ 25-35 but the cost with a PEFCs is $ 55.[9] Figure 3 summarizes the cost and targets stablished by the department of energy of the United States (DOE):

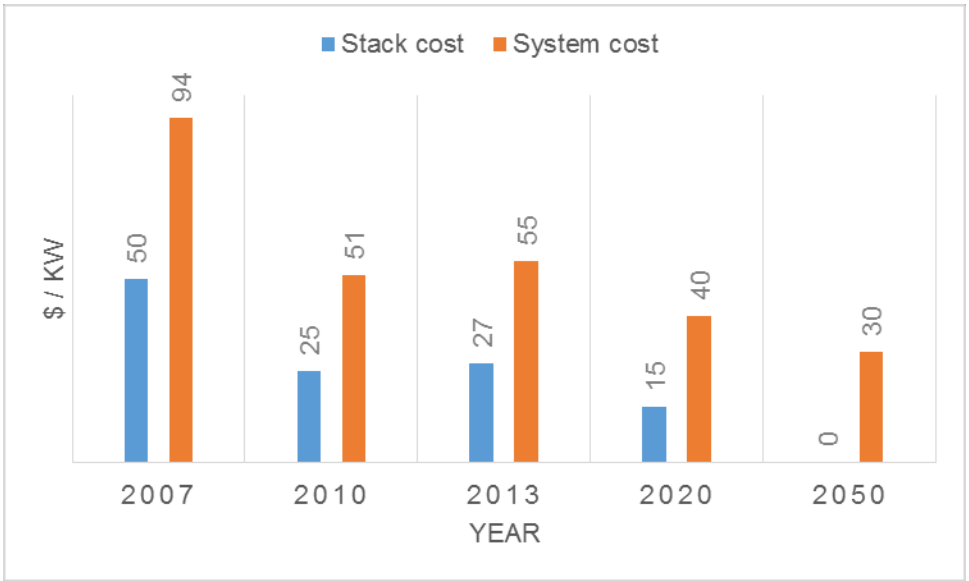

Figure 3 Evolution costs of PEFCs and targets for viable implementation of PEFCs for automotive sector. These values were taken and reproduced with the permission of reference 9.

As can be seen in the Figure 5, the cost of a PEFC is 40 – 50 % more expensive than a common ICE. In order to tackle the DOE's targets, the PEFC cost of has to be reduced by 27 % by 2020 and by 45 % by 2050. Commonly, the scale-up of devices production results in an important decrease in the total cost. Figure 5 shows the detailed costs for PEFC.[10] Components cost is volume-sensitive, therefore their cost is reduced increasing the manufacturing. However, the cost related to the catalyst cannot be reduced. Platinum is the common catalyst employed in PEFC at both sizes of the cell (anode and cathode) being 16 % of the total cost assuming 1000 units. Although by increasing production up to

500000 units the cost of the rest of components might be reduced, the cost of Pt might not be reduced because its price is dominated by demand/supply market. Even though the costs of components could be reduced by increasing production, the economic viability of PEFC lies in the reduction and optimization of the catalyst.

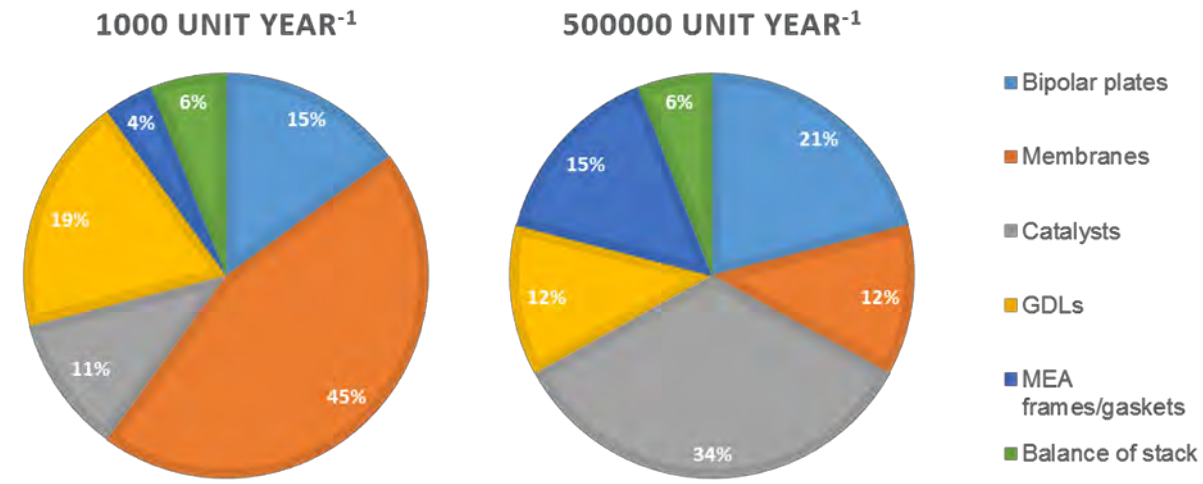

Figure 5 Projected cost of PEFC stack on the basis of production of 1000 and 500000 devices per year.

The use of platinum in PEFC should not be a limitation for a wide commercialization of PEFC because ICE technology employees platinum materials in their converters. However, the amount of Pt employed in a current fuel cell is around 5 times that of an ICE. Since 2005, the loading of Pt has reduced by 80 % making PEFCs more economically viable. This trend is expected to continue in a slower rate.

In addition, the reduction of amount of platinum, other limitations of PEFC technology need to be improved such as degradation of the membrane, sluggish kinetics of oxygen reduction reaction (ORR) or degradation of catalyst layer at the cathode.

2.1.2.2. Poor kinetics of the oxygen reduction reaction

In addition to the high cost associated with the loading of precious metals, PEFCs display poor kinetics for oxygen reduction reaction (ORR) .[13] Even though the exact reaction pathway of the ORR is not fully known, there are two proposed options: associative and dissociative (figure 6). One of those pathways occurs through the direct reduction of adsorbed oxygen to water (k_1). The other pathway consists in the formation of peroxo intermediate species (k_2) and then the reduction of these species to water (k_3).[11]

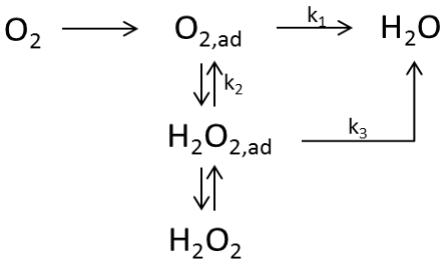

Figure 6 Proposed oxygen reduction reaction mechanism on Pt in acidic medium.

The ORR takes place at 0.8 - 0.85 V vs RHE in a PEFC, a value too far from the reversible electrode potential, 1.23 V vs RHE. This overpotential of 300 mV is due to the slow ORR kinetics and competing reactions such as the formation of platinum oxides.[12] This overpotential must be overcome for the development and commercialization of PEFCs.

Norskov *et al*. reported that the origin of this overpotential is related to the strong adsorption of O_2, which avoid the electron and proton transfer steps of the reaction.[12] Using the density functional theory (DFT), the authors calculated the stability of ORR intermediates. Figure 7A shows the catalytic activity for several

metals as a function of both O and OH binding energy. As can be seen, platinum presents the highest activity for the ORR.

Stamenkovic *et al.* studied the activity for platinum alloys as a function of the d-band center relative to the Fermi level.[13] Figure 7B shows theoretical activity and experimental activity of several platinum alloys as a function of the d-band center. While the DFT calculations predict the highest catalytic activity on the Pt_3Ni, the Pt_3Co alloys have shown the highest experimental catalytic activity. This difference was later associated with the surface structure and coordination.[14]

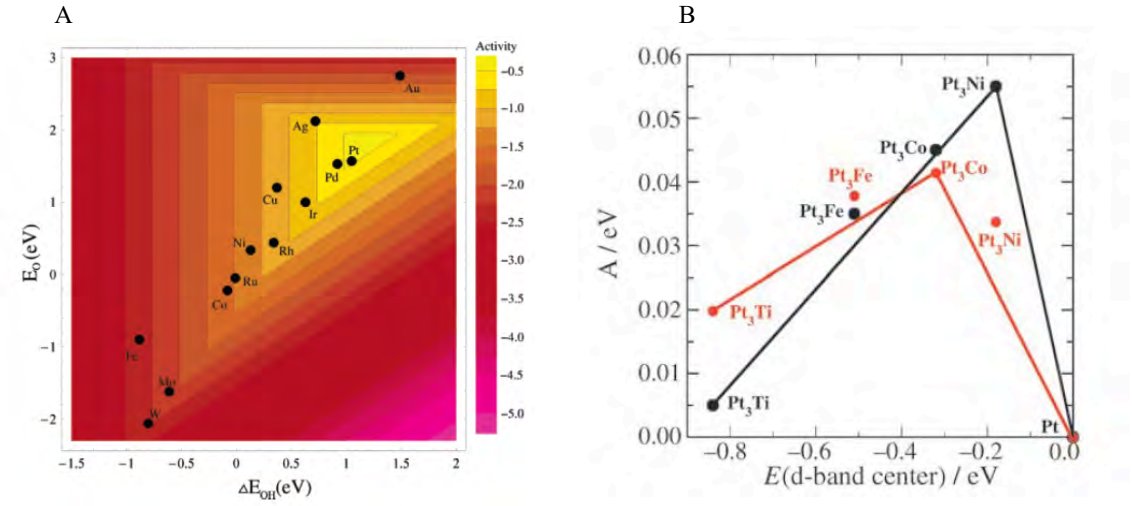

Figure 7 (A)Theoretical values of catalytic activity towards ORR as a function of the O binding energy and OH binding energy for different metals. (B) Activity of Pt-alloys toward ORR theoretical values (black) and experimental values (red) as a function of d-band centre. Figure reproduced and modified with permission from reference 13 y 14.

The surface orientation effect of Pt towards ORR in $HClO_4$ was studied by Markovic *et al.* using Pt low-index single crystals.[15] They found that the reaction takes place through $4e^-$ pathway. In addition, the authors concluded the catalytic activity follows the following trend: (100) > (111) > (110). On the other hand,

Sanchez-Sanchez *et al.* showed improvement of catalytic activity for platinum nanoparticles with (111) preferential orientation.[16]

Platinum alloy nanoparticles have been also studied towards the ORR. Toda *et al.* studied the activity of PtNi, PtCo and PtFe nanoparticles. These particles presented a significant increase in catalytic activity against pure Pt of 10, 15 and 20 times larger respectively.[17–19] Yang *et al.* reported that the catalytic activity of PtNi nanoparticles presents a specific activity increase of ≈ 1.5-3.0 [20]. Huang *et al.* showed the activity of PtCo nanoparticles with an enhancement of ≈1.2-2.2 with respect to pure Pt as well. PtNi nanoparticles (25 % Ni) are considered the state-of-the-art catalysts for ORR. [21] Discrepancies in the literature are associated with different factors as: preparation methods, cleanness of the catalyst, dispersion of the nanoparticles and loading among others.

Pt-alloys present an enhancement of catalytic activity because the increase in the number of 5d vacancies leads in a higher 2p electrodonation from O_2 to Pt. Consequently, the O-O bond is weakened and the oxygen reduction is favoured.[21] Some reports have shown that the amount of second metal added should be controlled since an excessive increase of the second metal results in an increase of the 5d vacancies and in a stronger bond between Pt-O. Consequently, ORR rate is lowered since the electro-donation is more difficult.[17–21]

Particle size is another property which affects the catalytic activity of nanoparticles towards ORR. Hayden *et al.* studied the effect of the particle size on the catalytic activity. Figure 8 shows the activity normalized by the area (specific activity) and by the mass (mass activity). They observed for Pt

nanoparticles dispersed in high porous carbon that the activity presented a maximum for a particle size of 4 nm (figure 8). Particles with higher or lower particle size presented higher interaction with OH yielding a decrease in activity.[22,23]

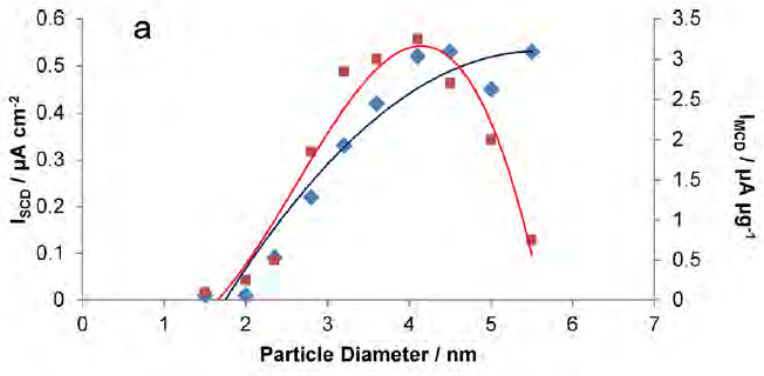

Figure 8 Specific activity (SCD), red square, and mass activity (MCD), blue triangle, of platinum nanoparticles deposited on high porous carbon as a function of the particle size. Figure reproduced with permission from reference 22.

2.1.2.3. Durability

Poor durability of a PEFC compares with a traditional combustion engine is limiting the mass-market of this technology. The durability issue is related to the degradation of some components of the fuel cell as the membrane or the catalysts.[24] Degradation of the cathode catalyst layer affects directly in decay of the fuel cell performance having adverse effects on the cost-efficiency. United States Department of Energy (DoE) establishes that a stationary fuel cell must have 40,000 hours operating lifetime and an automotive fuel cell must have 5,000 hours of operating lifetime to be competitive. However, the operating hours of a fuel cell are far from the targets established, for automotive system is around 1700 hours and 10.000 hours for stationary systems.[25]

The improvement of the durability is essential for making PEFCs technology competitive and leading in a wide commercialization of the technology. Understanding the complex degradation processes within the cathode catalyst layer is the key for the design of more durable catalysts. The degradation of the catalyst layer is consequence of both metal active catalyst and support degradation.

a. Active metal degradation

The main effect of the active metal degradation is the decay of the active surface area leading to a failure of the device.[26] Additionally, processes such as detachment and dissolution have other effects as the contamination of the membrane and consequently its degradation. The degradation mechanisms have been grouped in two main groups: associative and dissociative mechanisms.

The associative mechanisms are agglomeration process[27] in which particles come together forming a cluster and Ostwald ripening[24] in which small particle dissolve and redeposit in larger particles (Figure 9).

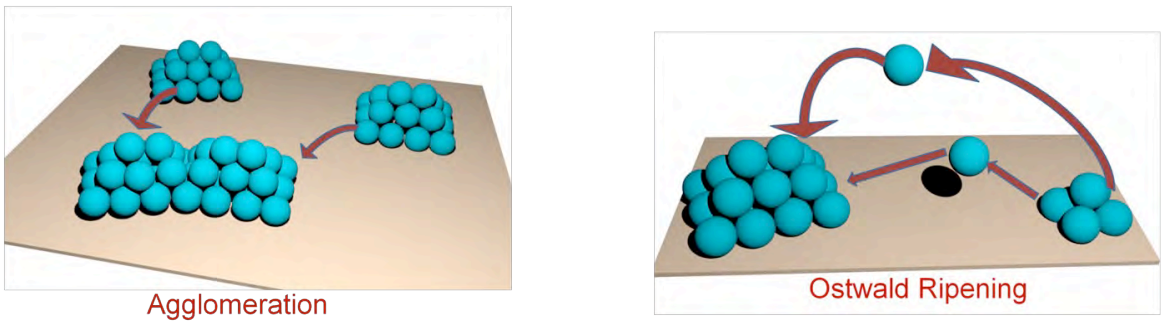

Figure 9 Representation of associative degradation mechanisms within a catalyst layer under PEFC´s operation conditions.

On the other hand, a weak interaction between the support and the metal nanoparticles leads to their detachment.[28] (Figure 10) This weak interaction might be consequence of the degradation of the support (see section b). Additionally, dissolution of the nanoparticles is the other degradation mechanism included in the dissociative processes.[29] Commonly, platinum based nanoparticles are the catalyst employed in the cathode catalyst layer. As a consequence of the PEFCs' operation conditions, platinum dissolves redepositing on the membrane or being expelled in the water stream.

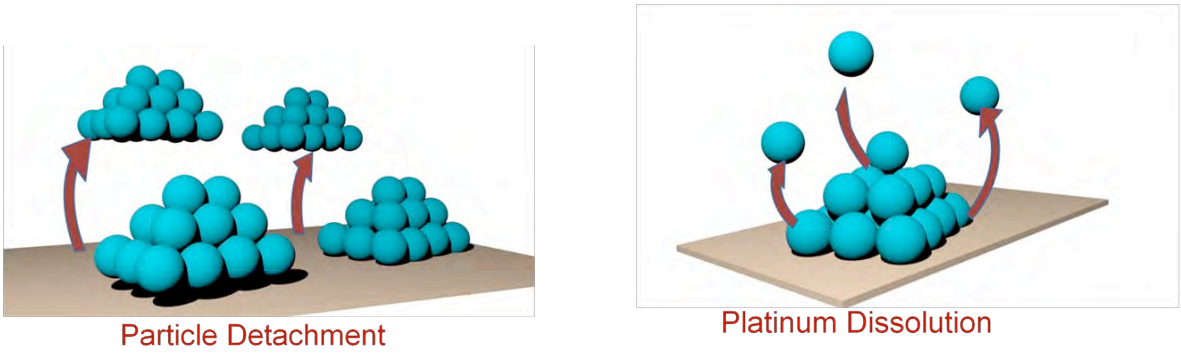

Figure 10. Simplified representation of dissociative mechanisms under PEFC's conditions.

b. Support material degradation

Porous carbon with a high surface area is the common material employed as a support material in low temperature fuel cells. Carbon has ideal characteristics as higher conductivity, well-established pore structure, large surface area and low cost making it as a proper support material. However, the carbon durability under operation conditions has to be improved in order to decrease the ratio cost/durability of PEFC.

The process of turning on/off the fuel cell has to be improved in order to keep potential of the cell under control. The potential in the cathode can reach values

of 1.4 V vs. RHE during the start-stop process of a fuel cell, due to that carbon oxides to carbon dioxide:

$$C + H_2O \rightarrow CO_2 + H^+ + 4\ e^- \qquad E^o = 0.207\ V \text{ vs. RHE} \tag{4}$$

Air is commonly used to remove fuels from the anode and the cathode when a fuel cell is off. In this stage, the potential of the cathode (V^c) and the potential of the anode (V^a) are closed to the equilibrium potential of oxygen (V_{eqO2} = 1.23 V) respect to the electrolyte potential (Φ), thus the cell potential is 0 V (eq. 5).

$$V_{cell} = V^c - V^a = 0\ V \tag{5}$$

Immediately after turning on the fuel cell, the gas channels of the anode closer to the fuel entrance are filled with hydrogen which is oxidized and the V^a is brought to the hydrogen equilibrium potential V^{eq}_{H2} = 0 V (Figure 11). Therefore, the cell potential is around 0.85 V. As V^a is constant through the anode layer due to high conductivity, in the region B the Φ is decreased by available oxygen for keeping the potential close to V^{eq}_{O2}. Due to this low Φ at the region B, (V^c – Φ) is much larger than V^{eq}_{O2}. Consequently, oxygen evolution takes place and carbon gets oxidized. Protons generated during the carbon oxidation go through the membrane to the anode where react with O_2 producing H_2O, closing the reverse current mechanism.

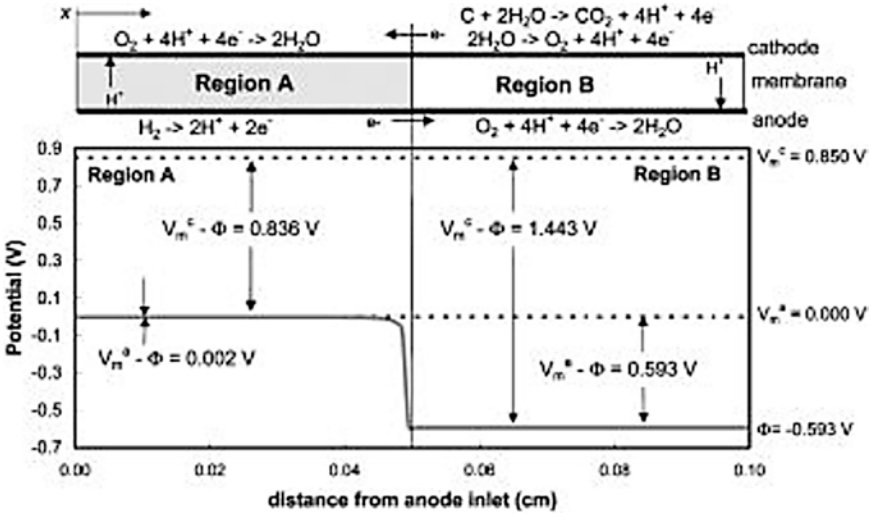

Figure 11 Anode potential representation as a function of the distance from the fuel entrance of the anode.

Dam *et al.* monitored the formation of CO_2 in a Pt/C film at potentials around 1.0 V vs RHE using online electrochemical mass spectroscopy[30] (Figure 12A-B). As a consequence of the oxidation of the carbon, platinum nanoparticles are detached leading to a decay of the ECSA as a function of the degradation time. Additionally, the well-connected porous structure (Figure 12C) of the carbon collapses and some pores are collapsed (Figure 12D). Therefore, platinum nanoparticles are isolated and are not accessible anymore[31]. Hence, the Pt active sites for ORR decrease carrying in a failure of the fuel cell.

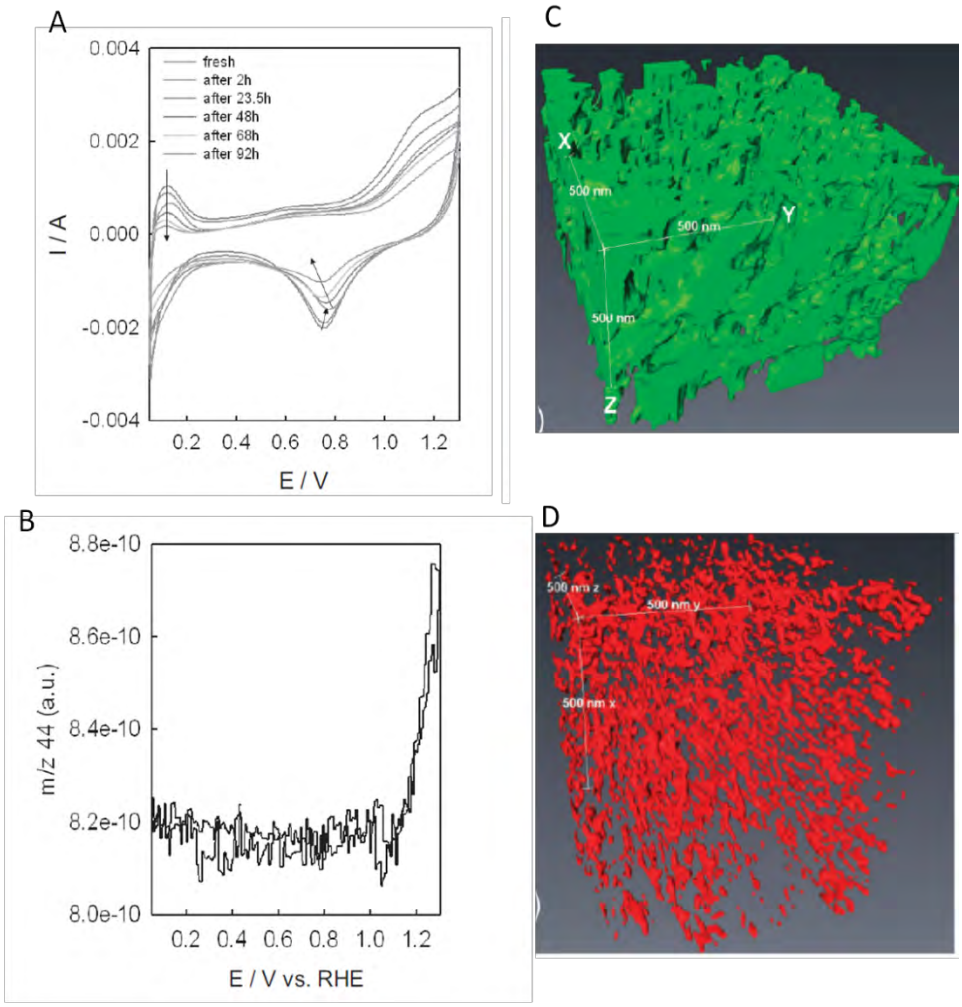

Figure 12 (A) Cyclic voltammograms of Pt/C as a function of time in which potential is kept at 1.05 V and **(B)** CO_2 detection by OLEMS. **(C- D)** Pore structure of carbon before (green) and after (red) degradation protocol. Figures reproduce and modified with permission from the reference 30 and 31.

2.2. Transition metal carbides: properties, synthesis and electrochemical applications

Transition metal carbides (TMCs) have attracted an outstanding attention due to their properties.[32] Since seminal works[32–34], they have been found to possess high conductivity, high mechanical resistance and great chemically stability,

although more detailed features are dependent on transition metal the carbide material is based on. Figure 1 shows the metals and stoichiometry of their most stable carbide, metal carbides of Groups 4-6 present corrosion resistance at room temperature degrading by concentrated acid or by oxidizing agents.[35,36]

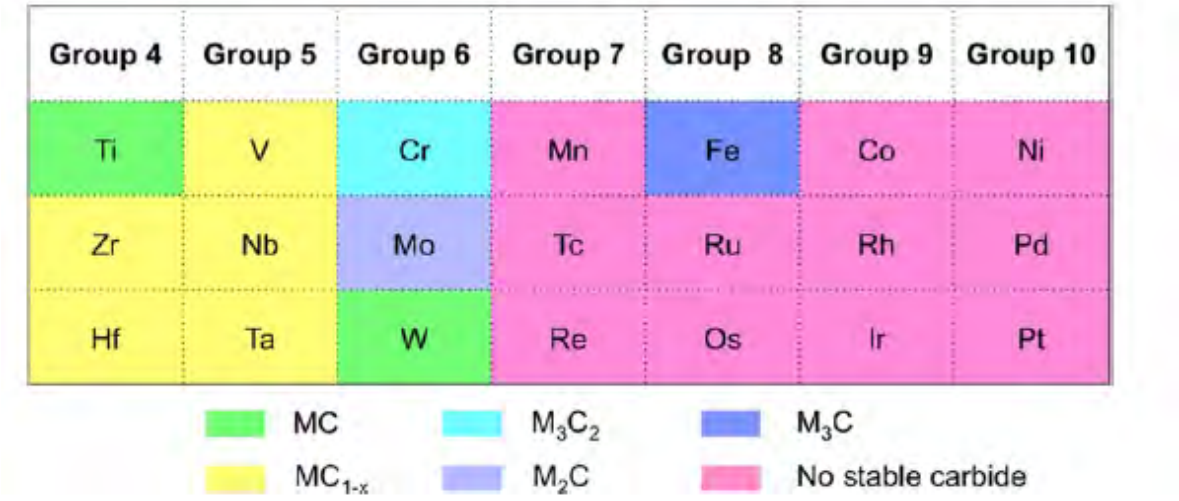

Figure 13 Location at the Periodic Table of transition metal and their more stable carbides and their stoichiometry. Figure reprinted with the permission of reference 35.

To mention some of the most important advances achieved using TMCs, they are used in the manufacture of precise cutting surgical material, military weapons, jewellery, superconductors and construction materials. Due to their mechanical resistance, physical and chemical resistivity TMCs in are used in a lot of applications that are increasing every day.

This scope of applications provoked the search for more efficient synthetic routes towards TMCs synthesis. They have been commonly synthesized using physical approaches as physical vapour deposition, plasma and laser methods.[37–39] Also, chemical methods have been used as liquid precursor route and carbonization of transition metal oxide in presence of carbon.[40,41] Both physical and chemical methods present problems such as the lack of a variety of materials that can be

synthesized (physical methods), the lack of control of particle size (physical and chemical methods)and expensive experimental setups and synthetic routes (physical and chemical methods). Certain developments have been focused on the synthesis of TMC with nanosize, presenting high surface areas or porous structure. These challenges have been tackled using the so-called urea route method which is a versatile method to prepare a wide range of TMC.[42–44] This synthetic method has the advantages that a wide range of TMC can be synthesized, the particle size can be control and the porous structure can be fashioned.[45,46] Even all these advantages, synthesis of TMC show up some challenges as the reduction of synthesis temperature and the purity of the product which commonly present carbon from the synthetic route.[47]

Development of more feasible synthetic methods towards TMCs synthesis is even more important due to recent reports claiming their tremendous performance in the field of electrocatalysis.[48,49] This work underpins the development of Fuel Cells, therefore, it is of utmost importance. TMCs have been used in two different ways. Firstly, a number of reports has been delivered to claim the catalytic activity of relevant reaction. In 1973, Bourdat *et al.* reported the platinum-like behaviour of WC for the oxidation of hydrogen to form water and the isomerization of 2,2-dimethylpropane to 2-methylbutane.[50] Also, transition metal carbides present catalytic activity for hydroprocessing. In addition, CO_2 reduction reaction, which is an extensively studied electrochemical reaction due to environmental problems related to CO_2, could take place over molybdenum carbide producing valuable organic chemicals.[53] Besides, transition metal carbides have been investigated as catalysts for energy generation, Bjerrum *et al.* reported the catalytic activity of WC towards hydrogen evolution reaction.[48]

Nevertheless, these materials do not provide the electrocatalytic efficiency that is enough to drive the Fuel Cell at a commercially relevant level. However, certain properties of TMCs are useful when it comes to supporting the current state-of-the-art catalysts. Commonly used carbon materials do not provide enough stability for the long-term performance. This issue was partially solved by applying TMCs as a support. Both theory and experimental studies have probed that TMCs are promising candidates for catalyst supports.[51,52] Chen et al. studied the stability trend of TMCs by mapping the pH region in which TMCs are stable by chronopotentiometric-titration.[54] Also, TMCs stability was correlated to the oxygen binding energy by DFT calculations confirming that TMCs are potential support materials for fuel cell applications. This combination of TMCs and Pt-based catalyst was also beneficial due to certain electronic effects that increase the catalyst efficiency.

Chhina et al. studied the activity of Pt supported on WC towards the ORR.[55] The activity of Pt/WC was studied after accelerated oxidation test presenting higher current density than Pt/C tested with the same procedure. These results suggest that the combination of Pt with carbides yields higher catalytic activity and durability, possibly due to an electronic effect. Also, tungsten carbide spheres promote higher activity of deposited Pt for the electrooxidation of methanol.[56] Tungsten is the most investigated carbide due to their properties as synergic effects over noble metals deposited. Other transition metal carbides as molybdenum carbide have shown effects on Pt and Pd which present higher activity deposited on Mo_2C for hydrogen oxidation. Pt-group metals supported on VC and TaC have been shown an enhancement of their catalytic activity towards the oxygen reduction reaction.[57-58] Also, Pt-group metals supported on ZrC have

been shown to be more activity for HOR.[59] Alonso-Vante et al. explained that enhancement of the catalytic activity is related with an electronic transfer from the support to the active metal, this phenomenon is called strong-metal-support-interaction (SMSI).[60]

In addition, SMSI between TMCs and electrocatalysts improves the stability of the catalyst formed by the TMC and noble metal. This fact is explained by the following two effects: (1) stability of TMC and noble metals in electrochemical conditions and (2) interactions of TMC and supported metals. However, the synthesis of TMC particles with high surface area still being a challenge for using TMC as support materials within energy generators such as fuel cells.

References

1 J. Melorose, R. Perroy and S. Careas, *World population prospects*, 2015, vol. 1.

2 T. Wilberforce, A. Alaswad, A. Palumbo, M. Dassisti and A. G. Olabi, *Int. J. Hydrogen Energy*, 2015, **41**, 16509–16522.

3 L. Carrette, K. Friedrich and U. Stimming, *Fuel cells*, 2001, **1**, 5–39.

4 L. Carrette and K. A. Friedrich, *ChemPhysChem*, 2000, **1**, 162–193.

5 United Nations, No Title, http://unfccc.int/paris_agreement/items/9485.php.

6 C. Song, *Catal. Today*, 2002, **77**, 17–49.

7 W. R. Grove, *Philos. Mag.*, 1839, **14**, 127–130.

8 S. Mekhilef, R. Saidur and a. Safari, *Renew. Sustain. Energy Rev.*, 2012, **16**, 981–989.

9 S. G. Chalk and J. F. Miller, *J. Power Sources*, 2006, **159**, 73–80.

10 C. Houchins, G. J. Kleen, J. S. Spendelow, J. Kopasz, D. Peterson, N. L. Garland, D. L. Ho, J. Marcinkoski, K. E. Martin, R. Tyler and D. C. Papageorgopoulos, *Membranes (Basel).*, 2012, **2**, 855–878.

11 E. E. Division and L. Alamos, *J. Electrochem. Soc.*

12 J. K. Nørskov, J. Rossmeisl, A. Logadottir, L. Lindqvist, J. R. Kitchin, T. Bligaard and H. Jónsson, *J. Phys. Chem. B*, 2004, **108**, 17886–17892.

13 V. Stamenkovic, B. S. Mun, K. J. J. Mayrhofer, P. N. Ross, N. M. Markovic, J. Rossmeisl, J. Greeley and J. K. Nørskov, *Angew. Chem. Int. Ed. Engl.*, 2006, **45**, 2897–901.

14 V. R. Stamenkovic, B. Fowler, B. S. Mun, G. Wang, P. N. Ross, C. A. Lucas and N. M. Marković, *Science*, 2007, **315**, 493–7.

15 N. M. Markovic, H. A. Gasteiger and P. N. Ross, 1995, **99**, 3411–3415.

16 C. M. Sa, F. J. Vidal-iglesias, A. Aldaz, V. Montiel and E. Herrero, *J. Am. Chem. Soc.*, 2010, **132**, 5622–5624.

17 T. Toda, H. Igarashi, H. Uchida and M. Watanabe, *J. Electrochem. Soc.*, 1999, **146**, 3750–3756.

18 T. Toda, H. Igarashi and M. Watanabe, *J. Electroanal. Chem.*, 1999, **460**, 258–262.

19 T. Toda, H. Igarashi and M. Watanabe, *J. Electrochem. Soc.*, 1998, **145**, 4185–4188.

20 H. Yang, W. Vogel and C. Lamy, *J. Phys. Chem. B*, 2004, **108**, 11024–11034.

21 Q. Huang, H. Yang, Y. Tang, T. Lu and D. L. Akins, *Electrochem. commun.*, 2006, **8**, 1220–1224.

22 B. E. Hayden, *Acc. Chem. Res.*, 2013, **46**, 1858–1866.

23 A. Anastasopoulos, J. C. Davies, L. Hannah, B. E. Hayden, C. E. Lee, C. Milhano, C. Mormiche and L. Offin, *ChemSusChem*, 2013, **6**, 1973–1982.

24 R. Borup, J. Meyers, B. Pivovar, Y. S. Kim, R. Mukundan, N. Garland, D. Myers, M. Wilson, F. Garzon, D. Wood, P. Zelenay, K. More, K. Stroh, T. Zawodzinski, J. Boncella, J. E. McGrath, M. Inaba, K. Miyatake, M. Hori, K. Ota, Z. Ogumi, S. Miyata, A. Nishikata, Z. Siroma, Y. Uchimoto, K. Yasuda, K.-I. Kimijima and N. Iwashita, *Chem. Rev.*, 2007, **107**, 3904–51.

25 F. Preli, *Fuel Cells*, 2002, **2**, 5–9.

26 S. D. Knights, K. M. Colbow, J. St-Pierre and D. P. Wilkinson, *J. Power Sources*, 2004, **127**, 127–134.

27 C. F. Nørgaard, S. N. Stamatin and E. M. Skou, *Int. J. Hydrogen Energy*, 2014, **39**, 17322–17326.

28 F. Hasché, M. Oezaslan and P. Strasser, *J. Electrochem. Soc.*, 2012, **159**, B24–B33.

29 J. C. Meier, C. Galeano, I. Katsounaros, J. Witte, H. J. Bongard, A. A. Topalov, C. Baldizzone, S. Mezzavilla, F. Schüth and K. J. J. Mayrhofer, *Beilstein J. Nanotechnol.*, 2014, **5**, 44–67.

30 V. A. T. Dam, K. Jayasayee and F. A. de Bruijn, *Fuel Cells*, 2009, **9**, 453–462.

31 H. Schulenburg, B. Schwanitz, N. Linse, G. Scherer, A. Wokaun and F. Polytechnique, *J. Phys. Chem. C*, 2011, **115**, 14236–14243.

32 L. Johansson, *Surf. Sci. Rep.*, 1995, **21**, 177–250.

33 B. C. Schulz, University of Alabama, 2011.

34 A. Fukunaga, S. Chu and M. E. Mchenry, *J. Mater. Res.*, 1998, **13**, 2465–2471.

35 D. Ham and J. Lee, *Energies* , 2009, 2.

36 L. Silvestroni and D. Sciti, *Adv. Mater. Sci. Eng.*, 2010, **2010**, 11.

37 E. C. P. Schaaf, M. Kahle, *Appl. Surf. Sci.*

38 B. B. O. Knotek, F. Loffler, A. Schrey, *SurfaceCoated Technol.*, 1993, **61**, 133–138.

39 R. A. Andrievski, *Mater. Sci.*, 1997, **32**, 4463–4484.

40 H. Xiang, Y. Xu, L. Zhang and L. Cheng, *Scr. Mater.*, 2006, **55**, 339–342.

41 A. M. Nartowski, I. P. Parkin, A. J. Craven and W. C. H. Oaj, *J. Mater. Chem.*, 2001, **11**, 3116–3119.

42 C. Giordano and M. Antonietti, *Nano Today*, 2011, **6**, 366–380.

43 Q. Gao, C. Giordano and M. Antonietti, *Small*, 2011, **7**, 3334–40.

44 C. Giordano, C. Erpen, W. Yao and M. Antonietti, *Nano Lett.*, 2008, **8**, 4659–63.

45 J. Zhu, K. Sakaushi, G. Clavel, M. Shalom, M. Antonietti and T.-P. Fellinger, *J. Am. Chem. Soc.*, 2015, **137**, 5480–5485.

46 M. Antonietti, N. Fechler and T.-P. Fellinger, *Chem. Mater.*, 2014, **26**, 196–210.

47 P. Justin, P. H. K. Charan and G. R. Rao, *Appl. Catal. B Environ.*, 2014, **144**, 767–774.

48 A. L. Tomas-garcia, Q. Li, J. O. Jensen and N. J. Bjerrum, 2014, **9**, 1016–1032.

49 F. Meunier, P. Delporte, B. Heinrich, C. Bouchy, C. Crouzet, C. Pham-Huu, P. Panissod, J. J. Lerou, P. L. Mills and M. J. Ledoux, *J. Catal.*, 1997, **169**, 33–44.

50 R. B. Levy and M. Boudart, *Science*, 1973, **181**, 547–549.

51 Y. C. Kimmel, X. Xu, W. Yu, X. Yang and J. G. Chen, *ACS Catal.*, 2014, **4**, 1558–1562.

52 J. Monzó, D. F. van der Vliet, A. Yanson and P. Rodriguez, *Phys. Chem. Chem. Phys.*, 2016, **18**, 22407–22415.

53 M. D. Porosoff, X. Yang, J. A. Boscoboinik, and J. G. Chen, Angew. Chem. Int. Ed., 2014, **53**, 6705-6709.

54 Y. C. Kimmel, X. Xu, W. Yu, X. Yang, and J. G. Chen, *ACS Catalysis*, 2014, **4**, 1558-1562.

55 H. Chhina, S. Campbell and O. Kesler, *J. Power Sources*, 2007, **164**, 431-440.

56 R. Ganesan, and J. S. Lee, Angew. Chem. Int. Ed., 2005, **44**, 6557-6560.

57 Z. Hu, C. Chen, H. Meng, R. Wang, P. K. Shenand H. Fu, *Electrochem. Commun.*, 2011, **13**, 763-765.

58 J. Polonsky, I. M. Petruchina, E. Christensen, K. Bouzek, C. B. Prag, J. E. T. Andersen and N. J. Bjerrum, *Int. J. Hydrogen Energy*, 2012, 37, 2173-2181.

59 M. Horigome, K. Kobayashi and T. M. Suzuki, *Int. J. Hydrogen Energy*, 2007, **32**, 365-370.

60 A. Lewara, L. Timperman, A. Roguska and N. Alonso-Vante, *J. Phys. Chem. C*, 2011, **115**, 20153-20159.

CHAPTER 2

Aim and specific objectives of the thesis

As it was mentioned in the previous chapter, reducing the emission of CO_2 and the decrease of energy demand are main challenges of the society. One solution is the development of new technologies based on renewable sources of energy for transportation applications such as Fuel Cells and batteries. This thesis tackles one of the main challenges in the development and implementation of fuel cells for automotive applications.

The overall aim of this thesis is the development of Pt-based catalyst with long-term durability for Polymer Electrolyte Fuel Cell applications. In order to achieve this goal, we will implement transition metal carbides as support materials replacing the commonly used carbon support. A brief description and objectives of each chapter is presented below:

Chapter 3

One of the main challenges when developing new catalyst is to stablish a consistent protocol for the evaluation of the composition and properties of the materials. This chapter present a new methodology for understanding the degradation mechanisms of the catalysts. Since electrochemical measurements are not a sufficient tool to fully describe the degradation mechanism, I have combined electrochemical measurements and X-ray fluorescence technique. On one hand, electrochemical measurements provided the values of the

electrochemical surface area as a function of time for each degradation protocol, while the spectroscopic measurements provide the change in relative composition of the catalyst. As a new analytical tool was developed, the measurements had to provide statistical meaning and the reproducibility and report of errors was key. The validation of this technique was performed using unsupported Pt nanoparticles, Pt nanoparticles supported on carbon and Pt nanoparticles supported on TaC. This methodology allowed to assess the degradation mechanism of the active metal catalyst as well as the stability of the support material.

Chapter 4

The Chapter 4 implemented the protocol developed in Chapter 3 to evaluate the activity and durability of Pt nanocatalyst supported on a series of transition metal carbides. I face two main challenges in this chapter: 1) the synthesis of transition metal nitrides nanoparticles with a reduced particles size and large porosity; 2) the attachment and stabilization of the Pt nanoparticles to the support material. The first challenges is highly important as a support materials should have large surface area for a good dispersion of the nanoparticles, and high porosity for a good diffusion of the gas catalyst and water management. A serial of transition metal carbides with high surface area were synthesised and used as support material of Pt nanoparticles: TaC, VC and NbC. The preparation of the supported catalyst will be described in Chapter 4 .The stability and activity towards the ORR of these supported catalysts was assessed following the protocol described in Chapter 3.

Chapter 5

Since the Pt catalyst by itself are not the state-of-the-art catalyst in terms of activity and durability, I extend my studies to one of the best catalyst for ORR reported in the literature, PtCo alloy nanoparticles. Here one of the challenges was to obtain PtCo alloy nanoparticles with the ideal composition that show catalytic activities similar to those reported in the literature. To achieve this goal we implemented the water-in-oil method. The second main challenge was associated to the description of the degradation protocol for more than 3 metals. While Chapter 3 and 4, I had to follow the X-ray fluorescence signal of the Pt as well as the signals of the metal present in the carbide, in this chapter the precense of cobalt in the alloy add complexity to the analysis. In this chapter, I studied the durability and ORR activity of PtCo nanoparticles supported on NbC.

CHAPTER 3

Elucidating the degradation mechanism of the cathode catalyst of PEFCs by a combination of electrochemical methods and X-ray fluorescence spectroscopy

Format: Paper.

Information: J. Monzó, D. F. van der Vliet, A. Yanson and P. Rodriguez**,** *Phys. Chem. Chem. Phys.*, 2016,18, 22407-22415. – Published by the Royal Society of Chemistry.

Overview: In this paper we present a novel methodology for elucidating the degradation mechanisms of Pt-based catalysts under simulated PEFC conditions. This methodology uses in-depth cyclic voltammetry and X-ray fluorescence to measure the Electrochemical Surface Area (ECSA) and the Pt-content allowing us to distinguish between associative and dissociative mechanisms as a function of time and under Accelerated Stress Test (AST) conditions.

The first milestone in this thesis was to develop a powerful and widely accessible technique to understand the degradation processes within a catalyst layer under harsh oxidative conditions. The understanding of the degradation mechanisms of a catalyst, both catalyst active-metal and the support material deterioration, is the keystone for the design of new durable catalysts for PEFC applications. As explained in Chapter 1, there are few methods in the literature to study the catalyst degradation using expensive and complex set-up, however determining the exact degradation mechanism remains unclear. For this reason,

we decided to use cyclic voltammetry which is one of the most common techniques in an electrochemical laboratory and X-ray fluorescence which is a versatile technique employed in a wide range of disciplines as Chemistry, Geology or Physics for studying the stability of catalysts.

This paper covers the theoretical design and validation of a novel methodology for understanding catalyst deterioration. In addition, it covers the synthesis, characterization and durability study under AST conditions of Pt-based catalysts as unsupported Pt nanoparticles (Pt-Nps), Pt nanoparticles supported on carbon (Pt/Vulcan) and Pt nanoparticles dispersed on TaC (Pt/TaC).

This prepared catalyst, Pt/TaC, displayed a mass activity higher than Pt-Nps and Pt/Vulcan towards the oxygen reduction reaction. Besides, Pt/TaC presented an improved stability under AST conditions. The enhanced activity and improved durability of this catalyst open up a new opportunity to develop more durable catalysts using transition metal carbides as support materials for PEFC applications.

Overview: JM and PR designed the experimental set-up and JM carried out all the experiments. JM, DV, AY and PR analysed the data and wrote the paper. All the authors contributed to the final version of the manuscript.

Section 1. Microscopic confirmation of homogeneous catalyst layer.

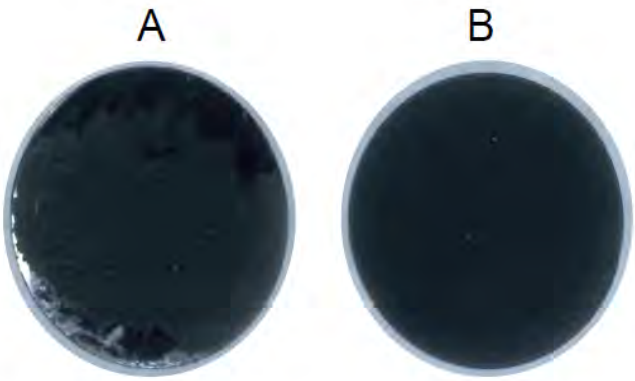

Figure SI1. Optical micrograph of the film obtained using (A) the one-drop casting method and (B) the film obtained using the multi-drop casting method proposed in this work.

Section 2. Experimental design to determine Pt content within the catalyst layer.

In order to establish a relationship between the electrochemical surface area (ECSA) and Pt content, to distinguish between associative and dissociative processes, the Pt content of the catalyst layer on the disk was determined by X-ray fluorescence (XRF). After a well-defined number of degradation cycles, the working electrode was placed in a XRF spectrometer and the Pt content was resolved. To reduce the background noise, the best scan quality provided by the equipment was employed for all the measurement carried out in this work. These measurements took 25 minutes each under helium atmosphere.

After the Pt content characterization, the carbon disk was polished with 0.05 μm alumina to remove all the catalyst from the carbon disk surface. After the polishing, the carbon disk was sonicated for 10 minutes and dried in an air-flow oven at 55 °C. In order to confirm the absence of any remaining catalyst on the carbon surface, the disk was characterized by XRF prior to its next use. Then, a new thin catalyst layer was prepared to proceed with the degradation protocols.

Section 3. Calibration curve and limit of detection for Pt content.

In order to establish a relationship between the XRF response and the Pt content, an experimental calibration curve was constructed. A certain volume of Pt solution with a well-known concentration of Pt (125 µg mL^{-1}) was deposited on a zero response carbon disk and allowed to evaporate in air. The dried carbon disk was then analysed by XRF with each Pt loading on the disk investigated in triplicate (table SI1).

Table SI1. Experimental data for Pt calibration curve.

Mass $_{Pt}$ ± 0.1 (µg)	Net intensity ± 1 (Cps)		
8.0	1464	1515	1634
6.9	1408	1427	1339
5.9	1195	1253	1199
4.8	951	868	960
3.7	729	762	799
2.6	618	515	614
1.5	315	335	355
0.7	234	167	177
1.2	275	290	230
2.2	399	490	465

Figure SI2 shows the calibration plot using the net intensity of $Pt_{L\alpha}$ signal (9.45 KeV) as a function of the mass of Pt deposited on the carbon disk. As can be seen, the response of the intensity is linearly proportional to the mass of Pt with a correlation coefficient of 0.996.

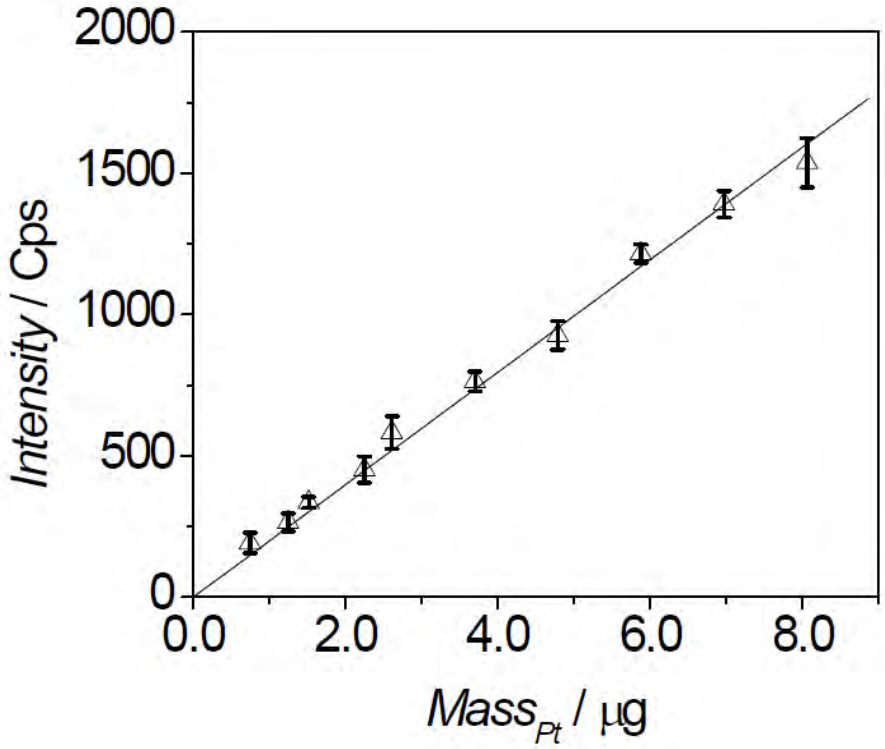

Figure SI2. Calibration data for Pt detection by XRF spectrometer (gradient = 199 ± 3 Cps μg^{-1}, R^2 = 0.998).

5

Section 4. Calibration curve and limit of detection for TaC content.

In order to establish a relationship between the XRF response and the TaC content, an experimental calibration curve was constructed. The protocol followed was the same used for the calibration curve of detection of Pt, section 3.

Table SI2. Experimental data for TaC calibration curve.

Mass $_{Pt}$ ± 0.1 (µg)	Net intensity ± 1 (Cps)		
23.5	1464	1515	1634
19.3	1408	1427	1339
34.5	1195	1253	1199
41.4	951	868	960

Figure SI3 shows the calibration plot using the net intensity of $TaC_{L\alpha}$ signal (8.45 KeV) as a function of the mass of TaC deposited on the carbon disk.

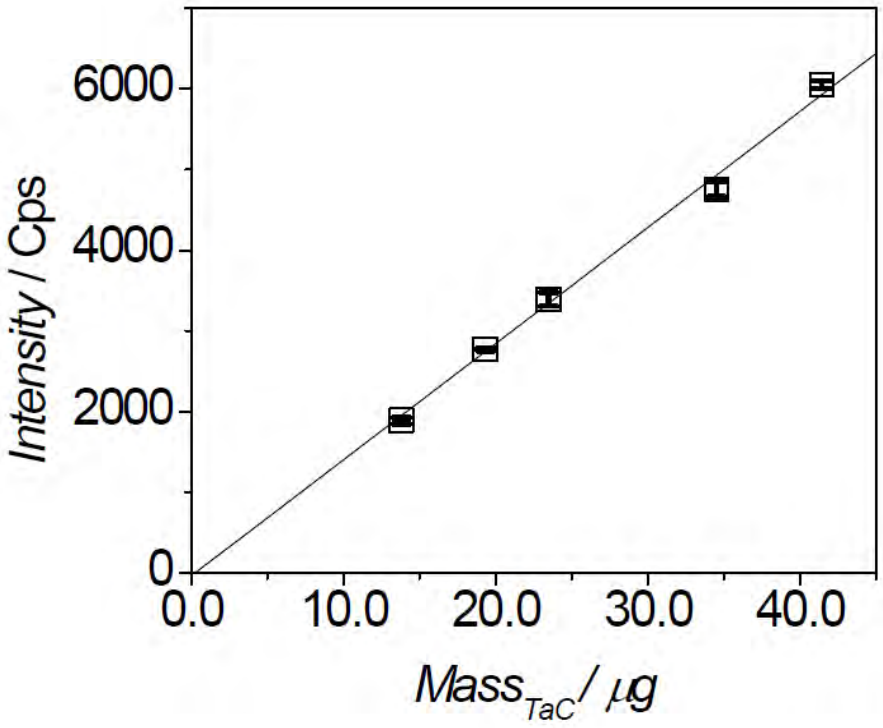

Figure SI3. Calibration data for TaC detection by XRF spectrometer (gradient = 144 ± 4 Cps μg^{-1}, $R^2 = 0.999$).

7

Section 5. Particle size distribution of Pt-Nps.

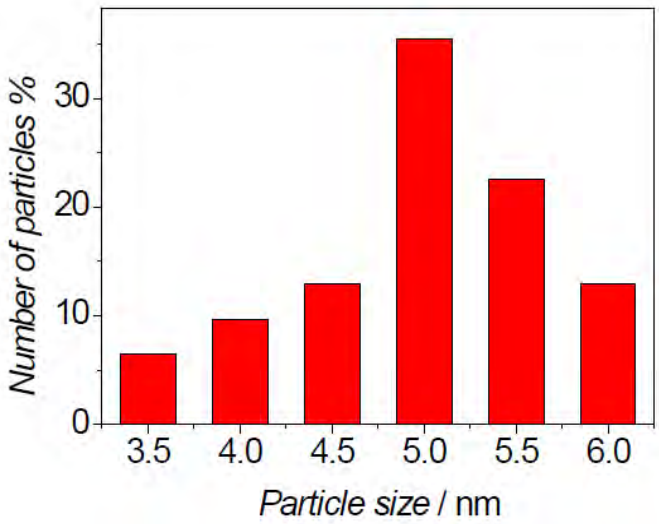

Figure SI4. Particle size distribution of Pt-Nps obtained from TEM measurements. The relative abundance of each particle size was calculated from a total of 175 nanoparticles.

Section 6. Compositional analysis of Pt/TaC by XRF.

A layer of Pt/TaC was deposited on the surface of a zero background response carbon disk. Then, this carbon disk was placed in a XRF spectrometer, acquiring the composition of this prepared catalyst. The compositional analysis was done in triplicate, resulting in a composition of (19.6 ± 0.8) % Pt and (80.4 ± 0.8) % Ta.

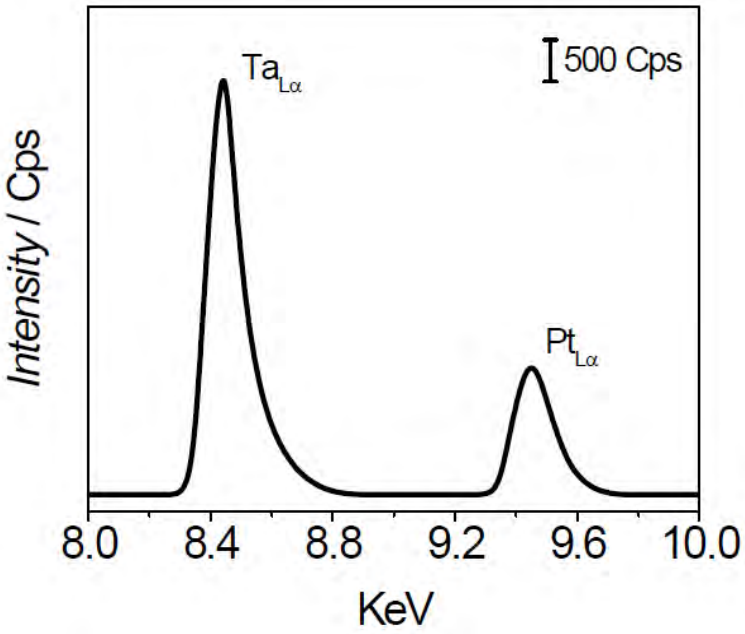

Figure SI5. X-ray fluorescence spectra of Pt nanoparticles supported on TaC. The signals at 8.45 keV and 9.45 keV are associated to $Ta_{L\alpha}$ and $Pt_{L\alpha}$ respectively. In order to present clear results, the original data was digitalized using the *GraphClick* software. Original data is available upon request.

Section 7. Physical characterization of Pt/Vulcan catalyst.

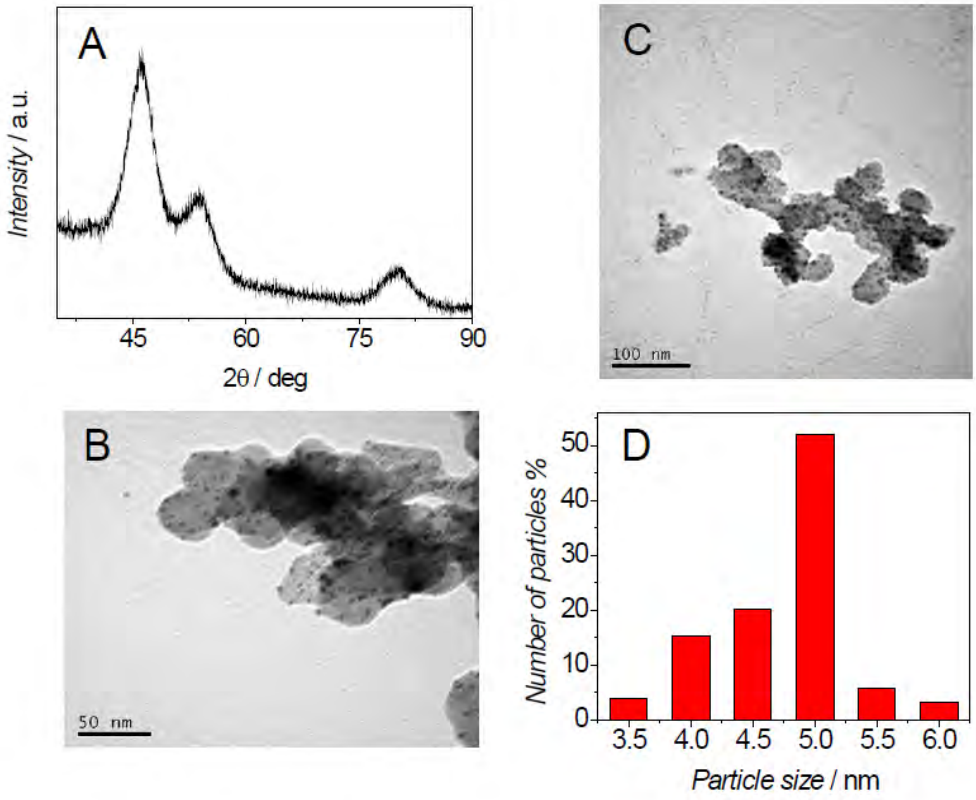

Figure SI6. (A) XRD pattern, (B-C) TEM images and (D) particle size distribution of Pt/Vulcan catalyst. The relative abundance of each particle size was calculated from a total of 175 nanoparticles.

10

Section 8. ORR Tafel plots of the catalysts: Pt-Nps, Pt/Vulcan and Pt/TaC.

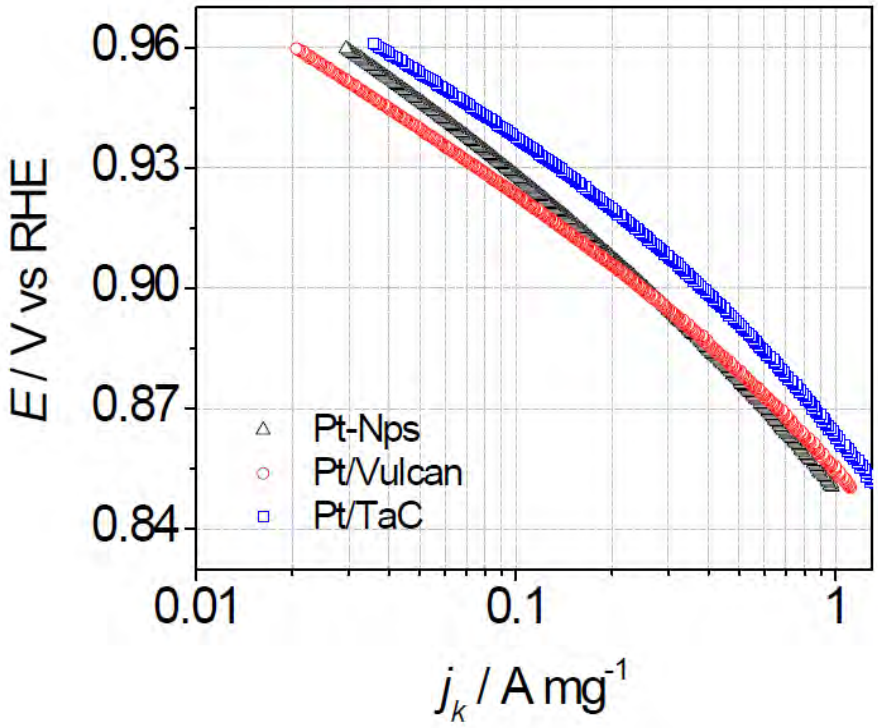

Figure SI7. Mass activity, j_k, for the ORR on Pt-Nps , Pt/Vulcan and Pt/TaC, data are shown for the positive-going sweep at 20 mVs^{-1} in O_2-saturated 0.1 M $HClO_4$ at 1600 rpm.

Section 9. Study of the mechanical stability of the Nafion-free catalyst layer.

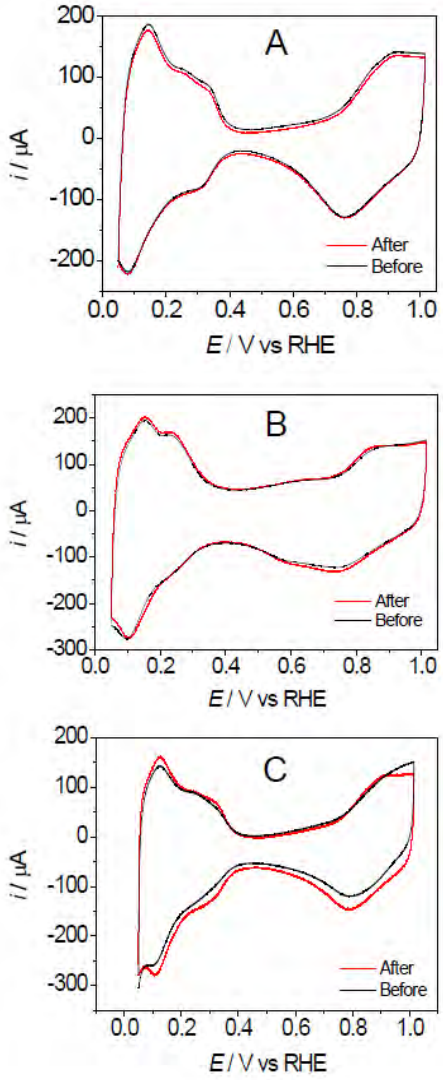

Figure SI8. Voltammetric profiles of Pt-nps (A), Pt/Vulcan (B) and Pt/TaC (C) before (black line) and after (red dashed line) mechanical stress evaluation. The catalysts were rotated at 300 rpm in 0.1 M $HClO_4$ during 5 hours at open circuit potential. The voltammograms were carried out in 0.1 M $HClO_4$ at 50 mVs^{-1}.

Section 10. Fluorescence spectra of the catalyst layer as a function of number of cycles during the load cycle protocol.

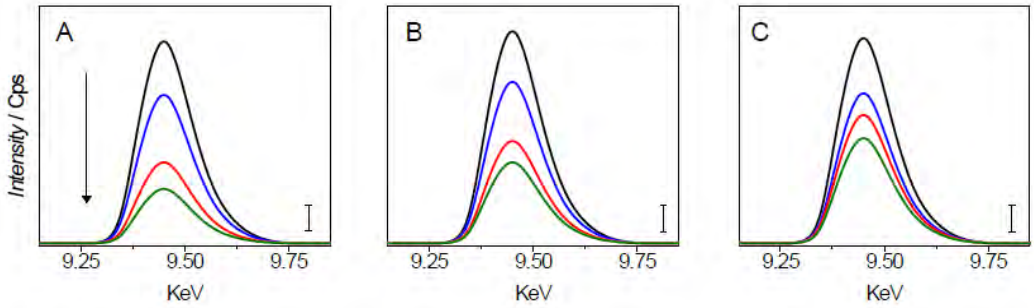

Figure SI9. X-ray fluorescence spectra ($Pt_{L\alpha}$) of Pt-Nps (A), Pt/Vulcan (B) and Pt/TaC (C) at different stages of the load cycle protocol; 0 cycles (black line), 2000 (blue line), 6000 cycles (red line) and 10000 cycles (green line). The scale bar corresponds to 100 Cps intensity. In order to present clear results, the original data was digitalized using the *GraphClick* software. Original data is available on request.

Section 11. Average of the particle size of each catalyst as a function of number of cycles during the load cycle protocol and shut-up/shut-down protocol.

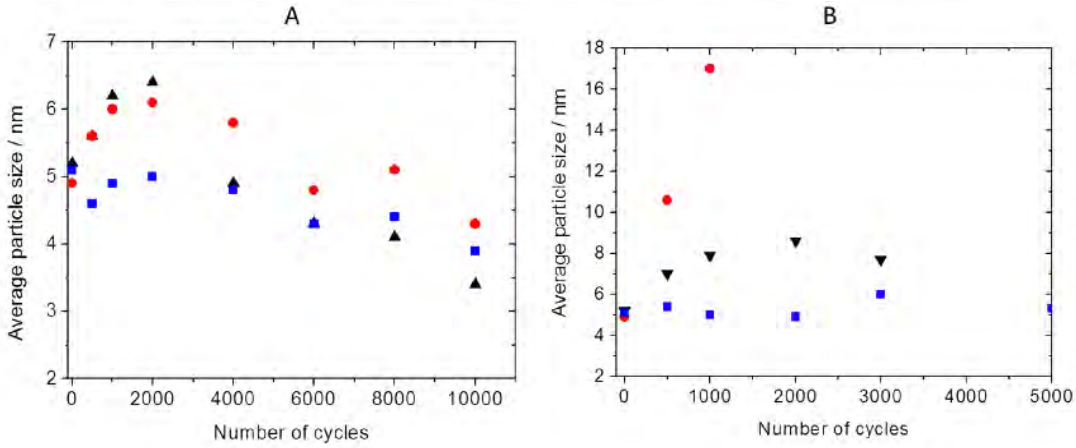

Figure SI 10. Average particle size of the Pt nanoparticles calculated from the mass of platinum and the ECSA as a function of the number of cycles for (A) load cycle protocol and (B) start-up/shut-down protocol. Pt-Nps (black), Pt/TaC (blue) and Pt/Vulcan (red).

Section 12. ORR Tafel plots as a function of number of cycles during the load cycle protocol.

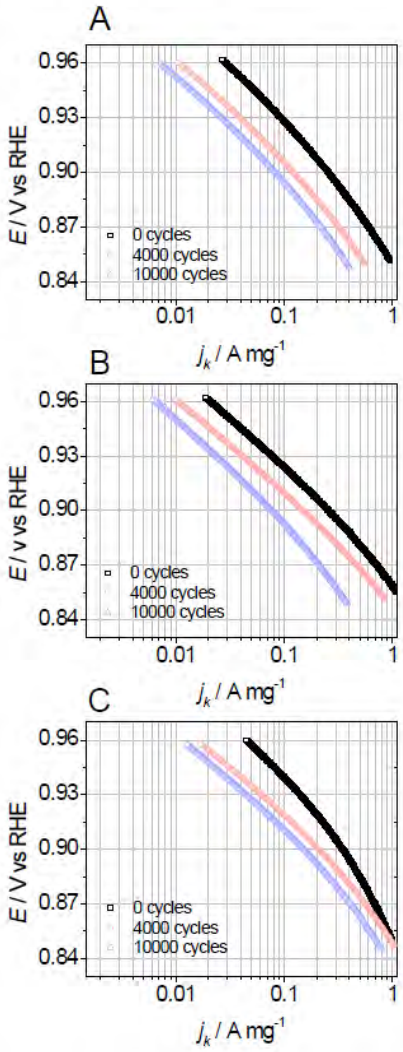

Figure SI11. Mass activity, j_k, for the ORR on Pt-Nps (A), Pt/Vulcan (B) and Pt/TaC (C) as a function of number of degradation cycles during the load cycle protocol. Data are shown for the positive-going sweep at 20 mVs^{-1} in O_2-saturated 0.1 M $HClO_4$ at 1600 rpm.

Section 13. Fluorescence spectra of the catalyst layer as a function of number of cycles during the start-up/shut-down protocol.

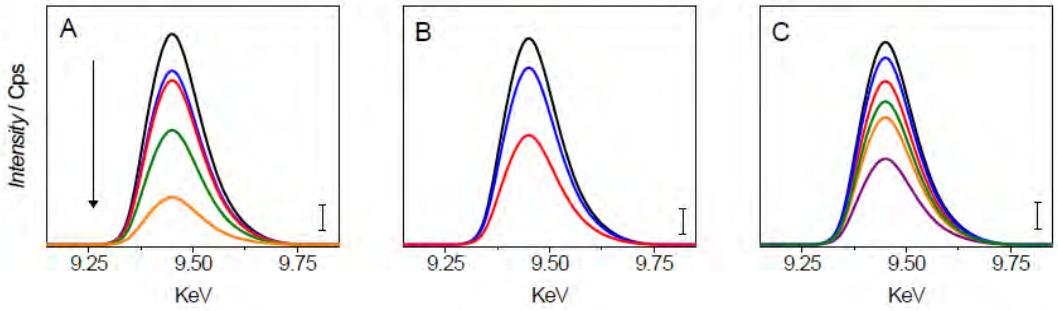

Figure SI12. X-ray fluorescence spectra of Pt-Nps (A), Pt/Vulcan (B) and Pt/TaC (C) at different stages of the start-up/shut-down protocol. 0 cycles (black line), 500 cycles (blue line), 1000 cycles (red line), 2000 cycles (green line), 3000 cycles (orange line) and 5000 cycles (purple line). The scale bar corresponds to 100 Cps intensity. In order to present clear results, the original data was digitalized using the *GraphClick* software. Original data is available on request.

Section 14. Fluorescence spectra of Pt/TaC ($Ta_{L\alpha}$) layer as a function of number of cycles during the start-up/shut-down protocol.

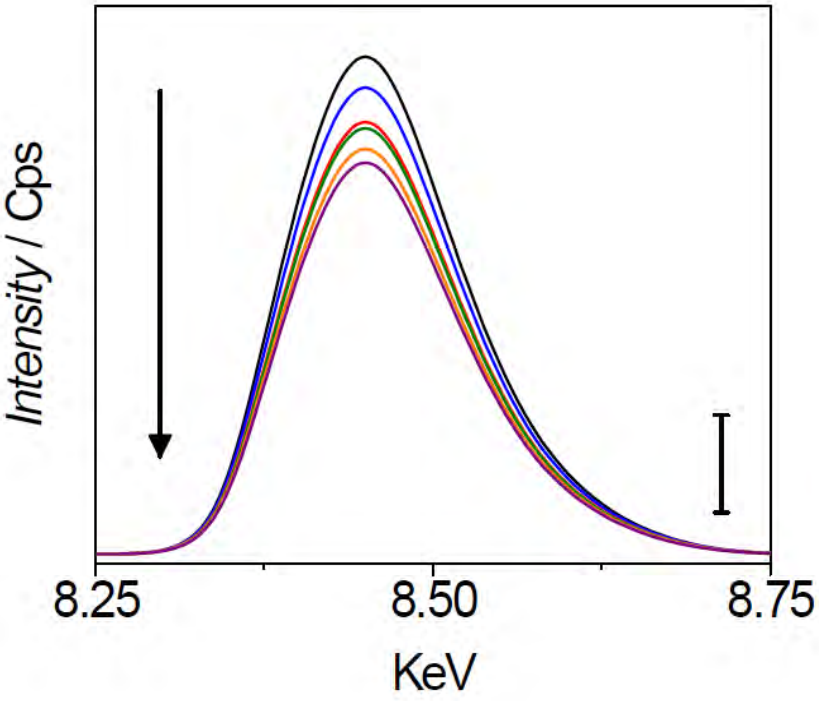

Figure SI13. X-ray fluorescence spectrum of Pt/TaC at different stages of the start-up/shut-down protocol. 0 cycles (black line), 500 cycles (blue line), 1000 cycles (red line), 2000 cycles (green line), 3000 cycles (orange line) and 5000 cycles (purple line). The scale bar corresponds to 500 Cps intensity. In order to present clear results, the original data was digitalized using the *GraphClick* software. Original data is available on request.

Section 15. ORR Tafel plots of catalysts as a function of number of cycles during the start-up/shut-down protocol.

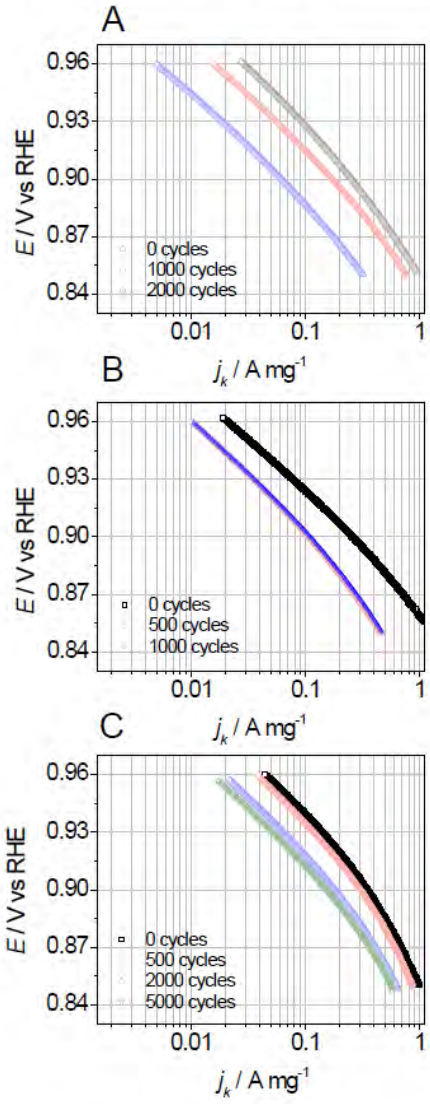

Figure SI14. Mass activities, j_k, for the ORR on Pt-Nps (A), Pt/Vulcan (B), and Pt/TaC (C) as a function of number of cycles during the start-up/shut-down protocol. Data are shown for the positive-going sweep at 20 mVs^{-1} in O_2-saturated 0.1 M $HClO_4$ at 1600 rpm.

CHAPTER 4

Transition metal carbides as alternative support materials for cathode catalyst in Polymer Electrolyte Fuel Cell

Format: Paper (unpublished).

Information: J. Monzó, A. Danks, J. Pampel, j. Solla-Gullon, T.-P. Fellinger Z. Schnepp and P. Rodriguez.

Overview: In this paper draft we present the synthesis and characterization of a series of transition metal carbides; NbC, VC and TaC. These transition metal carbides have been used as support materials of Pt nanoparticles in order to evaluate the ORR mass activity and the stability of the prepared catalysts.

On the basis of the result obtained in Chapter 3, Pt nanoparticles supported on TaC presented an enhancement of the ORR mass activity and an improvement of the stability under oxidative conditions. We decided to synthesis transition metal carbides (TMC) with high surface area as the minimum requirement for potential support materials is 50 m^2g^{-1}. Pt nanoparticles of 5 nm were dispersed on the TMC and the stability and ORR mass activity was assessed; Pt/NbC emerged as a proper catalyst candidate because it presented a 1.7-fold enhancement of ORR mass activity. Additionally, Pt/NbC was shown to be more stable than the common commercial catalyst Pt/C.

Overview: JM and PR designed the electrochemical experiments and JM carried out all the experiments. JM, AD, ZS, JP and TF designed the synthesis of TMC and JM carried out the synthesis. JM analysed the data and wrote the paper.

Transition metal carbides as alternative support materials for cathode catalyst in Polymer Electrolyte Fuel Cell

Javier Monzó[a], Ashleigh Danks[a], Jonas Pampel[b], Jose Solla-Gullon [c],Tim-P. Fellinger[d], Zoe Schnepp[a] and Paramaconi Rodriguez*, [a].

[a]School of Chemistry, University of Birmingham, Edgbaston, B15 2TT, Birmingham, England.

[b]Max Planck Institute of Colloids and Interfaces, Department of Colloid Chemistry, Potsdam, Germany.

[c]Institute of Electrochemistry, University of Alicante 03080, Alicante (Spain).

[d]Chalmers University of Technology, Department of Chemistry and Chemical Engineering, Göteborg, Sweden.

Corresponding author: p.b.rodriguez@bham.ac.uk

Abstract

In this work we report the synthesis and characterization of transition metal carbides (TMC): VC, NbC and TaC and its use as a support material for platinum catalyst. The Pt supported catalyst on the metal carbides catalysts showed an enhancement of the mass activity of 1.9 times (Pt/VC), 1.7 times (Pt/NbC) and 1.4 (Pt/TaC) in comparison to the commercial catalysts Pt/C. Accelerated stress protocol (ASP) under shut-up/shut-down conditions (0.5 V to 1.5 V vs RHE) showed that Pt/NbC was the most stable catalysts. The degradation mechanism of the Pt supported catalyst on metal carbides was also determined by combination of electrochemical methods and X-ray fluorescence spectroscopy. We proposed that the enhancement in the catalytic activity and improved durability of the Pt catalyst supported on the TMC is associated to capacitive electronic metal-support interactions between the support and the Pt nanoparticles.

1. Introduction

Low-temperature fuel cell technology is proposed candidate for the replacement of traditional combustion engine for automotive applications.[1,2] However, the durability and cost of polymer electrolyte membrane fuel cells (PEFCs) is a limiting factor for its wide commercialization.[3,4] The common catalyst employed in PEFC is a Pt-based catalyst composed of Pt nanoparticles dispersed on carbon with high surface area.[5,6]

Although carbon supports are known to be thermodynamically unstable, they are still the catalyst support of choice for PEFC electrocatalysts for the following reasons:

1. High electronic conductivity: approximately 2 $S \cdot cm^{-1}$ or higher.

2. High specific surface area: 50 to 800 $m^2\ g^{-1}$.

3. Highly porous structures: pore sizes between 20 to 100 nm for gas diffusion electrodes.

However, in automotive fuel cell applications, high potentials regularly occur, causing a change in the morphology of the carbon support. In fuel cell applications, different driving cycles indicate that, during the fuel cell system's life of 5000 hours, approximately 300,000 cycles between 0.7 V and 0.9 V will be performed.[3] In addition, the cathode can reach values as high as 1.5 V during start/stop cycles.[7,8] As a result of these high potentials, severe oxidation of the cathode can take place, leading not only to loss of carbon surface area and detachment of Pt nanoparticles, but also to

complete deterioration of the catalyst. This results in rapid failure of the fuel cell.[4,9]

The development of durable metal-catalyst as Pt-alloys[10–12] and the development of more stable support materials or improvement of the interaction between the metal-catalyst and the support are the major challenges of the PEFCs .[13] Among of the possible support materials, transition metal carbides (TMCs) are emerging as promising alternative support materials due to their high conductivity, high mechanical and chemical resistivity and potential electronic properties.[14] Their electronic properties are like noble metals, which can promote an electron transfer from TMCs to the supported metal catalyst improving its catalytic activity towards oxygen reduction reaction (ORR).[15] Additionally, TMCs are stable in the operation conditions for the oxygen reduction reaction, enhancing the expected catalyst lifetime.[16]

Three somehow forbidden conditions that a support material should present for its implementation on PEFC are the surface area, porosity and the hydrophobicity. In order to obtain reasonably high Pt Nps dispersions in the support materials of the surface area of the support should at least be in the range of graphitized carbon blacks, which are typically >50 m^2/g carbon. The catalyst support should be able to form porous structures in the catalyst layer. Current porosities of carbon black electrodes have pores in the order of 20-100 nm range.[17] The required pore sizes for a new support material should be larger than at least 25 nm under typical PEFC operating temperatures and pressures. The balance of hydrophobic and

hydrophilic properties of the support materials is also important in the design of gas diffusion electrodes (GDE) on PEFC. On one hand, the presence of water produce during the ORR strongly affects the gas diffusion towards the electrode but on the other hand the lack of water could result in the decrease of the ionic conductivity of the Nafion membrane. The gas diffusion layer on the cathode side of PEMFC requires generally hydrophobic support materials. For an acceptable water management the contact angle of the support should be > 120° where the contact angle on the Pt/Vulcan is 135°[18] and other hydrophobic carbons is around 130-150°.[19]

Previous works have discussed the utilization of carbide materials as a support for the cathode catalyst in PEFC, however those works have implemented large TMC particles and have not paid attention either the structural requirements of porosity and surface area, to the electrochemical stability or the electronic effect.[20,21] Given the recent advanced in the synthesis of metal carbide materials with large surface area and porous structures, this work will implement this method of synthesis to prepare TMC and evaluate its electrochemical properties as support materials on a cathode for PEFC.[22]

This work presents the synthesis and characterization of transition metal carbides with high surface area. The catalytic activity and stability of Pt-Nps dispersed on the synthetized VC, NbC and TaC were evaluated in a thin-film rotating disk configuration and following accelerated stress protocol (0.5 V to 1.5 V vs RHE) established by the department of energy (DoE).[23]

The time-dependence degradation mechanisms of the catalysts was studied using the methodology developed in a previous work.[21]

2. Experimental section

2.1. Synthesis of transition metal carbides

TMCs carbides were synthesized using the method developed by Giordano et al. so-called “urea route".[22,24] In brief, a metal salt precursor was dissolved in ethanol to obtain a concentration of 10 wt. % of the metal salt. A given amount of urea as indicated in table 1 was dissolved into the 10 mL of the solution and the ethanol was evaporated inside an air oven at 80 ºC. The dried sample was calcinated in a tubular furnace under N_2 atmosphere at 900 ºC during 2 hours.

Table 1 Conditions of synthesis of the different samples of metal carbides. It has to be considered that the volume of metal salt (VMS) is based in a 10 wt. % metal salt concentration in ethanol.

Desired product	Metal salt	VMS (mL)	Urea (g)	Ratio (metal:urea)
VC	$VOCl_3$	5	1.21	7
NbC	$NbCl_5$	5	0.78	7
TaC	$TaCl_5$	5	0.85	10

2.2. Preparation of catalyst inks

Platinum nanoparticles were synthesized following the water-in-oil (w/o) microemulsion method previously reported.[25,26] A salt of Pt (H_2PtCl_4) was reduced using sodium borohydride inside of the water phase. After the complete reduction of Pt^{+2} to Pt^0, Pt-Nps were precipitated with acetone

and collected by centrifugation. Then, Pt-Nps were cleaned with diluted solution of acetone:water and stored in ultra-pure water as described in the literature.

The catalyst inks with 20 wt.% Pt were prepared following the protocol reported by Monzó et al.[21] Briefly, 0.01 g of Pt-Nps were dispersed in a water solution containing 0.04 g of TMCs. The resulting solution was stirred overnight and the catalyst (Pt/TMC) was cleaned several times with ElgaPureUltra water and collected by precipitation. A given amount of Pt/TMC was dispersed in water in order to obtain a catalyst concentration of 0.0014 g mL^{-1}.

All the catalyst were evaluated and compared against Pt/Vulcan (20 wt. %Pt, ETEK). The catalyst ink was prepared using 0.007 g of Pt/Vulcan dispersed in 20 mL of ElgaPureUltra water with a final concentration of $7 \cdot 10^{-5}$ g mL^{-1}.

2.3. Physical characterization

The Pt-Nps, VC, NbC, TaC and Pt/C were characterized by Transmission Electron Microscopy (TEM) using a JEOL JEM 1200 EX MKI instrument. The samples were prepared by drop-casting ethanolic suspensions of the catalysts on carbon coated copper grids.

The catalyst crystalline structure of the catalyst was determined using a Bruker AXS D2 PHASER diffractometer with a Co-Ka (0.179 nm) radiation source. A small amount of the catalysts was dried under Ar flow on a zero background SiO holder (MTI).

The composition of the catalysts was determined by X-ray fluorescence (XRF) using Bruker S8 Tiger 4 kW spectrometer.

The surface area of the transition metal carbides was determined using a Quantachrome Quadrasorb equipment. The BET surface was calculated using the N_2 adsorption at 77 K.

2.4. Electrochemical measurements

In order to study the ECSA and the catalytic activity towards the ORR, the thin film method was employed in a rotating disk electrode configuration.[27] The working electrode consisted of a disk of glassy carbon (diameter = 5 mm), on which a film of the catalyst was deposited to obtain a final loading of 30 μg·Pt cm^{-2}. It is crucial to obtain a homogeneous catalyst layer on the electrode, in order to have uniform O_2 diffusion, and accordingly an appropriate diffusion limited current, which is geometry dependent. The deposition of the catalysts on the carbon disk was performed by drop casting and drying several small aliquots of the catalyst suspensions, rather than a single large drop. The resulting homogeneous catalyst layer was confirmed microscopically as described before.[21]

In this work, the catalyst layer has been prepared without Nafion to prevent oxygen transport resistance, electronic resistance and sulfonate adsorption.[28,29]

The potentials were controlled with an Autolab PGSTAT12 potentiostat. A Au wire with high surface area was used as a counter electrode and the Ag/AgCl electrode as a reference. All the potentials are reported versus to

the reversible hydrogen electrode (RHE). All the electrochemical measurements were carried out in a electrolyte solution of 0.1 M $HClO_4$ (Suprapure, Merck), prepared with ultra-pure water (ElgaPureUltra, 18.2 MO cm, 1 ppb total organic carbon).

In order to study the stability of the catalyst, the catalysts were evaluated under the shut-up/shut-down Accelerated Stress Protocol (ASP) conditions. In brief, the electrode was cycled 5000 times between 0.5 V to 1.5 V vs RHE with a scan rate of 50 mV s^{-1}. Initial studies performed in our laboratory showed that the formation/accumulation of bubbles under the RDE electrode (due to carbon oxidation to CO_2) might lead to inaccurate measurements of the ECSA and irreproducible results. Therefore, for proper comparison with the Pt/C_{vulcan} all the ASPs presented here were performed with 300 rpm rotation. After a defined number of degradation cycles, the ECSA and the ORR polarization curves were acquired in a fresh solution. The ECSA and Pt content were determined at different stages of the protocol using the hydrogen adsorption/desorption region and XRF as it is described in appendix I and appendix II.

3. Results and discussion

3.1. Characterization of transition metal carbides

Figure 1 shows the XRD pattern of the as synthetized VC, NbC and TaC nanoparticles. The 2Θ signals at 43.76, 51.11 and 75.19 are in agreement with the PDF card 01-089-7382 of the VC.(Figure 1A) The XRD pattern of NbC (Figure 1B), with 2Θ angles at 35.49, 41.13, 59.58, 71.06 and 74.83, is in agreement with the PDF Card - 00-002-1031 and correspond to the precense of NbC. The pattern on figure 1C ,2Θ = 40.76, 47.53, 69.55, 83.80 and 88.37, is in agreement with the presence of TaC crystals (PDF Card - 03-065-7114). It is important to note that signals associated with the

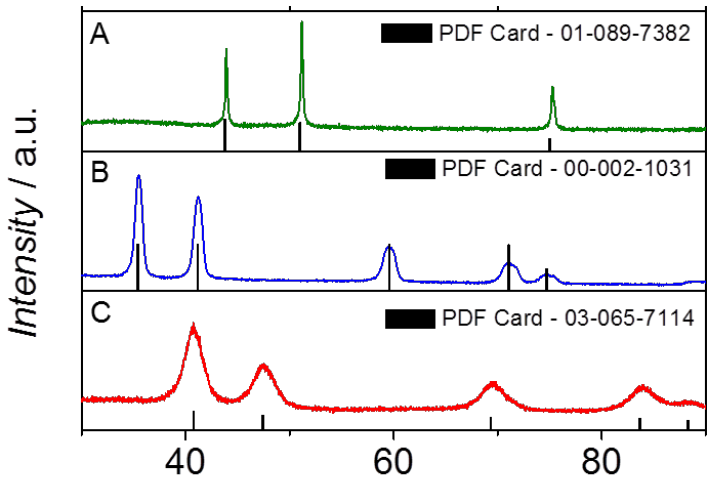

Figure 1 X-ray diffraction patterns of VC (A), NbC (B) and TaC (C). The database pattern for each sample has been included.

reactants from the synthesis or other side products were not detected, confirming the purity of the final carbide support material.

The structural characterization of the support materials was complemented by TEM (Figure 2). The particle size distribution is shown in figure SI1. Figure 2A shows the TEM image of VC which is composed of spherical

nanoparticles with and average size of 50 nm diameter. Similarly, the NbC nanoparticles present a spherical shape but the average particle size was significantly smaller: 10 nm diameter (Figure 2B). The TEM image on figure 2C spherical TaC nanoparticles with particle size of 7 nm diameter. The control Pt/Vulcan catalyst was also characterized by XRD and TEM as shown in figure SI3. TEM characterization indicates a size distribution for the Pt nanoparticles of (5 ± 1) nm dispersed in porous carbon, it is in good agreement with previous published results.[21]

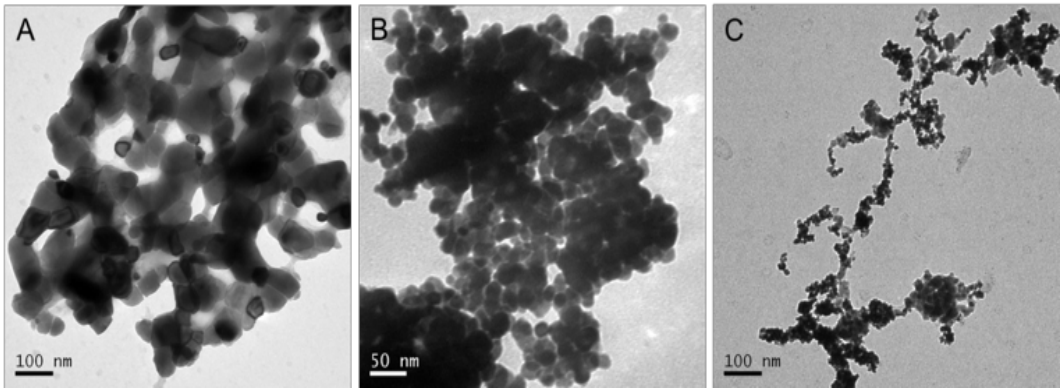

Figure 2 TEM images of the transition metal carbides synthesised: VC (A), NbC (B) and TaC (C).

Given the importance of the water management in the optimal performance of the cathode catalyst of PEMFC, the hydrophobicity of the catalyst was measured by determining the contact angle of the catalyst with a water droplet. Images of water droplets on the surface of TMC layer are shown in figure 3. By fitting a tangent to three-phase point where liquid surface touches the solid surface the contact angle was measured. Because there is no nafion agent added to the TMC films, the contact angles on the surface of TMC provides the information of the materials and no other additives. The contact angle for VC, NbC and TaC is 140.8 ± 0.3, 145.8 ±

0.5 and 143.3 ± 0.3, respectively. This contact angle values are comparable with the carbon Vulcan[18] (135°) which makes this carbides support suitable for PEFC applications.

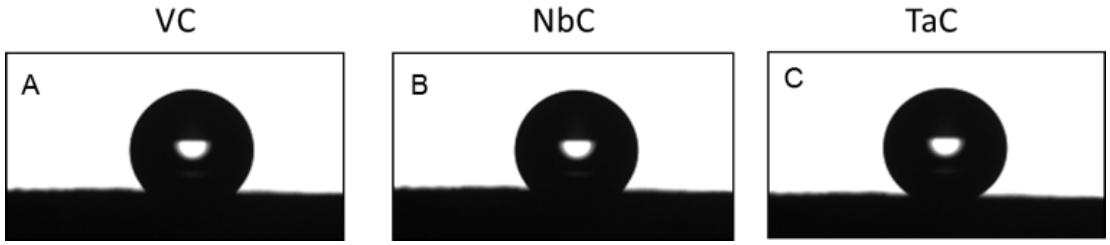

Figure 3 Optical images of a water drop on a monolayer of VC (A), NbC (B) and TaC(C). The contact angle is internal angle that the drop forms with the surface.

As it was mentioned in the introduction, other important property of the catalyst support for the PEFC is the surface area. The surface area of the TMC was calculated from the nitrogen adsorption isotherms (Figure SI2). The surface area of the VC is 51 $m^2 g^{-1}$, for NbC is 76 $m^2 g^{-1}$ and 68 $m^2 g^{-1}$ for TaC. All the TMC present a surface area larger than 50 $m^2 g^{-1}$ which is the minimum required for support materials.[21]

3.2. Characterization of Pt-based catalyst

Prior to the dispersion of the Pt nanoparticles in the metal carbide support, the as-synthetized Pt-Nps nanoparticles were characterized by XRD (Figure SI4.). From the XRD pattern and using the Scherer equation it was determine that the Pt nanoparticles are 5nm diameter which was confirmed later by TEM. After the dispersion of the Pt nanoparticles on the TMC following the procedure described in the experimental methods, the supported nanoparticles were characterize by TEM. Figures 4A-C show the TEM images for Pt/VC, Pt/NbC and Pt/TaC. Unfortunately, due to the similar molecular weight of the Pt and the TaC and NbC, it is very difficult

to distinguish the interface between both materials. In the case of Pt/VC, 5 nm Pt nanoparticles can be observed surrounding the much larger VC particles. However, for Pt/NbC and Pt/TaC catalysts is difficult to differentiate between the carbide and the Pt nanoparticles due to similar particle size. The presence of Pt-Nps is confirmed by the XRD patterns (Figure SI5). The signals at 2Θ = 46.57, 53.34, 80.20, 98.33 and 104.44 confirm the presence of Pt in the three catalysts (PDF Card - 01-089-7382). The composition of the prepared catalysts was confirmed by XRF; 20 % Pt and 80 % NbC, 19 % Pt and 81 % VC and 21 % Pt and 79 % TaC were confirmed by XRF (Figure SI6).

3.3. Electrochemical evaluation of the Pt supported nanoparticles on TMC towards the oxygen reduction reaction in acidic media

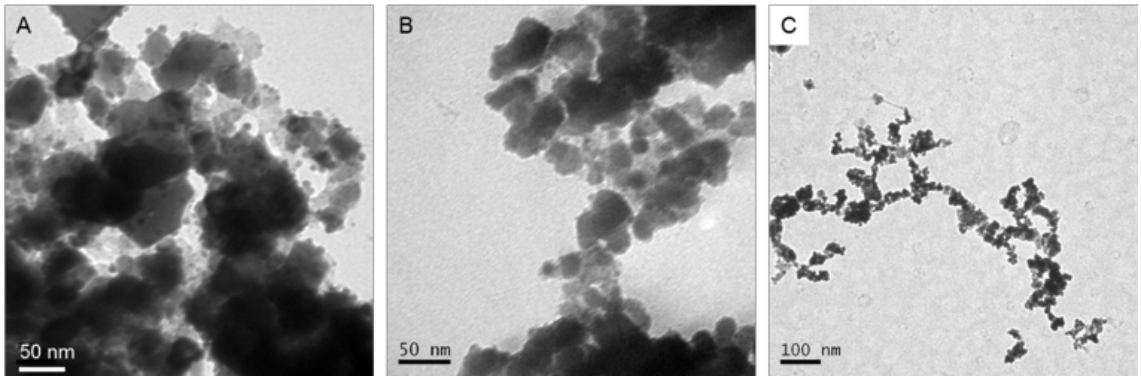

Figure 4 TEM images of Pt-based catalysts prepared: Pt/VC (A), Pt/NbC (B) and Pt/TaC (C).

Figure 5A shows the voltammetric profiles in 0.1 M $HClO_4$ of the 3 Pt/TMC catalysts and the Pt/C_{vulcan}. The voltammetric profiles of all the catalyst present the typical features of $H_{ads/des}$ and oxide formation and reduction in agreement with previous literature. The electrochemical surface area (ECSA) was calculated following well-stablish procedure using the $H_{ads/des}$ region after double layer subtraction. For both Pt/VC and Pt/NbC the

calculated ECSA is 53 m^2 g^{-1} and for Pt/TaC is 48 m^2 g^{-1}. The resulting values of the ECSA are closed to theoretical value of 55.85 m^2 g^{-1} for spherical Pt-Nps of 5 nm, which confirm that most of the Pt catalyst deposited on the carbide materials is accessible to the electrolyte. Figure 5B shows the oxygen reduction reaction (ORR polarization curves of the catalysts in 0.1 M $HClO_4$ under mass transport conditions in a RDE electrode at a rotation speed of 1600 RPM. The 2 distinctive regions for the ORR polarization curves can be distinguish for all the catalyst: diffusion control region (between 0.1-0.8 V vs RHE) and the kinetic control region (between 0.85-1 V RHE). Figure SI7 shows the Tafel curves for each catalyst in the kinetic control region. As can be seen, all the platinum catalyst supported on the TMC shows higher catalytic activity in comparison with the commercial Pt supported on carbon Vulcan, being the Pt/VC the catalyst with higher catalytic activity.

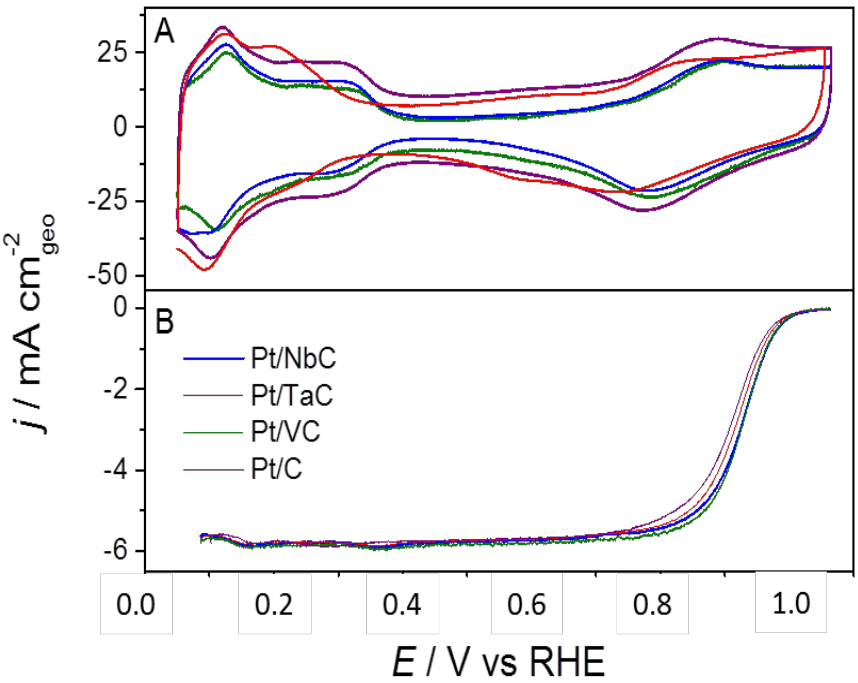

Figure 5 (A) Voltammetric profiles of catalysts in Ar atmosphere and (B) ORR polarization curves in 0.1 M $HClO_4$ satured with O_2 at 20 mV/s. ORR polarization curves were Ohmic drop corrected and the background from capacitative process at the blank was subtracted.

The mass activity was calculated from the measured current (j) and the diffusion current (j_d) using the modified Koutecky-Levich[21] equation (Eq. 1):

$$j_k = \frac{j_d \cdot j}{j_{d-j}} \quad (1)$$

Table 1 summarizes the initial conditions of ECSA and mass activity for each of the catalyst. As can be seen the ORR mass activity of the Pt/VC, Pt/NbC and Pt/TaC show a 1.9, 1.7 and 1.4-fold improvement over the Pt/C. This enhancement of the mass activity could by associated with a strong-metal-support-interaction (SMSI).[30,31] Recently, Binninger et al. has proposed the concept of capacitive electronic metal-support interactions for catalyst particles at the nanometer scale, where electronic equilibration results in a long-range charging of the catalytically active outer surface.[30,31] In supported nanocatalyst, the long-range charge transfer result into a shift of the local work function at the outer surface of the platinum nanoparticle causing an enhancement in the catalytic activity towards the ORR.

Table 2 Initial conditions of the catalysts under study prior the degradation protocol.

Catalyst	Pt/VC	Pt/NbC	Pt/TaC	Pt/C
ECSA ($m^2\ g^{-1}$)	53	53	48	57
$Pt_{content}$ (wt. %)	20	19	21	20
Mass activity ($A\ mg^{-1}_{Pt}$)@0.09 V vs RHE	0.49	0.46	0.34	0.25

3.4. Evaluation of the stability of the Pt/TMC catalyst under shut-up/shut-down accelerated stress protocol (ASP) conditions

The ECSA of the catalyst as a function of time under the ASP was determined by measuring the $H_{ads/des}$ region in a 0.1 M $HClO_4$ solution (See appendix I for more information). Figure 6A-C shows the blank voltammograms of the catalysts at different stages of the shut-up/shut-down protocol. As can be seen, the features associated to the $H_{Ads/Des}$ and Pt-oxides decrease as a function of number of cycles for all the Pt/TMC catalyst. Figure 6D summarizes the ECSA as a function of number of cycles. As can be seen the ECSA of all the catalyst decreases as a function of the number of shut-up/shut-down cycles. The commercial catalyst Pt/C degrades rapidly and no Pt ECSA was observed after 2000 cycles. The Pt/VC and Pt/TaC catalyst decreased their surface area from 53 $m^2\ g^{-1}$ to 11 $m^2\ g^{-1}$ and from 48 $m^2\ g^{-1}$ to 11 $m^2\ g^{-1}$ respectively after 5000 cycles. The Pt/NbC showed the slowest and smallest decay of the ECSA. After 2000 cycles, the Pt/NbC shows over 40% more ECSA than the other two Pt/TMC, and after 5000 cycles, the ECSA was 18 $m^2\ g^{-1}$.

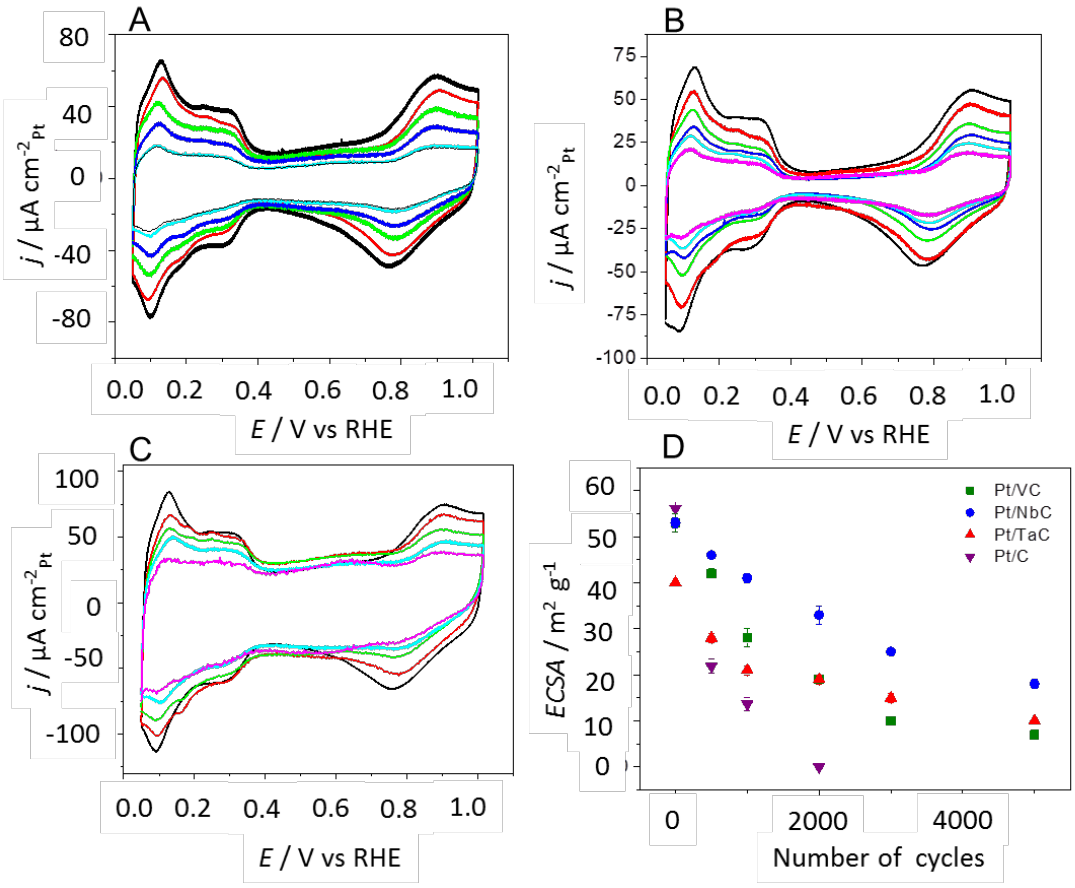

Figure 6 (A-C) Voltammetric profiles of Pt/VC, Pt/NbC, Pt/TaC and Pt/C in 0.1 M $HClO_4$ 50 mV s^{-1} at 0 cycles (black line), 500 cycles (red line), 1000 cycles (green line), 2000 cycles (cyan line) and 5000 cycles (purple line). The cyclic voltammograms of Pt/C are not shown because they were published in a previous communication. (D) ECSA of P/VC, Pt/NbC, Pt/TaC and Pt/C as a function of number of cycles.

In order to understand the degradation mechanism of the Pt/TMC catalysts, the Pt content of the catalyst layer was determined by XRF measurements during the protocol and the degradation models described in reference 21 were implemented.[21] (See appendix II for more information) The ECSA and the platinum content has been normalized in figure 7 by the initial values for proper comparison. Figure SI8 shows X-ray fluorescence spectra of Pt/VC, Pt/NbC, Pt/TaC and Pt/C at different stages of the shut-up/shut-down protocol, showing Pt(Lα). For the Pt/VC (Figure 7A), the decrease of the ECSA and Pt content follows the same trend during the ASP which can

be related to dissociative mechanisms as Pt dissolution or particle detachment are the responsible of the deterioration of the catalyst. The Pt/NbC shows similar behaviour within the first 2000 cycles, after when the Pt decay is larger than the decay of the ECSA meaning that the degradation is dominated by dissociative processes. On the other hand, Pt/TaC shows a decrease of ECSA larger than the Pt content in the first 1000 cycles, therefore associative mechanisms such Ostwald ripening or agglomeration are the major responsible of the degradation of this catalyst in this time window. However, the decrease of the ECSA and Pt content are similar after 1000 cycles which is attributed to a change to dissociative degradation mechanism.

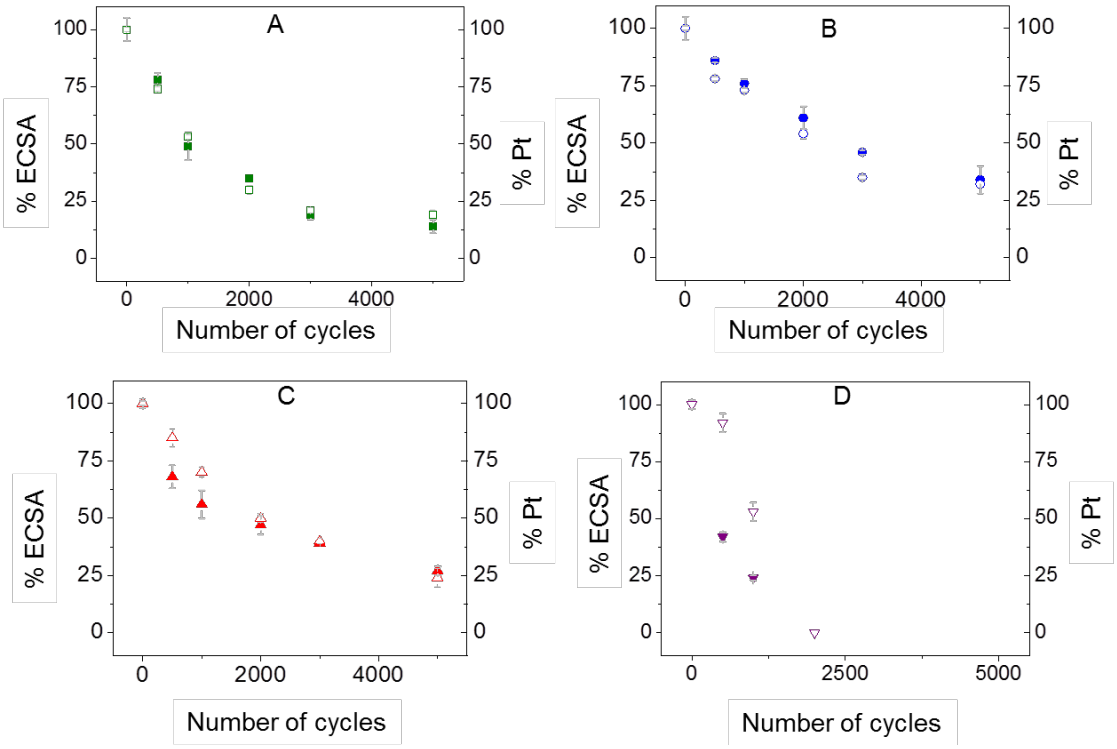

Figure 7 Relationship between the ECSA and Pt content from XRF measurements as a function of the number of cycles during the shut-up/shut-down protocol for Pt/VC (A), Pt/NbC (B), Pt/TaC (C) and Pt/C (D). Solid symbol for ECSA and empty symbol for Pt content.

In addition to the degradation of the Pt nanoparticles, it is important to consider the degradation of the support. Previous works have shown the degradation of the carbon support by following the CO_2 formation.[32] Here, the degradation of the support was followed by measuring the content of the metal on the TMC by XRF. Figure SI10 shows the normalized remaining loading of VC, NbC and TaC upon degradation cycles estimated by comparing of the initial intensity of the signals and the intensity after the degradation cycles. (See appendix II for more information). As can be seen in the figure SI9, the degradation of the TMC in the first 1000 cycles is much larger than in the rest of the protocol. NbC was the TMC most stable after the degradation protocol as it shows 90 % of the initial intensity whilst TaC showed a 80 % and VC a 75 %.

The ORR activity of the catalysts was measured during the protocol. Figure 8 shows the Tafel plots of the catalysts at different stages of the protocol. It can be seen that the Tafel curves shift to lower mass activity values as a function of number of cycles.

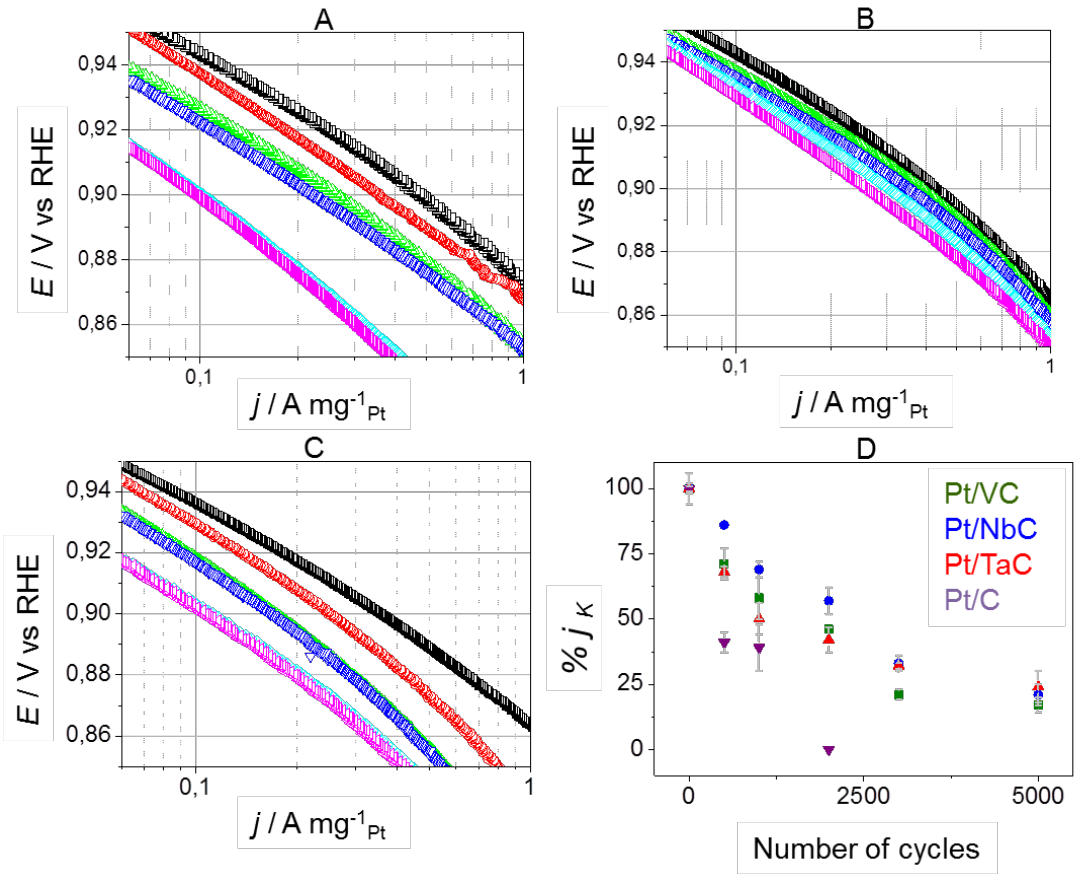

Figure 8 Mass activity, j_k, for the ORR on the TMC as a function of the number of shut-up/shut-down cycles. The data shown correspond to the positive-going sweep at 20 mVs^{-1} in O_2-saturated 0.1 M $HClO_4$ at 1600 rpm Pt/VC (A), Pt/NbC (B), Pt/TaC (C). (D) Kinetic current density (j_k, A mg^{-1}) at 0.9 V vs. RHE, as a function of cycle number.

Figure 8D summarizes the normalized mass activity as a function of number of cycles. In the first 3000 cycles, the decay of the mass activity is linear for Pt/VC, PT/NbC and Pt/TaC and in the successive cycles the mass activity remains almost constant. In absolute values, the mass activity for Pt/VC, PT/NbC and Pt/TaC is 0.09 A mg^{-1}_{Pt}, 0.29 A mg^{-1}_{Pt} and 0.1 A mg^{-1}_{Pt} respectively. It can be seen therefore, that the ORR mass activity obtained

with the Pt/NbC catalyst at the end of the protocol is comparable to the amass activity of Pt/C at the beginning of the protocol.

4. Conclusions

In this work, we have presented the synthesis of high surface are VC,NbC and TaC that were later used as a support of platinum nanoparticles catalyst for ORR. The supported catalyst was characterized in terms of structure and reactivity. All the TMC prepared show surfaces areas larger than 50 $m^2\ g^{-1}$ which is the minimum required for support materials in PEFC gas diffusion electrodes. The TCM also shown contact angles with water higher of about 140 which is comparable with the 135° contact angle reported for the carbon Vulcan.

The Pt/VC, Pt/NbC and Pt/TaC showed a 1.9, 1.7 and 1.4-fold ORR activity improvement respect to Pt/C catalyst, respectively under thin-film configuration conditions in a RDE.

Additionally, the stability of the catalysts was evaluated carrying under shut-up/shut-down accelerated stress protocol conditions. Dissociative mechanisms as Pt dissolution and particle detachment were the major responsible of Pt/VC and Pt/NbC degradation, whilst associative mechanisms as agglomeration or Ostwald ripening control the degradation of the Pt/TaC in the first 2000 cycles. The Pt/NbC showed the smaller degradation and the highest activity during the whole ASP. At the end of life, the mass activity towards the ORR was 0.29 A mg^{-1}_{Pt}. which is larger than the mass catalytic activity at the beginning of life for the commercial Pt/C_{vulcan}.

Transition metal carbides are potential support materials for PEFC application because it has been proved that they are stable under oxidative conditions. Our results demonstrates that TMC and in particular NbC is a promising alternative to commercial Vulcan XC-72 as a support materials for the cathode in PEMFC.

5. Conflicts of interest

There are no conflicts to declare.

6. Acknowledgements

J. M. acknowledges the University of Birmingham for financial support through PhD scholarships at the School of Chemistry. P. R. acknowledges the University of Birmingham for financial support through the Birmingham fellowship program.

7. References

1 J. Larminie, A. Dicks and M. McDonald, *Fuel cell systems explained*, Wiley., 2003.

2 C. Song, *Catal. Today*, 2002, **77**, 17–49.

3 X.-Z. Yuan, H. Li, S. Zhang, J. Martin and H. Wang, *J. Power Sources*, 2011, **196**, 9107–9116.

4 R. Borup, J. Meyers, B. Pivovar, Y. S. Kim, R. Mukundan, N. Garland, D. Myers, M. Wilson, F. Garzon, D. Wood, P. Zelenay, K. More, K. Stroh, T. Zawodzinski, J. Boncella, J. E. McGrath, M. Inaba, K. Miyatake, M. Hori, K. Ota, Z. Ogumi, S. Miyata, A. Nishikata, Z. Siroma, Y. Uchimoto, K. Yasuda, K.-I. Kimijima and N. Iwashita, *Chem. Rev.*, 2007, **107**, 3904–51.

5 X. Li and I.-M. Hsing, *Electrochim. Acta*, 2006, **51**, 5250–5258.

6 H. Schulenburg, B. Schwanitz, N. Linse, G. Scherer, A. Wokaun and F. Polytechnique, *J. Phys. Chem. C*, 2011, **115**, 14236–14243.

7 C. a. Reiser, L. Bregoli, T. W. Patterson, J. S. Yi, J. D. Yang, M. L. Perry and T. D. Jarvi, *Electrochem. Solid-State Lett.*, 2005, **8**, A273.

8 E. Zakrisson, *The Effect of Start / Stop Strategy on PEM Fuel Cell Degradation Characteristics*, 2011.

9 S. D. Knights, K. M. Colbow, J. St-Pierre and D. P. Wilkinson, *J. Power Sources*, 2004, **127**, 127–134.

10 U. A. Paulus, A. Wokaun, G. G. Scherer, P. S. Institut and C.-V. Psi, *J. Phys. Chem.*, 2002, **106**, 4181–4191.

11 T. Toda, H. Igarashi and M. Watanabe, *J. Electrochem. Soc.*, 1998, **145**, 4185–4188.

12 J. Greeley, I. E. L. Stephens, a S. Bondarenko, T. P. Johansson, H. a Hansen, T. F. Jaramillo, J. Rossmeisl, I. Chorkendorff and J. K. Nørskov, *Nat. Chem.*, 2009, **1**, 552–556.

13 T.-T. Nguyen, V. T. T. Ho, C.-J. Pan, J.-Y. Liu, H.-L. Chou, J. Rick, W.-N. Su and B.-J. Hwang, *Appl. Catal. B Environ.*, 2014, **154**–**155**, 183–189.

14 Y. Liu, T. G. Kelly, J. G. Chen and W. E. Mustain, *ACS Catal.*, 2013, **3**,

1184–1194.

15 I. J. Hsu, D. a. Hansgen, B. E. McCandless, B. G. Willis and J. G. Chen, *J. Phys. Chem. C*, 2011, **115**, 3709–3715.

16 Y. C. Kimmel, X. Xu, W. Yu, X. Yang and J. G. Chen, *ACS Catal.*, 2014, **4**, 1558–1562.

17 A. Ishihara, Y. Ohgi, K. Matsuzawa, S. Mitsushima and K. Ota, *Electrochim. Acta*, 2010, **55**, 8005–8012.

18 Y. Jiang, J. Hao, M. Hou, H. Zhang, X. Li, Z. Shao and B. Yi, *RSC Adv.*, 2015, **5**, 104095–104100.

19 M. Sansotera, W. Navarrini, L. Magagnin, C. L. Bianchi, A. Sanguineti, P. Metrangolo and G. Resnati, *J. Mater. Chem.*, 2010, **20**, 8607.

20 P. Justin, P. H. K. Charan and G. R. Rao, *Appl. Catal. B Environ.*, 2014, **144**, 767–774.

21 J. Monzó, D. F. van der Vliet, A. Yanson and P. Rodriguez, *Phys. Chem. Chem. Phys.*, 2016, **18**, 22407–22415.

22 C. Giordano, C. Erpen, W. Yao and M. Antonietti, *Nano Lett.*, 2008, **8**, 4659–63.

23 F. Hasché, M. Oezaslan and P. Strasser, *J. Electrochem. Soc.*, 2012, **159**, B24–B33.

24 C. Giordano and M. Antonietti, *Nano Today*, 2011, **6**, 366–380.

25 J. Solla-Gullón, E. Gómez, E. Vallés, A. Aldaz and J. M. Feliu, *J. Nanoparticle Res.*, 2010, **12**, 1149–1159.

26 J. Solla-Gullón, V. Montiel, A. Aldaz and J. Clavilier, *J. Electrochem. Soc.*, 2003, **150**, E104–E109.

27 K. J. J. Mayrhofer, D. Strmcnik, B. B. Blizanac, V. Stamenkovic, M. Arenz and N. M. Markovic, *Electrochim. Acta*, 2008, **53**, 3181–3188.

28 S. Kocha, *DOE Annu. Prog. Rep.*, 2014, 215–218.

29 A. Ohma, K. Fushinobu and K. Okazaki, *Electrochim. Acta*, 2010, **55**, 8829–8838.

30 C. Jackson, G. T. Smith, M. Markiewicz, D. W. Inwood, A. S. Leach, P. S.

Whalley, A. R. Kucernak, A. E. Russell, D. Kramer and P. B. J. Levecque, *J. Electroanal. Chem.*, 2018, **819**, 163–170.

31 T. Binninger, T. J. Schmidt and D. Kramer, *Phys. Rev. B*, 2017, **96**, 165405.

32 V. A. T. Dam, K. Jayasayee and F. A. de Bruijn, *Fuel Cells*, 2009, **9**, 453–462.

Transition metal carbides as alternative support materials for cathode catalyst in Polymer Electrolyte Membrane Fuel Cell

Javier Monzó[a], Ashleigh Danks[a], Jonas Pampel[b], Jose Solla-Gullon [c],Tim-P. Fellinger[d], Zoe Schnepp[a] and Paramaconi Rodriguez*, [a].

[a]School of Chemistry, University of Birmingham, Edgbaston, B15 2TT, Birmingham, England.

[b]Max Planck Institute of Colloids and Interfaces, Department of Colloid Chemistry, Potsdam, Germany.

[c]Institute of Electrochemistry, University of Alicante 03080, Alicante (Spain).

[d]Chalmers University of Technology, Department of Chemistry and Chemical Engineering, Göteborg, Sweden.

Corresponding author: p.b.rodriguez@bham.ac.uk

Table of contents

Section 1. Particle size distribution of transition metal carbides.

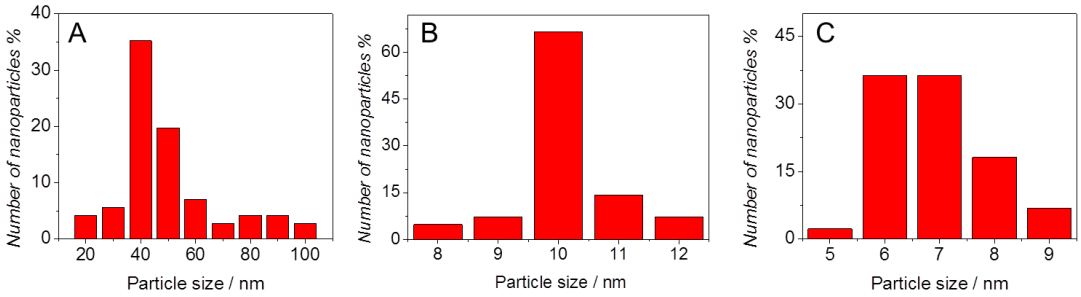

Figure SI1. Particle size distribution of VC (A), NbC (B) and TaC (C) obtained from TEM measurements. The relative abundance of each particle size was calculated from a total of 180 nanoparticles.

Section 2. Nitrogen adsorption isotherms of the transition metal carbides.

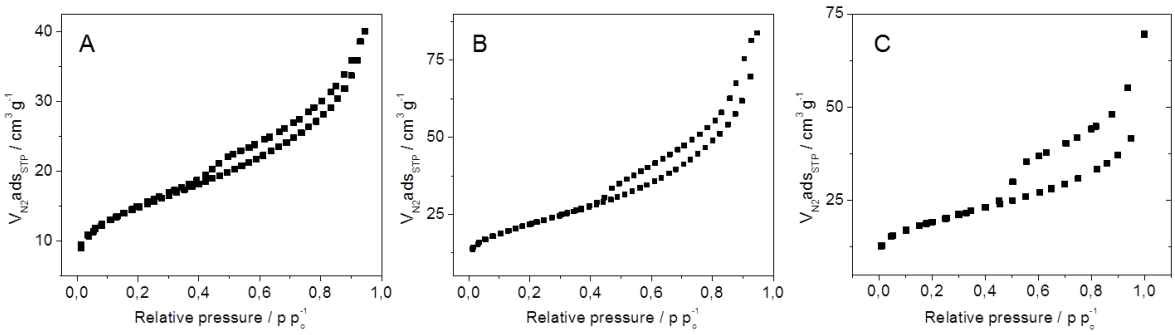

Figure SI2. Nitrogen adsorption isotherms of VC (A), NbC(B) and TaC(C).

Section 3. Physical characterization of Pt/C commercial catalyst.

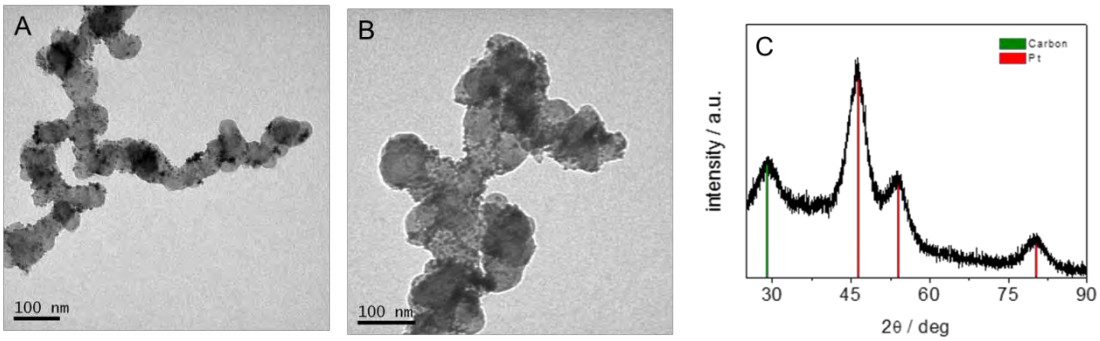

Figure SI3. (A-B) TEM images in which black dots are the Pt nanoparticles dispersed on carbon. (C) Commonly XRD pattern of Pt/C which is in agreement with previous results reported in the literature for this commercial catalyst.

Section 4. X-ray diffraction characterization of Pt nanoparticles.

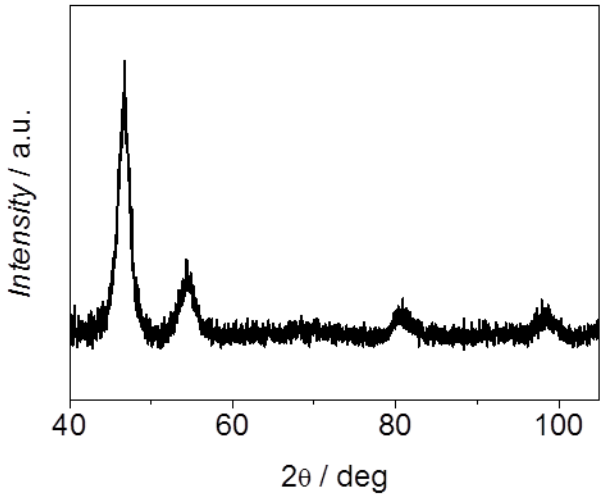

Figure SI4. X-ray diffraction pattern of Pt nanoparticles which presents the characteristic signals for Pt at 2Θ = 46.82° (111), 54.40° (200) and 80.79° (220).

Section 5. X–ray diffraction characterization of Pt/VC, Pt/NbC and Pt/TaC.

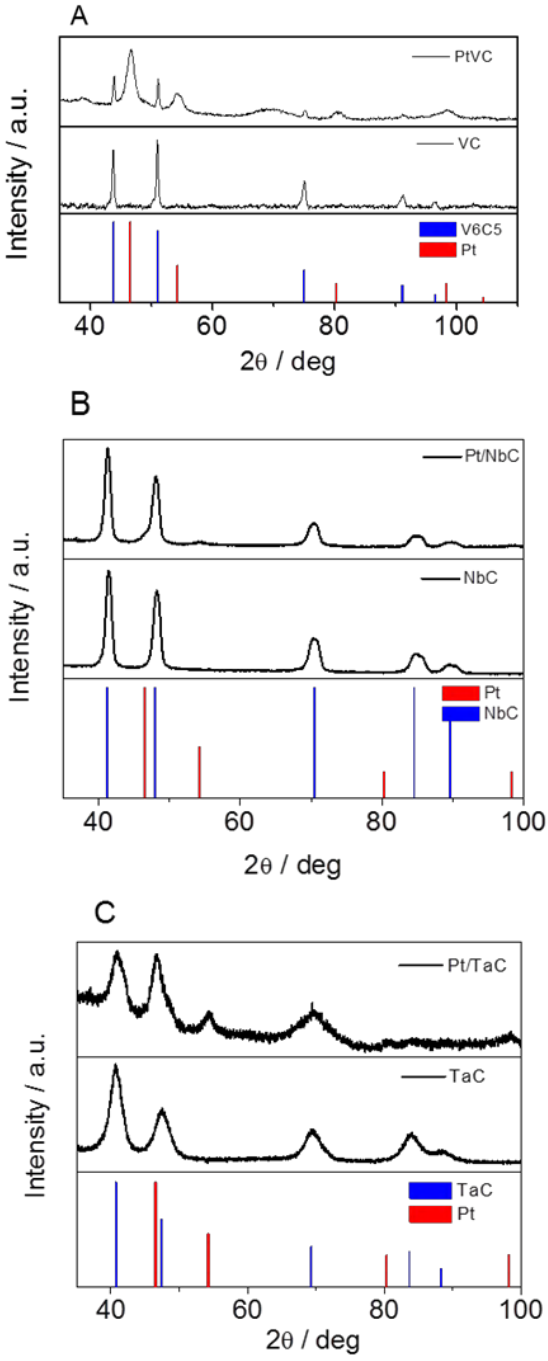

Figure SI5. XRD patterns of Pt nanoparticles dispersed on TMC. Pt/VC (A), Pt/NbC (B) and Pt/TaC (C), In the lower part of each panel the database pattern for Pt and TMC have been included in order to make more visual the analysis of the patterns.

Section 6. X-ray fluorescence spectra of Pt/VC, Pt/NbC and Pt/TaC.

Figure SI6 shows the X-ray fluorescence spectra of Pt/VC, Pt/NbC and Pt/TaC, the characterization was performed by triplicate in an aleatory order to prevent systematically errors. The emission line considered for the analysis was the more intense in order to prevent interferences from the background; Pt (Lα), V (Lα) Nb (Kα) and Ta(Lα).

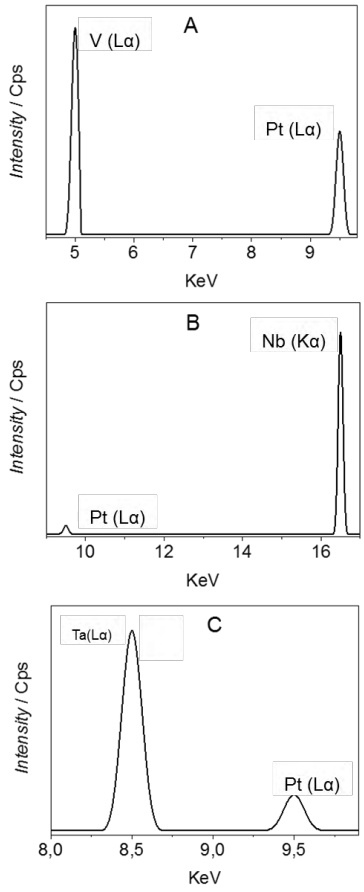

Figure SI6. X-ray fluorescence spectra of Pt nanoparticles supported on VC (A), NbC (B) and TaC(C).The signal at 9.45 keV is associated PtLα and the signals at 4.97 KeV, 16.51 and 8.51 KeV are associated to V (Lα) Nb (Kα) and Ta(Lα). In order to present clear results, the original data was digitalized using the GraphClick software. Original data is available upon request.

Section 7. Tafel plots of Pt/VC, Pt/NbC, Pt/TaC and Pt/C.

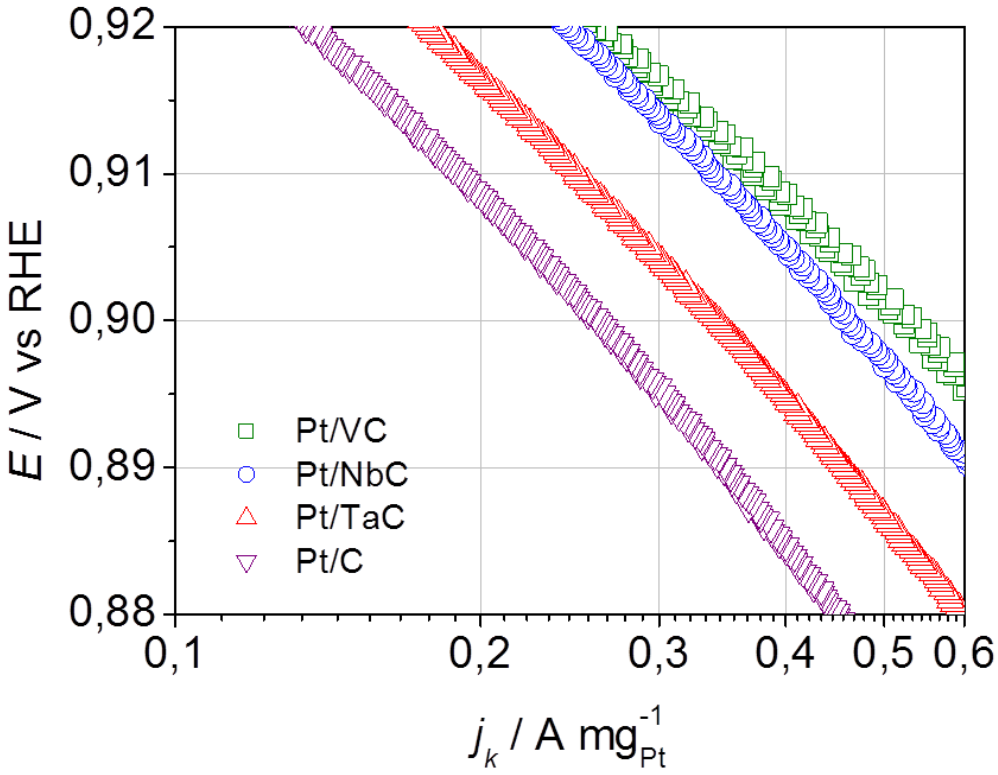

Figure SI7. Mass activity, j_k, for the ORR on the TMC as indicated in the figure. The data shown correspond to the positive-going sweep at 20 mVs^{-1} in O_2-saturated 0.1 M $HClO_4$ at 1600 rpm.

Section 8. X-ray fluorescence spectra of Pt/VC, Pt/NbC, Pt/TaC and Pt/C at different stages of the shut-up/shut-down protocol, showing Pt(L_α).

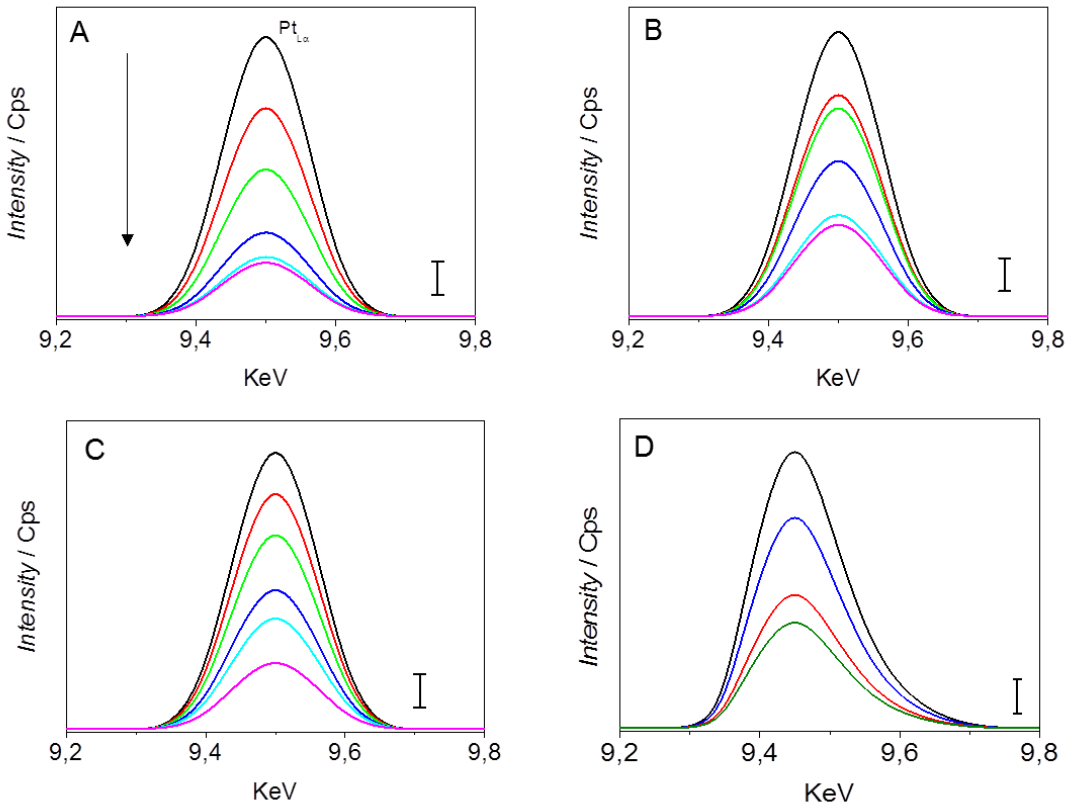

Figure SI8. XRF spectra of Pt/VC (A), Pt/NbC (B), Pt/TaC and Pt/C (D) during the shut-up/shut-down protocol (scale bar = 100 Cps). The XRF spectra were acquire at 0 cycles (black), 500 cycles (red), 1000 cycles (green), 2000 cycles (blue), 3000 cycles (cyan) and 5000 cycles (purple). *GraphClick* software was used to digitalize the original data in order to present clear results.

Section 9. Remaining loading of TMC at different stages of the shut-up/shut-down protocol.

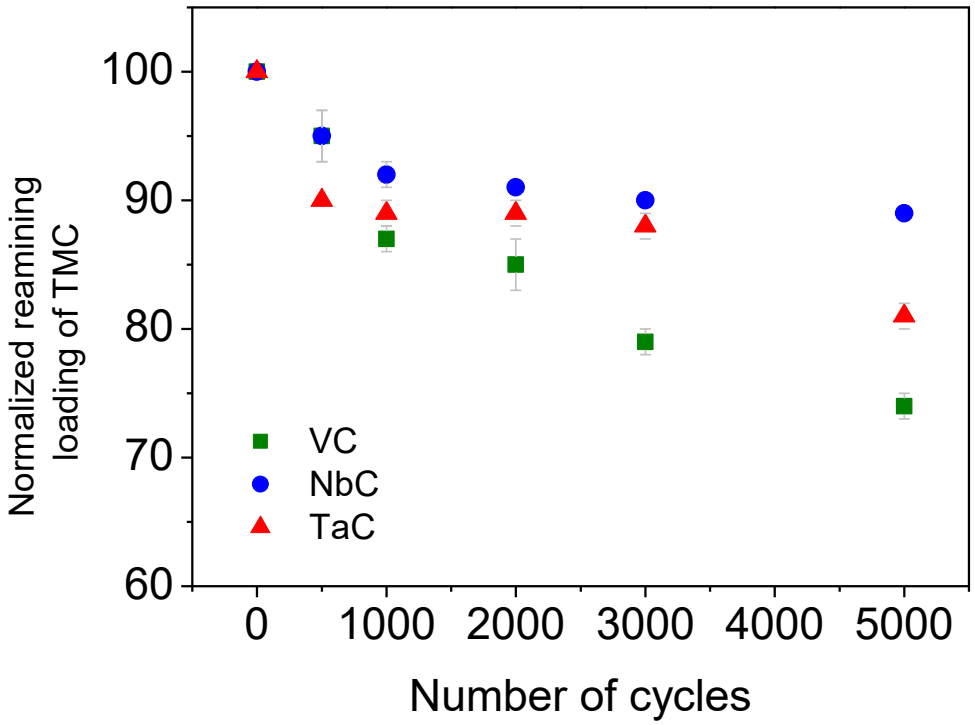

Figure SI9. Normalized remaining loading of TMC as a function of number of cycles. The loading was estimated by comparing of initial intensity of XRF signal and intensity at different stages of the degradation protocol.

CHAPTER 5

PtCo/NbC and Pt/NbC catalyst for oxygen reduction reaction: synthesis, characterization, activity and durability

Format: Paper (unpublished).

Information: J. Monzó and P. Rodriguez.

Overview: In this paper, we present the synthesis of Pt and PtCo nanoparticles supported on NbC. Pt/NbC and PtCo were characterized and tested as potential catalysts for PEFC application. Considering the results of Chapter 4, NbC was postulated as a potential support material because it was stable under oxidative conditions and promotes the ORR mass activity of Pt nanoparticles. For these reasons, it has been used as support material of PtCo to evaluate a possible electronic effect on the PtCo nanoparticles that could promote the ORR as well as to assess the stability of PtCo/NbC.

PtCo/NbC presented an improvement of the durability respect to the Pt/C and thus PtCo/NbC is postulated as a potential catalyst for PEFC because reduce the cost of the catalysts (10% wt. less Pt present in the alloy) and improve the durability with respect to the state-of-the-art catalyst.

Overview: JM and PR designed the experiments and JM carried out all the experiments. JM analysed the data and wrote the paper.

PtCo/NbC and Pt/NbC catalyst for oxygen reduction reaction: synthesis, characterization, activity and durability

Javier Monzó[a] and Paramaconi Rodriguez[*,a].

[a]School of Chemistry, University of Birmingham, Edgbaston, B15 2TT, Birmingham, England.

Corresponding author: p.b.rodriguez@bham.ac.uk

Abstract

In this work, we have reported the synthesis and characterization of Pt/NbC and PtCo/NbC catalysts. These novel cataysts showed an enhancement of the mass activity of 1.6-fold with respect to the commercial catalysts Pt/C. Addinionally, the stabiliy of the catalyts was studied, it was carried out an accelerated stress protocol (ASP), shut-up/shut-down protocol (0.5 V to 1.5 V vs RHE), and PtCo/NbC was the most stable. Meanwhile, Pt/C was completely degrade after 2000 cycles of the protocol the PtCo/NbC and Pt/NbC presented a stability of 45 % and 35 %, respectively. Also, the degradation mechanisms behind the deterioration of the catalysts were studied following a previous published methodology, dissociative mechanisms as Pt dissolution or particle detachment were the major responsible of PtCo/NbC and Pt/NbC deterioration. Finally, the ORR mass activity was reported as a function of the number of cycles, PtCo/NbC presented the highest mass activity after the whole protocol, 0.20 A mg^{-1}Pt.

1. Introduction

Fuel cell technology is an emerging approach for the generation of green energy to reduce the effect of energy production on the global warming.[1] Especially, PEFC is a promising candidate for automotive and stationary applications due to its high efficiency, low working temperature and zero

emissions.[2] However, the lifetime of PEFC is a limiting factor for a mass-commercialization as well as the cost.[3]

Currently, Pt and Pt-alloys are the state-of-the-art ORR catalysts for PEFC applications.[4–6] they present a high activity towards ORR and an acceptable durability. In order to reach a wide commercialization of PEFC, the amount of platinum has to be reduced due to the high cost of platinum. The use of transition metals to form alloys with Pt has been a common approach for this purpose.[4,7–11] Besides, Pt-alloys with transition metals have shown an improvement in mass activity and stability.[8,7,12,13] For example, the ORR mass activity of Pt increased when Pt alloys with cobalt forming Pt_3Co.[11]

In addition to reduce the amount of Pt, the development of stable support materials is crucial to increase the cost-efficiency of PEFC. Due to the operation conditions of PEFC, the catalyst suffers a deterioration leading in a failure of the device.[14] Recently, it was reported that the elucidation of the degradation mechanisms behind the deterioration is important to understand the degradation, thus design catalysts which present better stability.[15]

The ORR mass activity of Pt increased when metal oxides[16,17], doped-carbon[18] or metal nitrides[19] were used as support materials. The reason behind this improvement is the strong-metal-support-interaction (SMSI) phenomenon in which the support donates electronic charge to the metal (Pt). Thus, the adsorption of intermediate species of ORR (-OH and –OOH) onto the catalyst surface is mitigated leading more accessible active sites.[20]

Recently, transition metal carbides (TMC) have been used as support materials due to their electronic properties, physical stability and chemical resistance.[21] Pt nanoparticles (Pt-Nps) supported on WC showed an increase of the catalytic activity towards the ORR[22] and Pt nanodendrites supported on TiC showed an improvement of the activity as well.[16]

In this work, we present the stability study of Pt and PtCo nanoparticles supported on NbC. PtCo-Nps were selected due to their high mass activity and lower amount of Pt than pure Pt-Nps. NbC was selected as support material due to the expected chemical stability and the predicted SMSI. Also, the election of NbC was based on previous results of our group that showed and enhancement of ORR mass activity and stability when Pt-Nps were dispersed on TaC. In order to have a comparison with the market, the common and widely used Pt/Vulcan catalyst was used as reference.

2. Experimental section

2.1. Synthesis of Pt and PtCo nanoparticles

Pt and PtCo nanoparticles were synthesized following the methodology reported by Solla-Gullón et al.[7] In the case of Pt-Nps, H_2PtCl_6 was reduced with sodium borohydride using water in oil (w/o) microemulsion. In the case of PtCo nanoparticles, H_2PtCl_6 and $CoCl_2$ (atomic ratio, 3:1) were reduced in the water phase using sodium borohydride. In both cases, after the complete reduction of Pt and Co, the nanoparticles were precipitated adding acetone. Then, the nanoparticles were collected by centrifuge and cleaned with a solution of acetone:water in order to remove the organic

reagents. Finally, the nanoparticles were washed several times and stored with fresh Elga ultrapure water.

2.2. Preparation of catalyst inks

The catalysts inks were prepared dispersing 0.04 g of NbC in water, and then 0.01 g of Pt-Nps or PtCo-Nps was added. The resulting solution was stirred overnight and the catalyst Pt/NbC or PtCo/NbC was collected by centrifuge and cleaned several times with ElgaPureUltra water. 0.01 g of 20 wt. %Pt Pt/NbC was dispersed in 7 mL of ElgaPureUltra water in order to obtain a catalyst concentration of 0.0014 g mL^{-1}.

The ink of Pt/Vulcan (20 wt. %Pt, ETEK) was prepared dispersing 0.007 g of Pt/Vulcan in 20 mL of ElgaPureUltra water obtaining a concentration of $7 \cdot 10^{-5}$ g_{Pt} mL^{-1}.

2.3. Synthesis of Niobium Carbide

Niobium carbide was synthesis using the protocol developed by Giordano *et al.* in which a niobium salt ($NbNO_3$) was dissolved in ethanol obtaining a 10 wt. % of the metal salt. Then, a certain amount of the carbon source (Urea) was dissolved into 10 ml of the metal salt solution. The ethanol was evaporated in an air oven at 80 ºC obtaining a glassy product of yellowish colour. This glassy product was calcinated in a tubular furnace at 900 °C during 2 hours under nitrogen atmosphere.

2.4. Physical characterization

TEM images of the catalysts were acquired using a JEOL JEM 1200 EX MKI instrument. The samples were prepared by drop-casting deposition of each catalyst on carbon-coated copper grids.

The crystalline structure was studied using a Bruker AXS D2 PHASER diffractometer with a Co-Kα (0.179 nm) radiation source. On a zero background SiO holder (MTI) few drops of catalysts were deposited and dried under Ar atmosphere.

X-ray fluorescence technique was employed to determine the composition of PtCo-Nps, Pt/NbC and PtCo using a Bruker S8 Tiger 4 kW spectrometer.

The surface area of NbC was calculated from the experimental results of the N_2 adsorption experiments performed at 77 K in a N_2 atmosphere after degassing the samples at 120 °C under vacuum for 12 hours using Quantachrome Quadrasorb equipment.

2.5. Electrochemical measurements

An electrochemical cell of two compartments with the reference electrode located in a lugging was employed for the electrochemical measurements. Autolab PGSTAT12 potentiostat was used to control the potential and record the current. A gold wire was used as counter electrode and the reference electrode was a Ag/AgCl electrode (the potentials reported in this work have been corrected to RHE). The electrochemical measurements were carried out in a electrolyte solution of 0.1 M $HClO_4$ (Suprapure, Merck), prepared with ultra-pure water (ElgaPureUltra, 18.2 Ohm cm^{-1}, 1 ppb total organic carbon).

In order to study the stability of the catalysts, an ASP described by the Department of Energy of United States[11] was carried out in which the catalysts were cycled between 0.5 V to 1.5 V vs RHE at 50 mV s^{-1}. ECSA and Pt content were measured at some stages of the protocol as it was described in a previous publication.[15] In order to have fair comparison between catalysts, the loading used for all the catalysts is 150 μg_{Pt} cm^{-2}.

3. Results and discussion

3.1. Catalyst characterization

Figure 1A shows the XRD pattern of Pt, the 2θ signals at 46.80° (111) and 54.40° (200) confirm the presence of Pt nanoparticles.[8] The formation of PtCo nanoparticles is confirmed by the shift of the reflections to higher 2θ values (Fig. 1B), the signals 2θ= 47.05° (111) and 54.67° (200) correspond

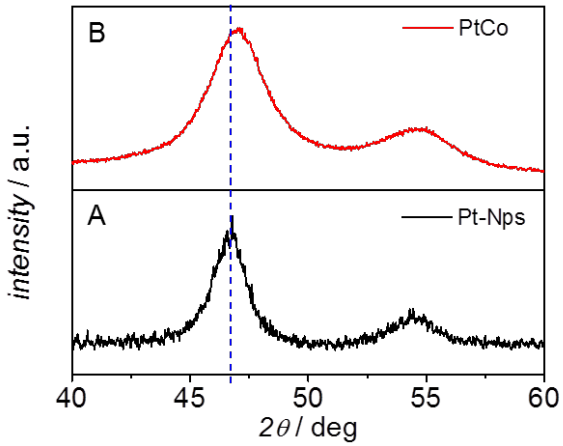

Figure 1 X-ray diffraction patterns of Pt nanoparticles (A) and PtCo nanoparticles (B).

to PtCo.[7]

The atomic composition of the PtCo nanoparticles acquired by EDX is 80 %Pt and 20% Co (Fig. SI1). Figure 2 shows the TEM images of Pt-Nps and

PtCo which present a particle size distribution of 5 nm and 4 nm, respectively (Fig. 2 C-D).

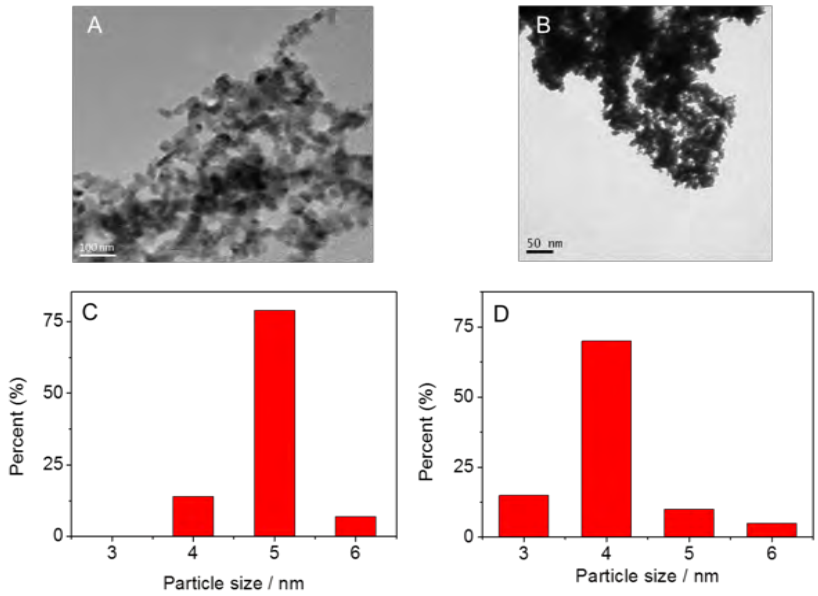

Figure 2 TEM images and particle size distribution of Pt-Nps (A-C) and PtCo-Nps (B-D). The particle size distribution was calculated in base of the size of 200 nanoparticles.

The Pt and PtCo were dispersed on NbC, figure 3 shows the TEM image of Pt and PtCo nanoparticles surrounding nanoparticles of NbC. The presence of Pt, PtCo and NbC was confirmed by XRD, the figure SI2 shows the XRD pattern of Pt/NbC and PtCo/NbC. The composition of the novel prepared catalysts was acquired by X-ray fluorescence (XRF) confirming a composition of 19 % Pt and 81 % NbCo for Pt/NbC catalysts, and a composition of 20 % Pt, 1 % Co and 79 % NbCo (Figure SI3). The NbC characterisation is summarized in the section 4 of the supporting information, it has to be highlighted that NbC present a surface area of 76 m^2 g^{-1}.

The Pt/C catalyst (20% wt. Pt) was employed as a reference to compare the

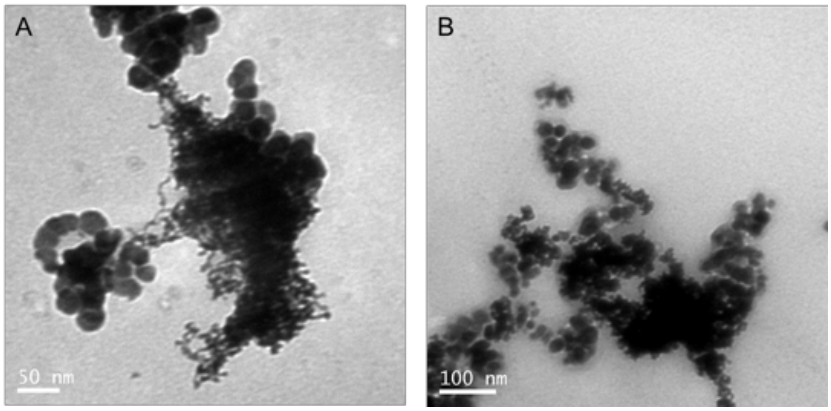

Figure 3 TEM images of Pt/NbC (A) and PtCo/NbC (B).

activity and durability of the novel catalysts presented in this work. The characterization results are in the section 5 of the supporting information. It is composed of Pt nanoparticles with a size of 5 nm supported on carbon. The percentage composition is 20 % in weight of Pt and presents a BET surface area of 250 m^2 g^{-1}.

3.2. Electrochemical characterization

Figure 4A shows the cyclic voltammograms of Pt/NbC, PtCo/NbC and Pt/C in 0.1 M $HClO_4$. The three catalysts present the common profile for Pt in acidic media in which H_{upd} region (0.05 V to 0.4V vs RHE), the double layer region (0.4 V to 0.7 V vs RHE) and the PtO_x region (0.7 V to 1.1 V vs RHE) can be distinguished. In the case of PtCo/NbC, it shows a smaller H_{upd} region than Pt/NbC due to the amount of Pt is smaller due to its alloy with

Co. Also, the presence of Co at the surface of Pt can block active sites for H^+ adsorption/desorption.

Also, both catalysts show the same charge in the double layer. However,

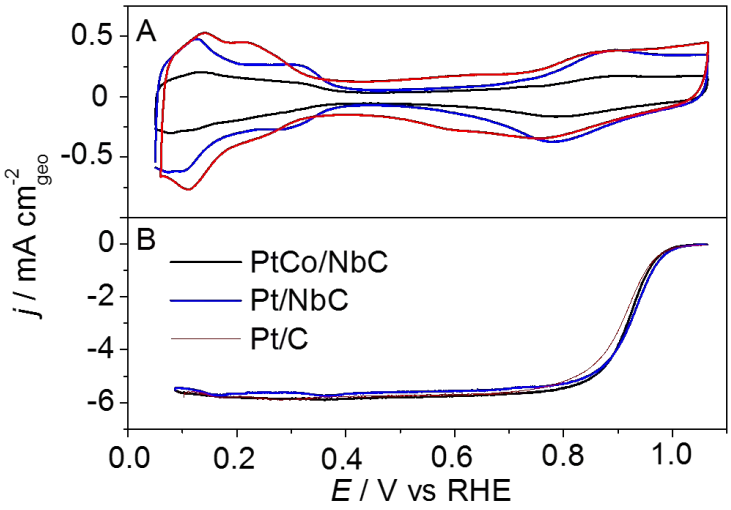

Figure 4 Voltammetric profiles of PtCo/NbC (black line), Pt/NbC (blue line) and Pt/C (red line) in Ar atmosphere (A) and in presence of O2 (B). 0.1 M HClO4 at 20 mV s-1. Rotation rate: ω = 1600 rpm.

Pt/C present a larger double layer charge due to the surface area of carbon is much larger than the surface area of NbC. For carbon the surface area is 250 $m^2\ g^{-1}$ and for NbC is 76 $m^2\ g^{-1}$. The electrochemical surface area (ECSA) was calculated using the charge associated with the process of H^+ adsorption/desorption and using the value of 210 μC cm^{-2} corresponding for the formation of a hydrogen monolayer. The ECSA values are (53 ± 1) $m^2\ g^{-1}$ for Pt/NbC, (24 ± 1) $m^2\ g^{-1}$ for PtCo/NbC and (57 ± 1) $m^2\ g^{-1}$ for Pt/C. These values are in agreement with previously reported results for Pt nanoparticles of 5 nm.

Figure 4B shows the voltammetric profiles of the catalyst in 0.1 M $HClO_4$ satured with O_2. The curves have been corrected by the Ohmic drop and the background associated with capacitive current has been subtracted. The intrinsic activity for each catalyst was calculated at 0.9 V vs RHE using the Koutecky-Levich equation. Pt/NbC and PtCo/NbC present a mass activity of 0.40 A mg^{-1}_{Pt} and 0.42 A mg^{-1}_{Pt}, respectively. These values are 1.6 bigger than the Pt/C mass activity (0.25 A mg^{-1}_{Pt}). These differences are easier to see at the Taffle plots (Figure SI6). The enhancement of the mass activity of Pt could be associated with a strong-metal-support-interaction (SMSI). It has been reported that introducing metal carbides as support materials can promote an electron donation from metal carbide to Pt, thus oxygenated intermediates of ORR (-OH or –OOH) are less stable promoting the ORR. In the case of PtCo/NbC, this enhancement of mass activity could be associated as well to the presence of Co. Figure SI7 shows the ORR polarization curve for PtCo/NbC and for unsupported PtCo nanoparticles, it can be seen that the curves almost overlap meaning that the enhancement is related to the presence of Co.

3.3. Stability of PT/NbC and PtCo/NbC under oxidative conditions: shut-up/shut-down protocol

Figure 5A-C shows the blank voltammograms of the three catalysts at the start point of the shut-up/shut-down protocol, beginning of life (BOL), and at the end of the protocol, end of life (EOL). The characteristic regions linear dependent of Pt available sites as regions of H^+ adsorption/desorption and PtO_x decrease as a function of number of cycles due to the degradation of the catalyst. Figure 5D displays the ECSA as function of number of cycles, the commercial catalyst, Pt/C, after 2000 cycles is completely degrade.

However, the ECSA of Pt/NbC and PtCo/NbC goes from 53 to 18 m^2 g^{-1} and from 24 to 11 m^2 g^{-1} after the 5000 cycles, respectively. In the case of the PtCo/NbC, the degradation in the 1000 cycles is much faster that in the rest of the protocol. On the other hand, the degradation of Pt/NbC is linear in the first 3000 cycles, and then the trends change.

In order to understand the degradation mechanisms of the catalysts, the Pt

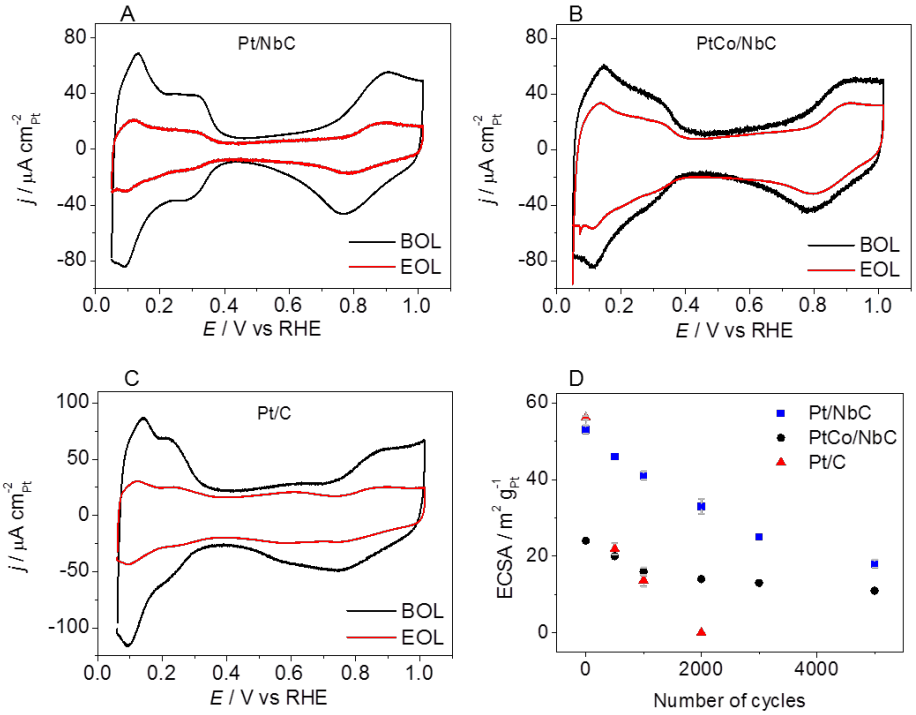

Figure 5 A-C Blank voltammograms of Pt/NbC, PtCo/NbC and Pt/C at the BOL (black line) and at the EOL (red line) in 0.5 M HClO4 at 50 mV s^{-1}. D ECSA as a function of number of cycles.

content of the catalyst layer was measure during the accelerated stress test (AST) following the methodology previously reported. Figure 6 shows the normalized ECSA and the Pt content as a function of the number of cycles. XRF spectra of the catalysts are summarized in figure SI6. For the PtCo/NbC, the decay of the ECSA and Pt content is proportional meaning that dissociative mechanisms as Pt dissolution or particle detachment are the responsible of the degradation. In the case of Pt/NbC, the decay of the Pt content is larger than the

decay of ECSA during the whole protocol, dissociative mechanism are the predominant mechanism of the degradation. The fact that the decay of Pt content is larger than the decay of the ECSA means that the dissolution/detachment of Pt is faster than in the degradation of PtCo/NbC. In contrast, the decay of ECSA is much larger than the decay of Pt content for Pt/C confirming that associative mechanisms as Ostwald ripening or agglomeration are the responsible of the degradation. Additionally, the degradation of carbon has to be considered in the degradation of Pt/C.

In addition to the degradation of the active-metal, it has to be considered

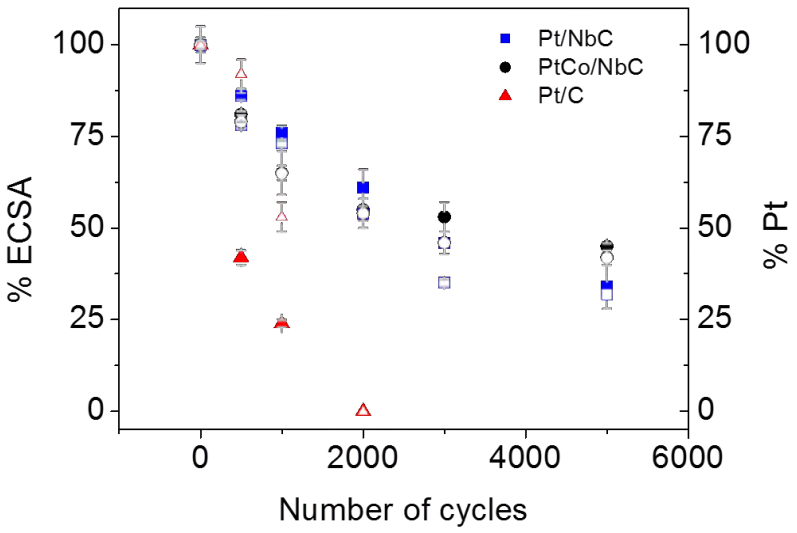

Figure 6 Normalized ECSA and normalized Pt content as a function of number of cycles for Pt/NbC (blue squares), PtCo/NbC (black spheres) and Pt/C (red triangles). Solid symbol for ECSA and empty symbol for Pt content.

the degradation of the support material. For that reason, the degradation of NbC has to be consider in the degradation of Pt/NbC and PtCo/NbC. Figure SI7 shows the XRF spectra in the region of Nb signal, the Nb content decay around 11 % for Pt/NbC and 10 % for PtCo/NbC. The degradation of the

novel catalysts presented in this work could be affected by the degradation of the NbC.

The ORR mass activity was measured during the protocol, figure 7 shows the ORR polarization curves and the normalized mass activity. In the first 2000 cycles, the mass activity of the Pt/NbC decays a 30 % whilst the activity of PtCo/NbC decays a 40 %. The commercial catalyst, Pt/C, is the one that suffers the strongest activity decay, in the first 1000 cycles decays a 60 % and after 2000 cycles is degrade and does not present activity.

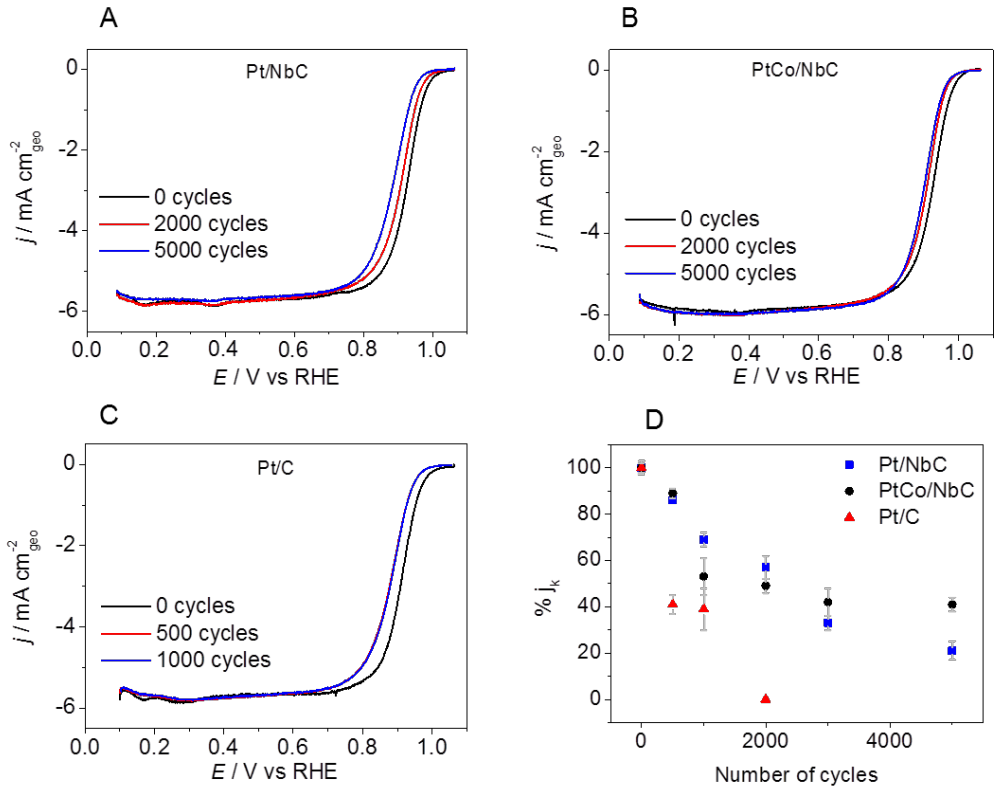

Figure 7 Figure 7 (A-C) ORR polarization curves and (D) normalized mass activity Pt/NbC (blue squares), PtCo/NbC (black spheres) and Pt/C (red triangles). 0.1 M $HClO_4$ at 20 mV s^{-1}. Rotation rate: ω = 1600 rpm.

4. Conclusions

In this paper, we have reported the synthesis and characterization of two novel catalysts as Pt/NbC and PtCo/NbC. The activity towards of the ORR was measured and Pt/NbC and PtCo/NbC presented an improvement respect Pt/C by 1.6 times. Additionally, the stability of the catalyst was studied under oxidative harsh conditions (Shut-up/shut-down protocol), and the PtCo/NbC and Pt/NbC were more stable than Pt/C. PtCo/NbC was more stable than the commercial catalysts that was degrade after 2000 cycles. Also, PtCo/NbC was a 10 % more stable than Pt/NbC after the whole protocol. In addition, the degradation mechanisms behind the deterioration of the catalysts were studied, dissociative mechanism were the major responsible of Pt/NbC and PtCo/NbC degradation.

In base of the results obtained in this work, NbC is postulated as a proper candidate to be a support material because is stable under oxidative conditions. Also, Pt/NbC and PtCo/NbC are proper catalysts to be used in PEFC as they are more stable than the commercial Pt/C.

5. Conflicts of interest

There are no conflicts to declare.

6. Acknowledgements

P. R. acknowledges the University of Birmingham for financial support through the Birmingham fellowship program. J. M. acknowledges the University of Birmingham for financial support through PhD scholarships at the School of Chemistry.

7. References

1 W. T. W. Lubitz, *Chem. Rev.*, 2007, **107**, 3900–3903.

2 S. Litster and G. McLean, *J. Power Sources*, 2004, **130**, 61–76.

3 R. L. Borup, J. R. Davey, F. H. Garzon, D. L. Wood and M. A. Inbody, *J. Power Sources*, 2006, **163**, 76–81.

4 U. A. Paulus, A. Wokaun, G. G. Scherer, P. S. Institut and C.-V. Psi, *J. Phys. Chem.*, 2002, **106**, 4181–4191.

5 S. Chen, H. A. Gasteiger, K. Hayakawa, T. Tada and Y. Shao-Horn, *J. Electrochem. Soc.*, 2010, **157**, A82.

6 H. a. Gasteiger, S. S. Kocha, B. Sompalli and F. T. Wagner, *Appl. Catal. B Environ.*, 2005, **56**, 9–35.

7 J. Solla-Gullón, E. Gómez, E. Vallés, A. Aldaz and J. M. Feliu, *J. Nanoparticle Res.*, 2010, **12**, 1149–1159.

8 S. Lankiang, M. Chiwata, S. Baranton, H. Uchida and C. Coutanceau, *Electrochim. Acta*, , DOI:10.1016/j.electacta.2015.09.061.

9 H. Yang, W. Vogel and C. Lamy, *J. Phys. Chem. B*, 2004, **108**, 11024–11034.

10 Q. Huang, H. Yang, Y. Tang, T. Lu and D. L. Akins, *Electrochem. commun.*, 2006, **8**, 1220–1224.

11 F. Hasché, M. Oezaslan and P. Strasser, *ChemCatChem*, 2011, n/a-n/a.

12 T. P. Johansson, E. T. Ulrikkeholm, P. Hernandez-Fernandez, M. Escudero-Escribano, P. Malacrida, I. E. L. Stephens and I. Chorkendorff, *Phys. Chem. Chem. Phys.*, 2014, **16**, 13718–25.

13 V. R. Stamenkovic, B. Fowler, B. S. Mun, G. Wang, P. N. Ross, C. A. Lucas and N. M. Marković, *Science*, 2007, **315**, 493–7.

14 X.-Z. Yuan, H. Li, S. Zhang, J. Martin and H. Wang, *J. Power Sources*, 2011, **196**, 9107–9116.

15 J. Monzó, D. F. van der Vliet, A. Yanson and P. Rodriguez, *Phys. Chem. Chem. Phys.*, 2016, **18**, 22407–22415.

16 T.-T. Nguyen, V. T. T. Ho, C.-J. Pan, J.-Y. Liu, H.-L. Chou, J. Rick, W.-N. Su and B.-J. Hwang, *Appl. Catal. B Environ.*, 2014, **154**–**155**, 183–189.

17 A. Lewera, L. Timperman, A. Roguska and N. Alonso-vante, *J. Phys.*

Chem. C, 2011, **115**, 20153–20159.

18 J. C. Meier, C. Galeano, I. Katsounaros, J. Witte, H. J. Bongard, A. A. Topalov, C. Baldizzone, S. Mezzavilla, F. Schüth and K. J. J. Mayrhofer, *Beilstein J. Nanotechnol.*, 2014, **5**, 44–67.

19 X. Tian, J. Luo, H. Nan, H. Zou, R. Chen, T. Shu, X. Li, Y. Li, H. Song, S. Liao and R. R. Adzic, *J. Am. Chem. Soc.*, 2016, jacs.5b11364.

20 J. L. R. Yates, G. H. Spikes and G. Jones, *Phys. Chem. Chem. Phys.*, 2015, **17**, 4250–4258.

21 Y. Liu, T. G. Kelly, J. G. Chen and W. E. Mustain, *ACS Catal.*, 2013, **3**, 1184–1194.

22 G. Cui, P. K. Shen, H. Meng, J. Zhao and G. Wu, *J. Power Sources*, 2011, **196**, 6125–6130.

PtCo/NbC and Pt/NbC catalyst for oxygen reduction reaction: synthesis, characterization, activity and durability

Javier Monzó[a] and Paramaconi Rodriguez[*,a]

[a.]School of Chemistry, University of Birmingham, Edgbaston, B15 2TT, Birmingham, England.

Corresponding author: p.b.rodriguez@bham.ac.uk

Table of contents

Section 1. Compositional characterization of PtCo nanoparticles.

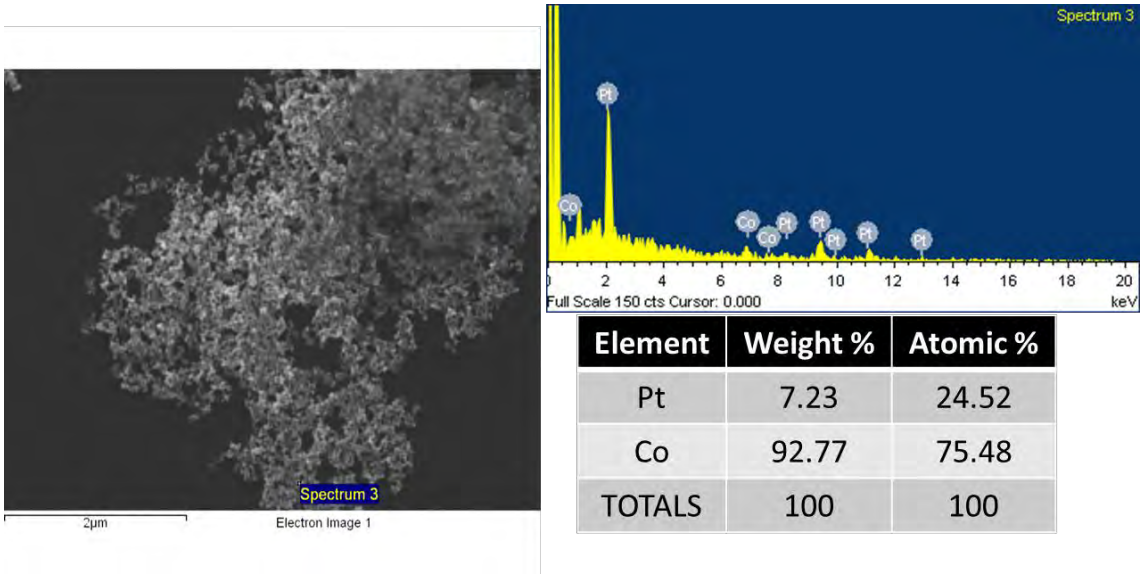

Element	Weight %	Atomic %
Pt	7.23	24.52
Co	92.77	75.48
TOTALS	100	100

Figure SI1. Compositional characterization of PtCo nanoparticles by Energy Dispersion X-ray (EDX). Scanning electron microscopy image of PtCo (left side), spectrum of elements and table summarising the composition (right side).

Section 2. X-ray diffraction patterns of Pt/NbC and PtCo/NbC.

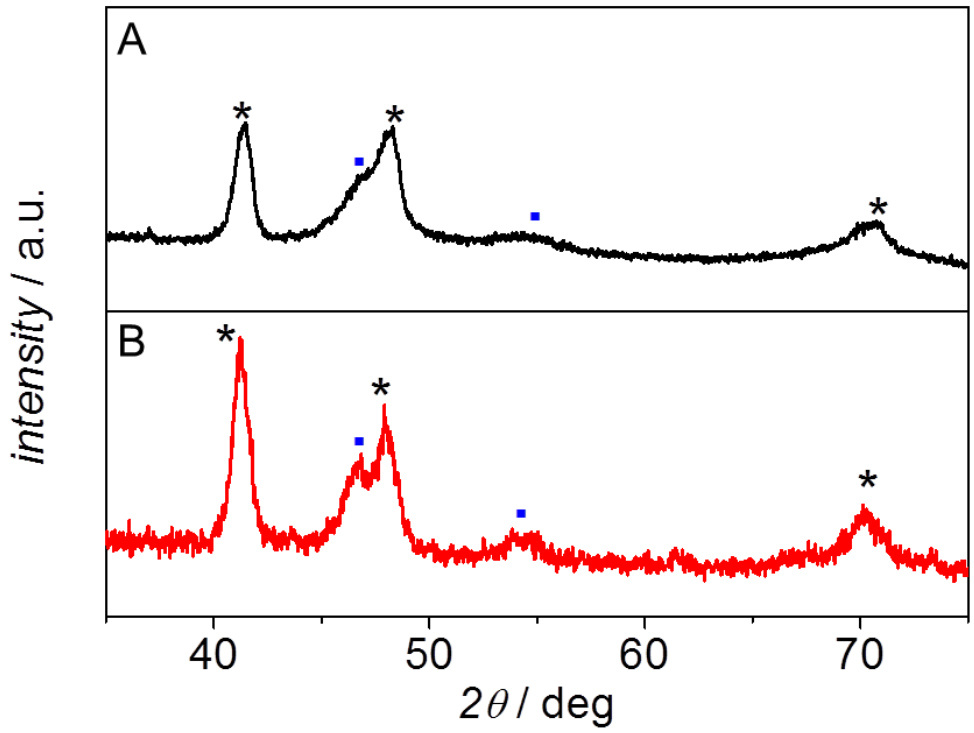

Figure SI2. XRD patterns of PtCo/NbC (A) and Pt/NbC (B). The black starts (*) indicate the reflections corresponding to NbC, whilst the signals Pt and PtCo are highlighted with the blue squares.

Section 3. X–ray fluorescence characterization of Pt/NbC and PtCo/NbC by XRF.

Figure S3 shows the X-ray fluorescence spectra of Pt/NbC and PtCo/NbC, the characterization was performed by triplicate in an aleatory order to prevent systematically errors. The emission line considered for the analysis was the more intense in order to prevent interferences from the background; Co (Kα), Pt (Lα) and Nb (Kα).

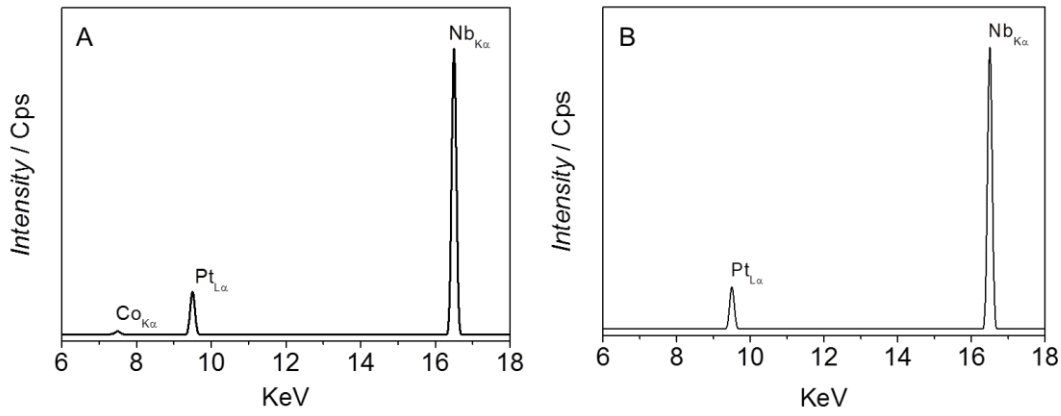

Figure SI3. X-ray fluorescence spectra of PtCo/NbC (A) and Pt/NbC (B).

The acquired results for the percentage composition are summarized in the table SI1.

Table SI1. Summary of the amount in weight of each element present in the catalysts.

Element	PtCo/NbC	Pt/NbC
Pt	20	19
Co	1	-
NbC	79	81

Section 4. Physical characterization of niobium carbide (NbC).

Figure SI4 shows the TEM images of NbC nanoparticles with a particle size around 10 nanometers. Figure S4-C shows the experimental XRD pattern (upper panel) and the data base pattern (PDF Card - 00-002-1031 NbC) (lower panel) with a proper fitting. The surface area for NbC was calculated from the nitrogen adsorption curve (Figure SI4-D) results applying the Brunauer–Emmett–Teller model, it is 76 m^2 g^{-1}.

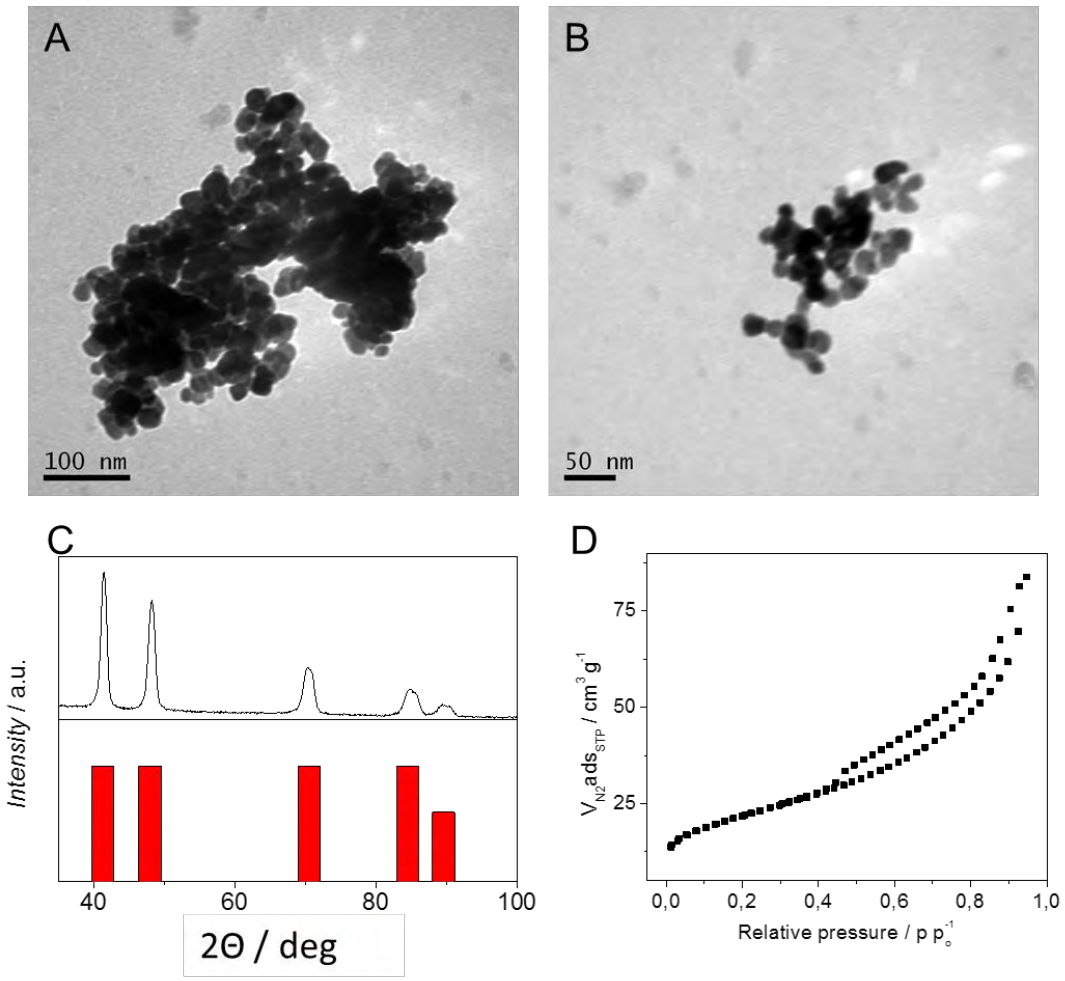

Figure SI4. (A-B) TEM images, (C) XRD pattern and (D) nitrogen adsorption curve of NbC.

Section 5. Physical characterization of Pt/C commercial catalyst.

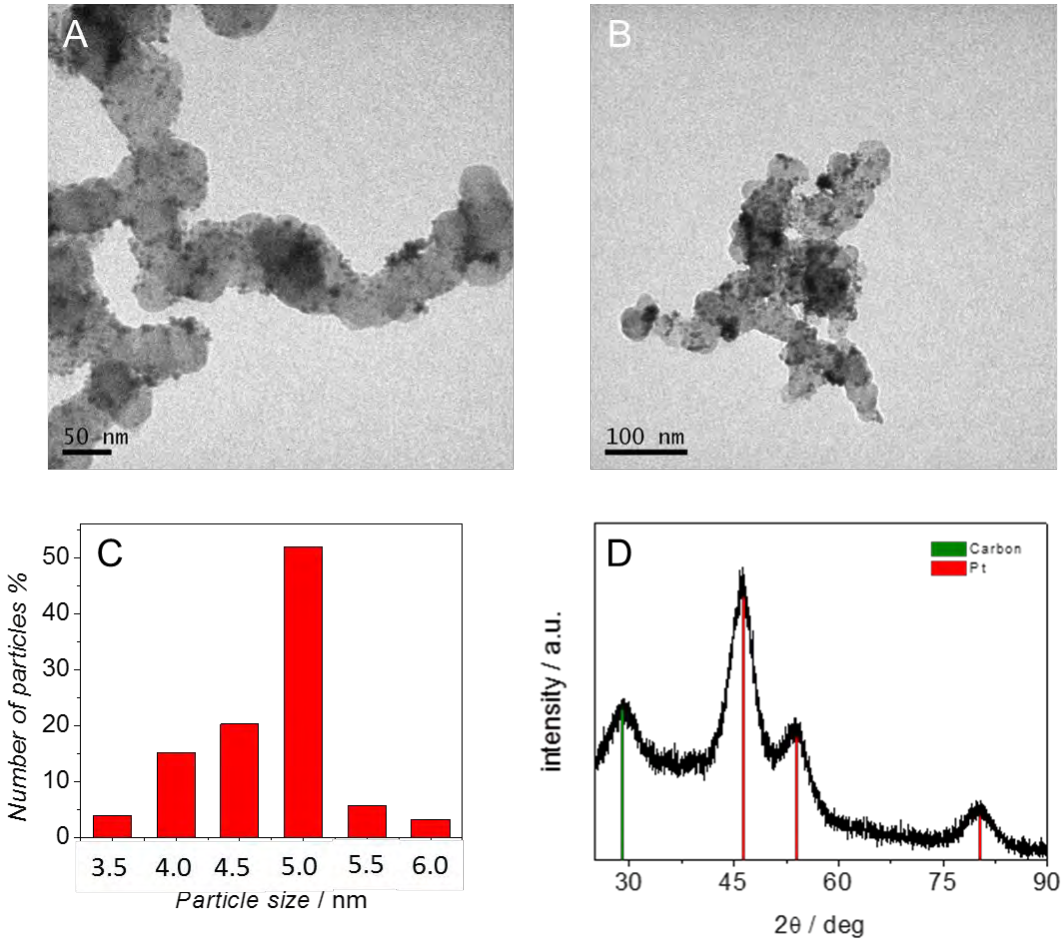

Figure SI5. (A-B) TEM images of Pt/C from ETEK Company. (C) Particle size distribution of Pt nanoparticles supported on carbon. The percentage of number of particles was calculated in base of the size of 200 nanoparticles. (D) XRD pattern in which signals of carbon (green line) and signals of platinum (red lines) are assigned.

Section 6. ORR Tafel plots of Pt/NbC, PtCo/NbC and Pt/C.

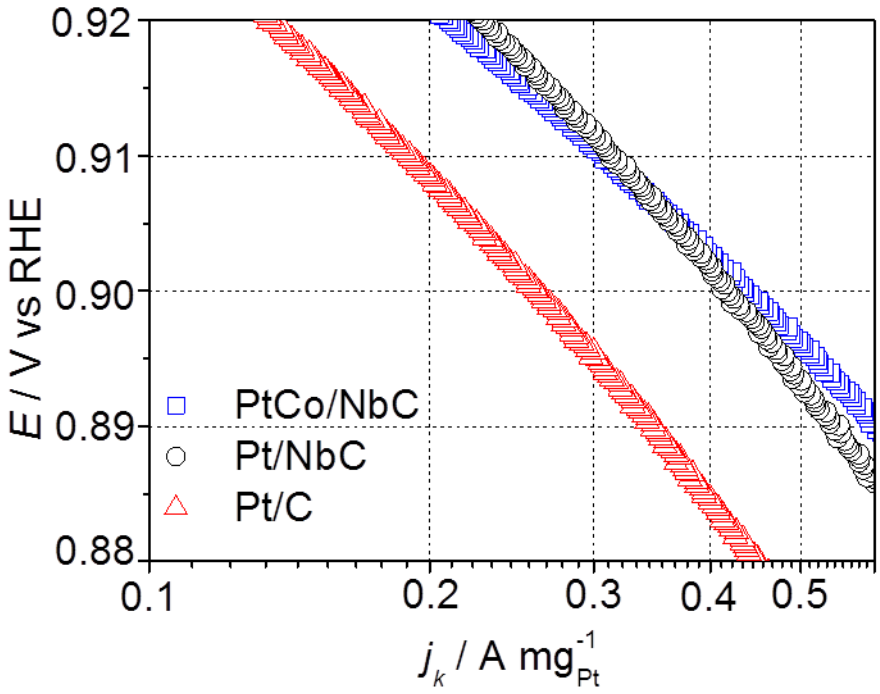

Figure SI6. Mass activity, j_k, of PtCo/NbC, Pt/NbC and Pt/C towards the ORR. The results shown are for the positive sweep scan at 20 mV s^{-1}.

Section 7. ORR polarization curve of PtCo/NbC and unsupported PtCo.

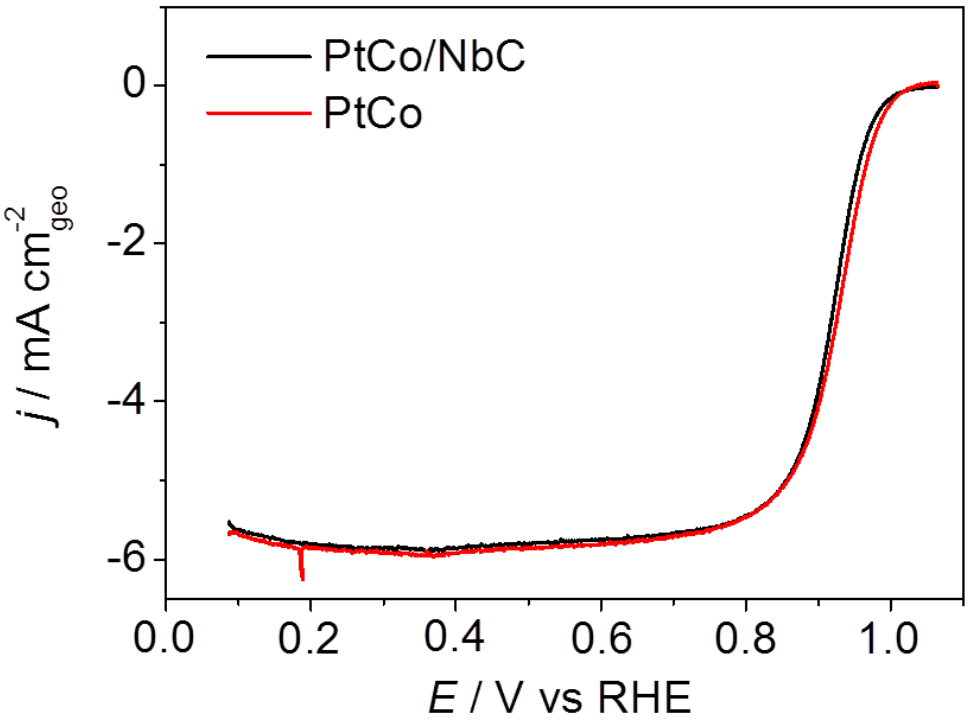

Figure SI7. ORR polarization curve of PtCo/NbC and unsupported PtCo nanoparticles. The results shown are for the positive sweep scan in 0.1 $HClO_4$ at 20 mV s^{-1}. Rotation rate: ω = 1600 rpm.

Section 8. X-ray fluorescence spectra of Pt/NbC and PtCo/NbC at different stages of the shut-up/shut-down protocol, showing Pt(L_α) and Co(Kα).

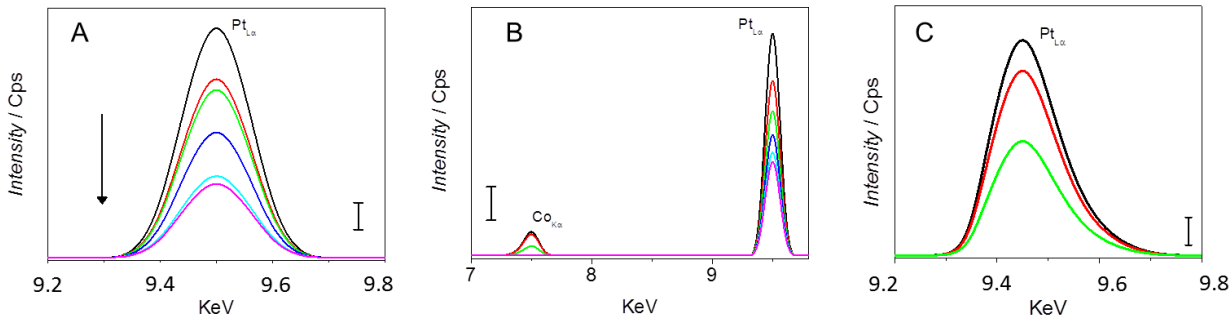

Figure SI8. XRF spectra of Pt/NbC (A), PtCo/NbC (B) and Pt/C (C) during the shut-up/shut-down protocol (scale bar = 100 Cps). The XRF spectra were acquired at 0 cycles (black), 500 cycles (red), 1000 cycles (green), 2000 cycles (blue), 3000 cycles (cyan) and 5000 cycles (purple). *GraphClick* software was used to digitalize the original data in order to present clear results.

Section 9. X-ray fluorescence spectra of Pt/NbC and PtCo/NbC in the region of Nb (Kα) at different control points of the shut-up/shut-down protocol.

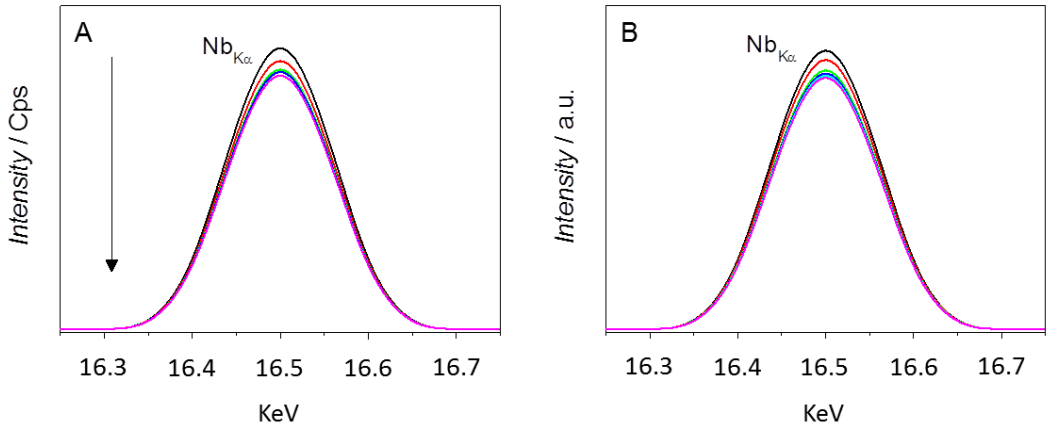

Figure SI9. (A) Spectra of Pt/NbC and (B) PtCo/NbC in the emission region of Nb (K_α) at diferent stages of the shut-up/shut-down protocol. The XRF spectra were acquire at 0 cycles (black), 500 cycles (red), 1000 cycles (green), 2000 cycles (blue), 3000 cycles (cyan) and 5000 cycles (purple). *GraphClick* software was used to digitalize the original data in order to present clear results.

Conclusions and future work

Given the current challenge of reducing the energy consumption and minimize the CO_2 emission, several technological solutions have been proposed. In the Chapter 1, I have introduced one of those, called Fuel Cell that is believed to provide an alternative solution to the use of internal combustion engines for automotive and stationary applications. Chapter 1 summarizes the particular aspects of the Polymer Electrolyte Fuel Cells which are the main subject of this thesis. This part also discusses the benefits and challenges associated with the technology. Some of those challenges have been chosen to be objectives of my work within this PhD project.

The overall goal of this thesis was to develop and evaluate new Pt-based catalyst for Polymer Electrolyte Fuel Cell applications. The main novelty relies on the utilization of transition metal carbides as support materials for the Pt-based catalyst. The transition metal carbides, as explained in the chapter 1, provide high conductivity and high chemical and electrochemical stability. On the other hand, some of the challenges, as described therein, are related to the synthesis of such transition metal carbides with high surface area and well-developed porosity. The second novel aspect of the thesis refers to the development of a methodology that allows the understating of the degradation mechanism of the catalyst under Fuel Cell operating conditions. A full comprehension of the degradation mechanism enables the development of improved catalyst based on a rational design. Chapter 1 describes the state-of-the-art of methods that have been used to draw a full picture of the degradation

mechanism. However, such methods have limitations that I have attempted to overcome with the methodology described in the Chapter 3.

A novel methodology for understanding the degradation mechanisms of the catalyst was developed via combining electrochemical measurements and X-ray fluorescence spectroscopy. This approach involves the use of electrochemical methods to determine changes in the ECSA and catalytic activity towards the ORR. Simultaneously, X-ray fluorescence has been used to track changes in chemical composition of studied materials. The combination of the results allowed us to describe the degradation mechanisms of the Pt-supported catalyst and to correlate such degradation mechanisms to the decrease of the mass catalytic activity towards the oxygen reduction reaction. The validation of the methodology was assessed using unsupported Pt nanoparticles (Pt-Nps), Pt nanoparticles supported on carbon (Pt/C) and Pt nanoparticles supported on TaC (Pt/TaC). It was found that Pt/TaC showed enhancement of mass activity and improvement of durability under mimic PEFC conditions (Chapter 3). This enhancement of catalytic activity could be associated with a Strong Metal Support Interaction (SMSI) between Pt and TaC. In addition, as a conclusion of this chapter, we have established a simple methodology that enables the understating of degradation of catalyst commonly used in fuel cells. I have reported that Pt, and Pt/C follows an associative degradation mechanism while the Pt/TaC follows a dissociative mechanism. Even more, I strongly believe that such a methodology could be further apply to study the degradation of other catalyst *e.g* metal catalyst commonly used for oxygen evolution reaction.[1–8]

Even though, this chapter allowed us to establish a well-defined protocol to understand the degradation mechanism of the catalyst and indicate that Pt supported catalyst on TaC has higher catalytic activity than the unsupported catalyst of the catalyst supported on carbon, the surface area of TaC was a limiting factor for the use of TaC as support material in a real fuel cell. For that reason, a series of transition metal carbides (TaC, NbC and VC) with high surface area have been synthesised via so-called urea route and thoroughly characterised. As shown in the Chapter 4, the transition metal carbides prepared with this method had surface area values of 51 $m^2 \cdot g^{-1}$, 76 $m^2 \cdot g^{-1}$ and 68 $m^2 \cdot g^{-1}$ for VC, NbC and TaC, respectively. Perhaps, one of the limitations to reduce the particle size, and increase the surface area even more, is the high temperature of the synthesis process. Pt nanoparticles have been dispersed on the prepared TMC and the ORR mass activity and the durability were assessed (Chapter 4). Pt nanoparticles supported in NbC showed a 1.7-fold enhancement of ORR mass activity as well more stability than Pt/C (commercial catalyst) under PEFC conditions. Pt/TMC presented similar trend in the decay of ECSA and Pt content as a function of degradation cycles. Dissociative mechanisms, *e.g.* Pt dissolution or particle detachment, were mainly responsible for Pt/VC and Pt/NbC degradation. In the first 2000 cycles, the degradation of Pt/TaC and Pt/C was controlled by associative mechanisms, *e.g.* Ostwald ripening or particle agglomeration. In the further cycles, the Pt/TaC degradation was controlled by dissociative mechanisms. Pt/TMC showed an improved stability under oxidative conditions as well as enhancement of the catalytic activity towards ORR. Pt/VC, Pt/NbC and Pt/TaC presented 1.9, 1.7 and 1.4-fold activity improvement with respect to Pt/C, respectively. I strongly believe that

the SMSI of Pt with TMC has an advantage effect on the stability and catalytic activity of Pt/TMC.

Finally, in chapter 5, PtCo nanoparticles were synthesized, characterized and dispersed onto NbC support. The selection of the PtCo and the NbC for this chapter was based on the fact that PtCo is currently one of the state-of-the-art catalysts for the ORR and the NbC was the support that showed the highest stability in the Chapter 4. In this chapter, I found that PtCo/NbC showed higher catalytic activity towards the ORR in comparison with the Pt-based catalyst in chapter 3 and 4 except Pt/VC. It was also found that the PtCo/NbC showed higher durability than previous catalyst in this thesis. The degradation of this catalyst followed a dissociative mechanism similar to Pt/NbC.

The work presented in this thesis has expanded the knowledge about Pt-based catalyst supported on transition metal carbides for PEFC application with regard to their design, synthesis, physical and electrochemical characterization, stability under PEFC conditions and ORR mass activity. The key learnings derived from this Thesis are summarised below:

1. **X-ray fluorescence (XRF) technique can be used to determine the degradation mechanisms of Pt-based catalysts.** XRF is an excellent tool to determine the amount of Pt, V, Ta, Nb and Co remained in the catalysts layer during the stability protocols. Combining mass of Pt and active area of Pt (ECSA) is possible to distinguish between associative and dissociative degradation mechanism (**Chapter 3**).

2. **Transition metal carbides are potential support materials for replacing carbon as support material for PEFC applications.** As shown in Chapters 3 and 4, Pt nanoparticles supported on TMC have shown enhanced ORR mass activity and improved of durability during the accelerated degradation protocols.

3. **Among the transition metal carbides studied in this thesis, NbC is postulated as the best support material to replace carbon. As it was shown in Chapters 4 and 5, the Pt-based catalyst has shown** an improvement in the catalytic activity and durability in comparison to the other transition metal carbides. It is proposed that such improvement could be associated to strong metal support interactions between the Pt-catalyst and the metal carbide support. However, our results are not fully conclusive in this aspect and further studies are required. For example, the use of in-situ X-ray absorption spectroscopy and UPS/XPS analysis could provide evidence of such interactions and changes in the electronic structure of the catalyst.

This Thesis has expanded the knowledge of Pt-based catalyst support on transition metal carbides, and opens new avenues for the design of durable catalyst for PEFC applications. The optimization of the novel technique presented in **Chapter 3** has a great potential to allow distinguish between Pt dissolution and particle detachment (dissociative mechanisms) or between particle agglomeration and Ostwald ripening (associative mechanism. A combination of our technique with *in situ* TEM could allow us to distinguish *e.g.* between Pt dissolution or particle detachment. As such, future efforts should focus on the study and improvement of the dispersion of Pt and PtCo

nanoparticles on the transition metal carbides to avoid agglomeration or detachment of the particles (**Chapter 3**). We have suggested in this Thesis that the enhancement of the ORR mass activity is associated with an electron transfer between the support material and the metal nanoparticles (**Chapter 4** and **Chapter 5**), but the characterization of this electron donation could be proved by X-ray photoelectron spectroscopy.

The next steps to carry out on behalf of the results obtained in this thesis are described as follow:

- **Combine the XRF technique and the electrochemical measurements with a microscopical technique *e.g.* TEM.** More complete information on the mechanisms of catalysts degradation would assist in the design and preparation of catalysts.

- **Study the electronic structure of the catalysts using in-situ X-ray absorption spectroscopy and UPS/XPS analysis** to understand and corroborate the interactions between Pt and TMC and changes in the electronic structure that provide evidence of the origin of improved stability and enhanced catalytic activity towards ORR.

- **Scale-up the synthesis of NbC and the dispersion of Pt nanoparticles.** The results shown in this thesis were obtained at laboratory scale. A synthesis of NbC on a larger scale may present problems. Equally, the dispersion of platinum nanoparticles on NbC has to be studied and evaluated. Improved dispersion can enhance the

stability of nanoparticles deposited on NbC as well as the attachment of Pt nanoparticles on NbC.

- **Study the durability and the mass activity of Pt/NbC in a real polymer electrolyte fuel cell.** It has been proved in the literature that the stability of the catalyst in real fuel cells differs from the lab conditions.

References

1 P. Justin, P. H. K. Charan and G. R. Rao, *Appl. Catal. B Environ.*, 2014, **144**, 767–774.

2 T. P. Johansson, E. T. Ulrikkeholm, P. Hernandez-Fernandez, M. Escudero-Escribano, P. Malacrida, I. E. L. Stephens and I. Chorkendorff, *Phys. Chem. Chem. Phys.*, 2014, **16**, 13718–25.

3 K. Jukk, N. Kongi, K. Tammeveski, J. Solla-Gullón and J. M. Feliu, *Electrochem. commun.*, 2015, **56**, 11–15.

4 Q. Huang, H. Yang, Y. Tang, T. Lu and D. L. Akins, *Electrochem. commun.*, 2006, **8**, 1220–1224.

5 P. Hernandez-Fernandez, F. Masini, D. N. McCarthy, C. E. Strebel, D. Friebel, D. Deiana, P. Malacrida, A. Nierhoff, A. Bodin, A. M. Wise, J. H. Nielsen, T. W. Hansen, A. Nilsson, I. E. L. Stephens and I. Chorkendorff, *Nat. Chem.*, 2014, **6**, 732–738.

6 I. J. Hsu, D. a. Hansgen, B. E. McCandless, B. G. Willis and J. G. Chen, *J. Phys. Chem. C*, 2011, **115**, 3709–3715.

7 V. T. T. Ho, C. Pan, J. Rick, W. Su and B. Hwang, *J. Am. Chem. Soc.*, 2011, **133**, 11716–11724.

8 P. Malacrida, H. G. Sanchez Casalongue, F. Masini, S. Kaya, P. Hernández-Fernández, D. Deiana, H. Ogasawara, I. E. L. Stephens, A. Nilsson and I. Chorkendorff, *Phys. Chem. Chem. Phys.*, 2015, **17**, 28121–28128.

Appendix I

Cyclic voltammetry: Electrochemical Surface Area (ECSA) and ORR Catalytic Activity measurements

1. Fundamentals of the technique and determination of the ECSA

Cyclic voltammetry is a commonly used method for measuring electrochemical reactions. When using this method, a ramp of potentials is applied as a function of time between two potential limits and the current is measured. The electrochemical response is associated to changes in the double layer (electrostatic interactions) or to Faradaic process (electron-transfer reactions) taking place on the working electrode.[1]

Occasionally, these processes, capacitive currents or Faradaic currents, are of great use to determine the electrochemical surface area of materials. The capacitive current, for example, is commonly used to determine the electrochemical surface area of metal oxides commonly use in capacitors or as oxygen evolution catalyst.[2–5] On the other hand, faradaic processes can be used to measure the ECSA in case of catalytically-active metals. The best example is Pt, where electron-coupled proton adsorption and desorption indicate the surface area of electrochemically active Pt surface.[6,7]

The electrochemical surface area (ECSA) of platinum catalysts is essential for this project. By knowing the ECSA, I was able to report the specific activity of the different catalyst and to determine if, the catalyst is changing — e.g. dissolving – during the degradation protocols. [8–10]

The adsorption/desorption of H^+ on Pt involves one electron transfer, it is possible to calculate the ECSA using the charge (Q_H) associated with the adsorption/desorption of a monolayer layer of hydrogen in the H_{upd} region. Figure 1 shows highlighted in red the charge area associated with the desorption charge of a layer of H^+ from Pt surface.

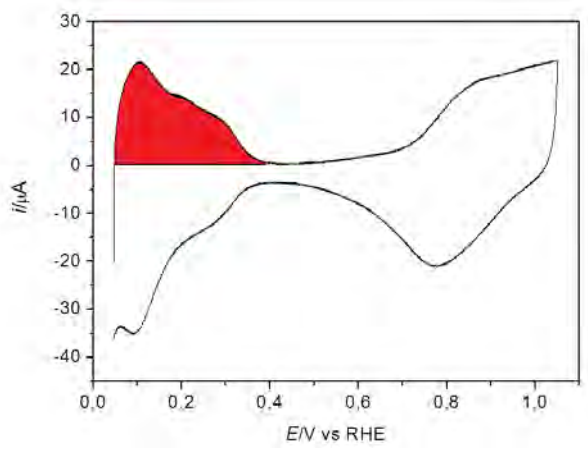

Figure 1 Voltammetric profile of platinum nanoparticles in 0.1 M $HClO_4$ at 20 mV s^{-1}. Area corresponding to a desorption layer of H^+ is highlighted in red.

The theoretical value for the charge density of the hydrogen adsortion for a polycrystalline Pt surface is 210 μC/cm^2.[8,11] Thus, using the equation I and determining the charge associated to the adsortion/desorption process of hydrogen in each of the Pt catalyst I was able to determine the ECSA of the catalyst. [6]

$$\mathbf{ECSA} = \frac{\mathbf{Q_H}}{\mathbf{210\ \nu}}\ (cm^2) \qquad (I)$$

2. ORR Catalytic Activity measurements

In order to study ORR's kinetics and durability of the novel catalysts, a rotating disk electrode (RDE) configuration was employed. RDE is a well-known method to obtain efficient mass transport, which is important to keep constant the concentration of oxygen around the electrode (figure 2A).[12,13]

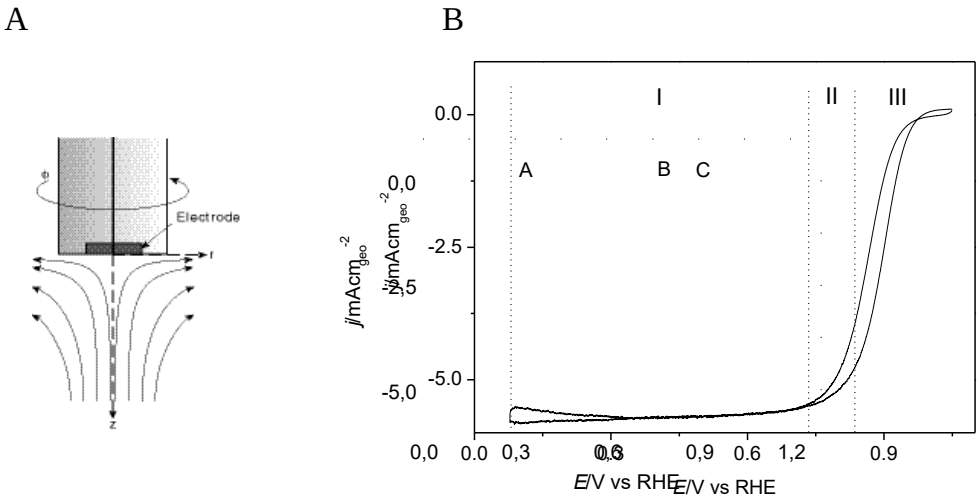

Figure 2 (A) Scheme of the O_2 diffusion profile to the surface of the rotating electrode. (B) ORR polarization curve of Pt nanoparticles supported on a glassy carbon disk in 0.1 M $HClO_4$ at 20 mV s^{-1}. Rotation rate: 1600 rpm.

The typical voltammetric profile for ORR presents three well defined regions that can be identified in the figure 2B. The region I, between 0.05 V - 0.75 V vs RHE is associated with the ORR controlled by the diffusion of oxygen towards the electrode. The region II between 0.75 V - 0.85 V is controlled by both diffusion and kinetics of the process. The current region III between 0.85 V - 1.00 V is controlled by the kinetics of the process.

The measured oxygen reduction current has contribution of both current controlled by the diffusion and current controlled by the kinetics as Koutecky-

Levich equation described (eq.II). The diffusion current is defined by the Levich equation (eq.III) which establishes that this current is proportional to the number of electron transferred (n), Faraday constant (F, 96,485 C · mol^{-1}), electrode geometrical area (A, cm^2), rotating rate (ω), diffusion coefficient (D, $1.8 \cdot 10^{-5}$ $cm^2 \cdot s^{-1}$) and kinematic viscosity (ϑ, 0.01 $cm^2 \cdot s^{-1}$).[14] Essentially, diffusion current depends on the electrode area, the electrolyte, the angular rate and the number of electrons involved in the reaction.

$$\frac{1}{i} = \frac{1}{i_k} + \frac{1}{i_d} = \frac{1}{i_k} + \frac{1}{0.62\ n\ F\ A\vartheta^{-1/6}\omega^{\frac{1}{2}}\ C\ D^{\frac{2}{3}}} \qquad \text{(II)}$$

$$i_d = 0.62\ n\ F\ A\vartheta^{-1/6}\omega^{\frac{1}{2}}\ C\ D^{\frac{2}{3}} \qquad \text{(III)}$$

In order to obtain the intrinsic activity of the catalysts, the kinetic current (i_k) can be derived from the measured current without the diffusion contribution using the equation IV.

$$i_k = \frac{i_d - i}{i \cdot i_d} \qquad \text{(IV)}$$

In this Thesis, the electrochemical measurements were carried out in a two compartments electrochemical cell using an Au wire as counter electrode, gold is stable at high potential were ORR takes place, and a calomel reference electrode. All the results are presented in a Reversible Hydrogen Electrode (RHE) scale. Electrochemical measurements were performed with an Autolab PGSTAT12. Solutions were prepared from $HClO_4$ (Suprapure, Merck), and ultra-pure water (ElgaPureUltra, 18.2 MΩ cm, 1 ppb total organic carbon).

Argon (Ar, N66) was used to deoxygenate all solutions and oxygen (O_2, N5.0) was employed to saturate with oxygen the solutions to perform the ORR.

References

1 K. Kinoshita, *Carbon : Electrochemical and Physiscochemical Properties*, Wiley, New York, 1988.

2 L. Manjakkal, W. T. Navaraj, C. G. Núñez and R. Dahiya, *Adv. Sci.*, 2019, **6**, 1802251.

3 C. C. L. McCrory, S. Jung, I. M. Ferrer, S. M. Chatman, J. C. Peters and T. F. Jaramillo, *J. Am. Chem. Soc.*, 2015, **137**, 4347–4357.

4 C. C. L. McCrory, S. Jung, J. C. Peters and T. F. Jaramillo, *J. Am. Chem. Soc.*, 2013, **135**, 16977–16987.

5 S. Jung, C. C. L. Mccrory, I. M. Ferrer, C. Peters and T. F. Jaramillo, 2016, 3068–3076.

6 J. C. J. Solla-Gullón, V. Montiel, A.Aldaz, *J. Electroanal. Chem.*, 2000, **491**, 69–77.

7 K. J. J. Mayrhofer, D. Strmcnik, B. B. Blizanac, V. Stamenkovic, M. Arenz and N. M. Markovic, *Electrochim. Acta*, 2008, **53**, 3181–3188.

8 R. Latsuzbaia, E. Negro and G. Koper, *Fuel Cells*, 2015, **15**, 628–638.

9 R. L. Borup, J. R. Davey, F. H. Garzon, D. L. Wood and M. A. Inbody, *J. Power Sources*, 2006, **163**, 76–81.

10 S. Cherevko, G. P. Keeley, S. Geiger, A. R. Zeradjanin, N. Hodnik, N. Kulyk and K. J. J. Mayrhofer, *ChemElectroChem*, 2015, **2**, 1471–1478.

11 F. Hasché, M. Oezaslan and P. Strasser, *ChemCatChem*, 2011, n/a-n/a.

12 K. J. J. Mayrhofer, D. Strmcnik, B. B. Blizanac, V. Stamenkovic, M. Arenz and N. M. Markovic, *Electrochim. Acta*, 2008, **53**, 3181–3188.

13 N. M. Markovic, T. J. Schmidt, V. Stamenkovic and P. N. Ross, *Fuel Cells*, 2001, **1**, 105–116.

14 N. Alexeyeva, A. Sarapuu, K. Tammeveski, F. J. Vidal-Iglesias, J. Solla-

Gullón and J. M. Feliu, *Electrochim. Acta*, 2011, **56**, 6702–6708.

Appendix II

X-ray fluorescence: fundamentals and measurements

1. Fundamentals of the technique

X-ray fluorescence is a spectroscopic technique used to elemental analysis and chemical composition.[1-3] Fluorescence phenomenon is the process of re-emission of radiation from the sample under study as a consequence of a previous exposure to radiation.

The fluorescence process is the ionization of the atoms when they are irradiated with the proper amount of energy.[2] This ionization ejects core electrons leading gaps in internal orbitals, these gaps are occupied by electrons in the external shells. The electron transitions between orbitals are L → K, M → K and M → L called K_α, K_β and L_α respectively (Figure 1).

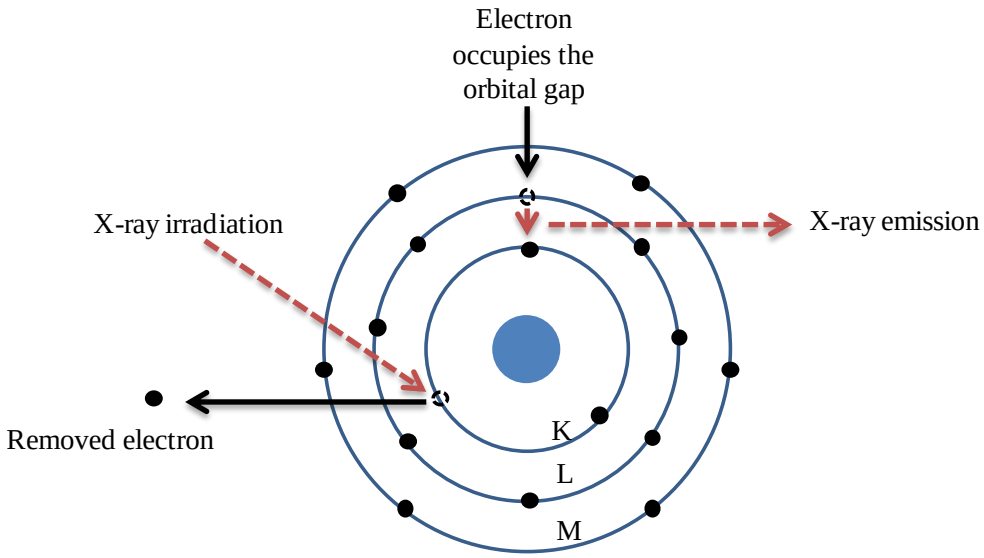

Figure 1 Schematic representation of fluorescence phenomenon.

As a consequence of this electronic re-ordering, energy is released as photons whose energy is proportional to the energy difference of the orbitals involved. Planck's equation (eq. I) defines that the irradiated wavelength is proportional to the speed of light, Planck's constant and inversely proportional to the orbital energy.

$$\lambda = \frac{h\,c}{E} \qquad \text{(I)}$$

The elemental composition of a sample can be determined because the difference in energy between the orbitals of each element is different.

2. Description of the experimental protocol and analysis of XRF results

XRF is a powerful tool to analyse traces of heavy metals in samples or composition of Pt-alloy nanoparticles. In this Thesis, XRF has been used to determine the amount of Pt remaining in the carbon disk of the RDE configuration after degradation cycles.

For the construction of the calibration curve of Pt, samples with different concentrations of Pt nanoparticles were prepared by depositing given volume of a well-known solution of Pt nanoparticles (125 $\mu g \cdot mL^{-1}$) on a zero response carbon disk. Figure 2 shows an XRF spectrum obtained for the Pt samples. The *intensity* of the signal $Pt_{L}\alpha$ (9.45 KeV) was measured using the GraphClick software. This software was employed to digitalised spectra to present clear results and determine the maximum value of $Pt_{L}\alpha$ signal. Then, the *intensity* of $Pt_{L}\alpha$ signal was plotted as a function of the well-defined Pt content controlled during the preparation of the samples. As a result, it was obtained a linear response between the $Pt_{L}\alpha$ intensity and the mass of Pt within the catalyst layer with a correlation coefficient of 0.996.

Such linear correlation was used as a calibration curve of the XRF and was employed during the degradation protocols to determine the amount of Pt remaining in the carbon disk of the rotating disk electrode. Similar procedure was used to prepare calibration curves for TaC as shown in figure SI3 of Chapter 3.

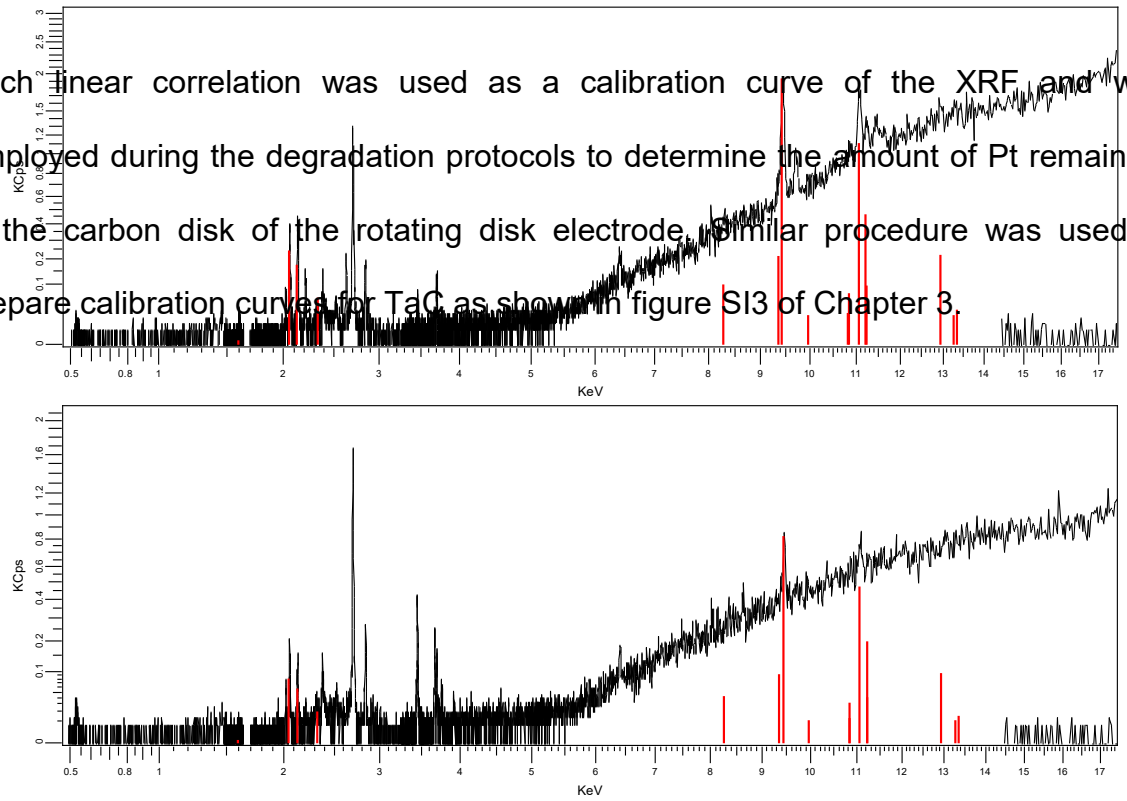

Figure 2 X-ray fluorescence spectrum of Pt/C catalyst. The red lines indicate the signals associated to the transition energy of platinum.

Prior each degradation protocol, the XRF spectra of the catalyst film prepared as described in section 2.3 of Chapter 3 was measured. The intensity of the signals of the metals under study (*e.g.* Pt and Ta) was used as reference during the evaluation of catalyst degradation. The amount of remaining Pt and Ta upon degradation cycles were calculated using the calibration curves on figures SI2 and SI3 of Chapter 3. For the rest of metals studied in Chapter 4 and 5 (*e.g.* V, Nb and Co), the remaining loading upon degradation cycles was estimated by comparing of the initial intensity of the signals and the intensity after the degradation cycles.

The values of each metal content, *e.g.* Pt, as a function of time or number of cycles, are relative values referred to the initial value of the baseline (t=0 s) for each film prepared and evaluated.

References

1 L. A. Hutton, G. D. O. Neil, T. L. Read, Z. J. Ayres, M. E. Newton, J. V Macpherson, D. Chemistry, S. Ultra and C. Calibration, Anal. Chem., 2014, Supporting, 1–8.

2 M. West, A. T. Ellis, P. J. Potts, C. Streli, C. Vanhoof, D. Wegrzynek and P. Wobrauschek, J. Anal. At. Spectrom., 2012, 27, 1603.

3 E. Bennett, J. Monzó, J. Humphrey, D. Plana, M. Walker, C. McConville, D. Fermin, A. Yanson and P. Rodriguez, ACS Catal., 2016, 6, 1533–1539.